UNIVERSITY OF LIVERPOOL

Nuclear Structure Studies of ^{159}Er up to High Spin.

Thesis submitted in accordance with the requirements of the University of Liverpool for the degree of Doctor in Philosophy

by

Mohammed Ibrahim Mohammed Mustafa

200573203

Oliver Lodge Laboratory

2012

"Success is not measured by the position you reach in life. It's measured by the obstacles you overcome."

Booker T. Washinghton.

This thesis is dedicated to:

- The pure soul of my deceased father, God forgive him who, after God, was the source of guidance and support to me throughout my life.
- The soure of inspiration my mother, for all her sufferings and endurance that she faced throughout her life to educate me in the best way.
- My sisters and brothers who have given me the opportunity to maintain my professional development and have undertaken all my study costs in different stages of my life.
- My beloved wife (Kazhal) and my little son (Wlat) for their unconditional love and inspiration throughout my PhD.

Acknowledgements

I would like to take this opportunity to express my deepest appreciation and thanks to thsoe people who guided me and shared their experiences during my four years study and research. Without their guidance and persistent assistance, this thesis would not have been possible.

- I would like to thank, foremost my supervisor Prof. Paul Nolan, for allowing me the opportunity to study at thr University of Liverpool, who was the source of ongoing guidance and support during my time as a PhD student.
- I would like also to thank the well-known and highly respected experts in the nuclear structure of Erbium nuclei, Prof. John Simpson with Dr. Eddie Paul and Dr. James Ollier for their insights on my research analysis through responses to all the questions that I have during my research.
- A special thanks to my secondary supervisour Dr Andy Boston, with Prof. Rodi Herzberg, Prof. Robert Page and Dr. Dave Joss for giving me the opportunity to take a part in all MSc. and postgraduate modules during my first year.
- In addition, I would like to thank all PhD students of the Liverpool Nuclear Structure Group, both past and present, especially John Revill, Robert Carroll, Laim Gaffney and Joseph Ress for their assistance to training practice techniques that have been used in this research and for proof reading this thesis.
- I express my gratitude to that relative justice which is verified in higher education in Iraq after freedom day (09/04/2003), that gave an opportunity for me and thousands of iraqi students to complete postgraduate study.
- Finally, I much indebted to Mr. Mstafa Said Qadr, Dr. Barham Ahmed Salh, Dr. Bayazid Hassan, Mr Haji H. Ibrahim and Mr. Harf Tayfur who provided support and a secure life for me in Baghdad after my nomination for PhD scholarship.

Abstract

In the current work a detailed spectroscopic investigations of the gamma-decays from the excited states of the rare-earth nucleus ^{159}Er has been performed to study the structural properties up to possible ultrahigh spins. The nucleus of ^{159}Er had been populated by the reaction ^{116}Cd(^{48}Ca,5$n\gamma$) at beam energy of 215-MeV in an experiment at Argonne National Laboratory using the Gammashphere array. Following a hypercube analysis of the collected data, new rotational bands were observed and the previously reported bands were extended up to possible spin through observation of new gamma-ray transitions in coincidence with the existing sequences. Possible angular intensity-ratio, B(M1)/B(E2)-ratios, measurements have been performed to confirm the nature of previously observed transitions and to assign multipolarites of the new ones. The band structures are discussed within the framework of cranked shell model calculations, revealing a diverse range of quasiparticle configurations. At spins of around 50$\hbar$, there is evidence for a change from dominant prolate collective motion in the yrast band and its signature partner to oblate non-collective structures via the mechanism of band termination. A possible strongly deformed triaxial band occurs at these high spins, which indicate collectivity beyond 50$\hbar$. The high-spin structures of data are interpreted within the framework of cranked Nilsson-Strutinsky calculations.

Contents

List of Figures

List of Tables

Chapter 1

Introduction

1.1 Introduction

The developments in gamma-ray spectrometers have allowed achievements in the understanding of the structure of nuclei upto ultrahigh spins. The work in the present thesis focuses on the analysis of gamma decays detected by the Gammasphere array from the ($5n\gamma$) reaction channel of the fusion evaporation reaction in an experiment between a beam of ^{48}Ca at energy 215 MeV provided by the ATLAS facility and a target of two self-supporting ^{116}Cd foils with a total thickness 1.3mg/cm^3 at Argonne National Laboratory. The present reaction channel corresponds to the population of the ^{159}Er nucleus. The spectroscopic investigation revealed new gamma-ray transitions which are fitted into four new bands (three bands in the current work and a band with high moment of inertia which has been reported in [Oll09]) and into the previously known bands [Del87, Sim98]. The experimental results have been interpreted in terms of the Cranked Shell Model and at high spin the structure of the bands compared with the predictions of Cranked Nilsson-Strutinsky calculations. This thesis comprises of another five chapters; Chapter 2 introduces the concepts and nuclear models that are used to describe the nuclear system. The nuclear shell model, spherical shell model and nuclear potentials, nuclear deformation, Nilsson model, Strutinsky shell correction procedure and Pairing and quasiparitcles are explained. In chapter 3,

the nuclear rotation, mechanisms of the generation angular momentum and cranking models have been introduced. Chapter 4 is devoted to common experimental details; the mechanism of fusion evaporation reactions and gamma-ray interactions with matter, gamma-ray detectors and the Gammasphere array as well as the experimental techniques that have been used to analyse the gamma decays from the excited states of the populated nucleus ^{159}Er. The details of the experimental results extracted from the gamma-ray spectroscopic analysis of ^{159}Er are discussed in chapter 5, and finally in chapter 6 the experimental results have been interpreted as mentioned in terms of the cranked shell model and Nilsson-Strutinsky calculations. This work has been published by M. Mustafa *et al.,* in PRC 85, 054320 (2011), [Mus11].

Chapter 2

Nuclear Models

2.1 Introduction

The concepts of the compound nucleus and of bulk properties of nuclei, such as the distribution of nuclear matter within nucleus, can be considered as the principles of the first thought to describe the nuclear interactions between the constituents of the nucleus to be of short-range as in an incompressible drop of charged liquid. This assumption led Weizsäcker to devise a formula in 1935 for the nuclear binding energy and mass of the nucleus using a semi-classical method [Wei35]. This description of the nucleus was considered to be the first nuclear structure model, which is known as the Liquid Drop Model (LDM). In this model the binding energy and mass of the nucleus vary smoothly with the atomic mass (A) of nucleus. The (LDM) model was very successful in explaning the systematic behaviour of the average binding energy per nucleon, and gives reasonable interpretations for some phenomena related to the fission of heavy nuclei. In spite of the above mentioned successes, the experimental observations revealed some results that were not consistent with the predictions of the model. In particular, the appearance of extra binding in some nuclei at specific proton and neutron numbers (2, 8, 20, 28, 50, 82 and 126), that are now called magic numbers. This suggests a limitation of the linear relationship of nuclear properties with atomic number (Z) at magic numbers that correspond to the closed shells in

nuclei. Furthermore, the model could not treat the natural behaviour of deviation from a spherical shape in the ground state of some nuclei. Because of these discrepancies, and observations of remarkable experimental evidence for shell structure and single particle behaviour in the nuclei, like in atomic physics, that could not interpreted by the (LDM), an enhancement of the model, to introduce the single particle behaviour of nuclei, which will be presented in this chapter in the form of the shell model which describes the microscopic properties of nuclei under the influence of quantum mechanics.

2.2 The Nuclear Shell Model

The successes of the shell model in atomic physics led to the attempts to interpret discrepancies in nuclear binding energies at closed shells. Therefore, nuclear physicists tried to use similar concepts of shells in the nucleus. Thus, the structure of the nucleus is characterised by energy and quantum numbers of the nuclear shells, in the Nuclear Shell Model. The model assumes that individual nucleons (proton or neutron) move independently from each other in a potential created by the average interaction of all the other nucleons in the nucleus. The individual nucleons are distributed into the nuclear shells, and occupy the energy levels of the shells according to increasing energy and the specified quantum numbers of the shell. The distribution of nucleons obeys the Pauli Exclusion Principle which states that "no two identical fermions can occupy the same quantum state". The existence of shell structure in the nucleus is supported by several experimental pieces of evidence outlined in the following:

- Deviation of the measured nuclear masses at certain nucleon numbers, (the proton and neutron magic numbers at closed shells) from of the liquid drop model.
- Proton magic nuclei are of high relative natural abundance.
- Nuclei with proton or neutron magic numbers exhibits sharp increase (disconti-

nuity) in nucleon separation energies compared with the prediction of the liquid drop model. This indicates that to excite nucleons from the closed shell to a higher shells requires a large energy, and the separation energy will be largest for doubly magic nuclei.

- The high lying excitation energy of the first excited state 2^+ in proton or neutron (either or both) magic numbers even-even nuclei.

- Variation of the measured reduced electromagnetic probability B(E2:$2^+ \rightarrow 0^+$) for even-even nuclei. It is of the lowest value at closed shells and will be highest at mid-shells. Through this measurement, one can calculate the electric quadrupole moments and deformation parameters, which indicate deviation from a spherical shape in nuclei.

The motion of individual independent nucleons in the nucleus was addressed by using a non relativistic Schrodinger equation with a central potential, and the energy of nuclear system described by Hamiltonian.

$$H = \sum_i T_i + \sum_i V(r_i) \tag{2.1}$$

The first term in equation of energy $\sum_i T_i$ represents the sum of the kinetic energies of individual nucleons and the second tem $\sum_i V(r_i)$ is the form of the average potential energy between interacting nucleons.

2.3 Spherical Shell Model and Nuclear Potential

Many attempts have been made at modelling the nuclear shell model with different nuclear potentials to explain the observed energy levels and predict the correct magic numbers that correspond to shell closures. The success of the shell model depends on the choice of nuclear potential. The characteristics of the interaction potential between the nucleons identifies the form (shape) of the nucleus and naturally produce the gap between the energy levels of the nuclear shells at magic numbers. The use

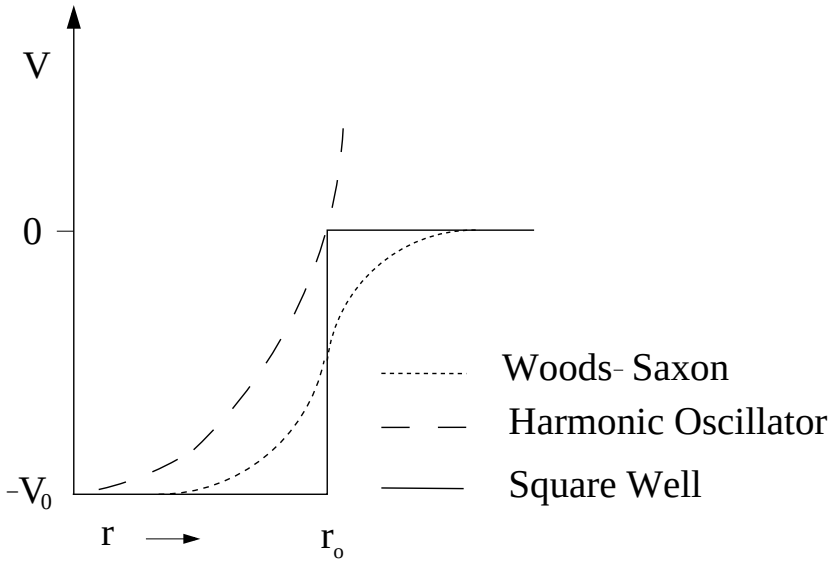

Figure 2.1: An illustration of three potential wells used to model the nuclear potential. V_0 is the well depth, r the distance from the origin, and r_o the nuclear radius.

of a central potential, which is spherically symmetric, gives a spherical shape to the nucleus, and introduces the nuclear system in spherical shell model. The most commonly used potentials in the spherical shell model are the square well, harmonic oscillator and Woods-Saxon potentials, illustrated in Figure 2.1. The Hamiltonian in spherical coordinates has been solved with these potentials, to identify energy levels and group them in the experimentally observed shell closures. The simplest description for a nuclear potential is the square-well potential. This potential has infinite limit with sharp edges and does not produce the experimentally observed magic numbers, so it will not be outlined in the following sections.

2.3.1 Harmonic Oscillator Potential

The harmonic oscillator potential provides a successful description for the nuclear shell model. However it is an unphysical potential as the nuclear force has no presence outside the nucleus. The harmonic oscillator potential is given by [Rin80]:

$$V_{HO}(r) = -V_o \left[1 - \left(\frac{r}{R_0}\right)^2\right] = \frac{1}{2} m\omega_0^2 (r^2 - R_0^2) \tag{2.2}$$

where R_0 is the nuclear radius, V(r)= 0 for $r > R_0$. $V_0 = \frac{m}{2}\omega_0^2$ is the depth of the potential well, m is the mass of a nucleon and ω_0 is the oscillator frequency of the particle in simple harmonic motion. The eigenvalues of the Hamiltonian for the harmonic oscillator potential are given by:

$$E_N = \left(N + \frac{3}{2}\right)\hbar\omega_0 + V_0 \tag{2.3}$$

and

$$N = 2(n-1) + l \tag{2.4}$$

where N is the oscillator quantum number, n is the radial quantum number, and l is the orbital angular momentum quantum number. The value of N in each oscillator shell degenerates to a set of levels, with either even or odd values of the allowed orbital angular momentum (l=N, N-2,.....,1 or 0). The equally-spaced levels (major shells) could be occupied by maximum number (N+1)(N+2)of identical nucleons. The parity of each level is given by:

$$\pi = (-1)^l = (-1)^N \tag{2.5}$$

The labelling of the levels and the occupation limit of the shells of harmonic oscillator potential are illustrated in table 2.1.

N	Allowed l	Level Label (n,l)	$E_N(\hbar\omega_0)$	Occupation $\sum 2(2l+1)$	Total
0	0	$1s$	3/2	2	2
1	1	$1p$	5/2	6	8
2	2, 0	$1d$, $2s$	7/2	12	20
3	3, 1	$1f$, $2p$	9/2	20	40
4	4, 2, 0	$1g$, $2d$, $3s$	11/2	30	70
5	5, 3, 1	$1h$, $2f$, $3p$	13/2	42	112
6	6, 4, 2, 0	$1i$, $2g$, $3d$, $4s$	15/2	56	168

Table 2.1: Occupation of harmonic oscillator shells.

The Harmonic oscillator potential with this description only produces the first three magic numbers (2, 8 and 20). Nevertheless, the model has been modified to

a more realistic form with contributions of an attractive term l^2 and a spin-orbit interaction. The l^2 term refines the shape of the potential to an intermediate shape between the square well and harmonic oscillator potentials and lowers the energy levels of the higher orbital angular momentum states, as illustrated in the middle part of Figure 2.1. The latter term will be disused in the next section.

2.3.2 Spin Orbit Interaction

The effect of the total angular momentum of each single nucleon in the nucleus has been taken into account (increased) using the harmonic oscillator potential by Mayer and Haxel [May49], Jensen and Suess [Hax49], in the form of a spin-orbit interaction,

$$V_{SO} = -f(r)l.s \tag{2.6}$$

where, l and s are the orbital angular momentum and intrinsic spin quantum numbers for the single nucleons respectively, and $f(r)$, is the strength of interaction, which is given by

$$f(r) = \lambda \frac{1}{r} \frac{dV(r)}{dr} \tag{2.7}$$

The inclusion of a spin-orbit interaction, splits each degenerate level ($l \geq 1$) according to the orientation of the spin and orbital angular momentum coupling. Each state can be filled with the $2j + 1$ nucleons. This interaction lowers the energy of the $j = l + 1/2$ state relative to that of the $j = l$ - $1/2$ state for each allowed value of orbital angular momentum. The magnitude of the interaction (splitting) is proportional to the value of the orbital angular momentum (l). Therefore, the states of higher j, in the f, g, h and i levels, intrude to the top of the lower shells as the energy of the $l + 1/2$ state is lowered. The potential leads to a grouping of those intruder states with the opposite parity states in the lower shell and determines the maximum number of identical nucleons in each major shell. The energy levels are reordered to produce all the experimentally observed magic numbers, as shown in the right side of Figure 2.2. The spherical shell model achieved its success by explaining shell closures and the

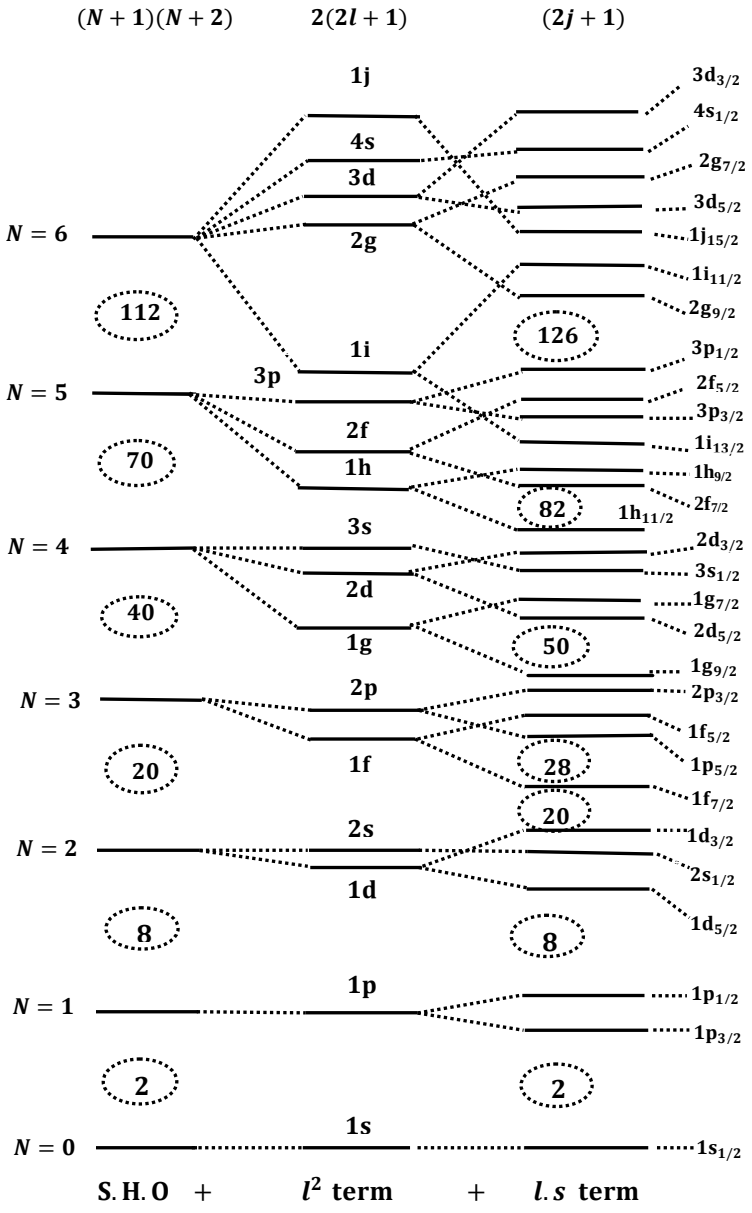

Figure 2.2: Single particle energy levels of the harmonic oscillator potential with the effects of l^2 term and spin-orbit interaction.

assignment spin and parity of nuclear states. It also predicts nuclear magnetic dipole and electric quadrupole moments of the (near) spherical nuclei near closed shells.

2.3.3 Woods-Saxon Potential

The Woods-Saxon (WS) potential is considered to be the most realistic form of the nuclear potential compared with the infinite square well and harmonic oscillator potentials. The shape of this finite potential is most likely as it follows distribution of the nuclear matter, smoothly vanishes outside the nucleus. It has the form [Woo54],

$$V_{WS}(r) = \frac{-V_0}{1 + exp^{\left[\frac{r-R_0}{a}\right]}} \tag{2.8}$$

where V_0 is the depth of the potential. R_0 and a are the radius and the surface diffuseness of the nucleus respectively. The Woods-Saxon potential will produce energy levels the same as of the harmonic oscillator potential with the l^2 term, and reproduce the correct magic numbers with the addition of a spin-orbit interaction.

2.4 Nuclear Deformation

The spherical shell model has been successful in predicting the single particle properties for nuclei near closed shells. Despite these successes, discrepancies have been observed between the theoretical predictions and experimental results with increasing numbers of nucleons outside closed shells. For instance, the nuclear quadrupole moment in the ground state has been found to change with nucleon number between major shells and is very large for certain nuclei. This behaviour is clear evidence for existence of static deformation in nuclei with atomic masses $A \cong 25$, $150 < A < 190$ and $A > 220$. Thus the nuclear potential deviates from its spherical symmetry to a deformed shape. The shape of a deformed nucleus can be parameterised through the expansion of the nuclear radius $R(\theta, \phi)$ in polar coordinates in terms of spherical harmonics $Y_{\lambda,\mu}(\theta, \phi)$,

$$R(\theta, \phi) = R_o \left(1 + \sum_{\lambda=0}^{\infty} \sum_{\mu=-\lambda}^{\lambda} \alpha_{\lambda\mu} Y_{\lambda\mu}(\theta, \phi)\right) \tag{2.9}$$

Where R_o is the radius of the sphere of the same volume of the deformed nucleus and $\alpha_{\lambda,\mu}$ are coefficients of multipole expansions that describe the distortions of the

nuclear surface with respect to the equilibrium shape. Coefficients of λ=0 and λ=1 corresponds to the conservation and translation of the nuclear volume respectively, were assumed to be equal to zero. The most significant deformations occur in nuclear shape with λ=2, quadruple deformation, which describes the elongation of axially symmetric shape of the nucleus. The five coefficients of $\alpha_{2\mu}$ can be written in,

$$\alpha_{20} = \beta_2 cos\gamma, \qquad \alpha_{21} = \alpha_{2-1} = 0, \qquad \alpha_{22} = \alpha_{2-2} = \frac{1}{\sqrt{2}}\beta_2 sin\gamma \tag{2.10}$$

where β_2 represents quadrupole deformation parameter of the nucleus and γ indicates the triaxiality of the nucleus and corresponds to the deviation from the axial symmetry. The various shapes of the nucleus in the (β_2, γ) coordinates can be represented by Lund conversion [And76], as in Figure 2.3. For quadrupole deformations, the axially symmetric collective shapes are prolate at $\gamma = 0°$ or oblate at $\gamma = -60°$, while the non collective shapes can be seen at $\gamma = -120°$ and $60°$ respectively. The triaxial shapes of the deformed nucleus along z-axis can be observed in the sector of the (β_2, γ) plane, when triaxial parameter changes between angles $0° < \gamma < 60°$.

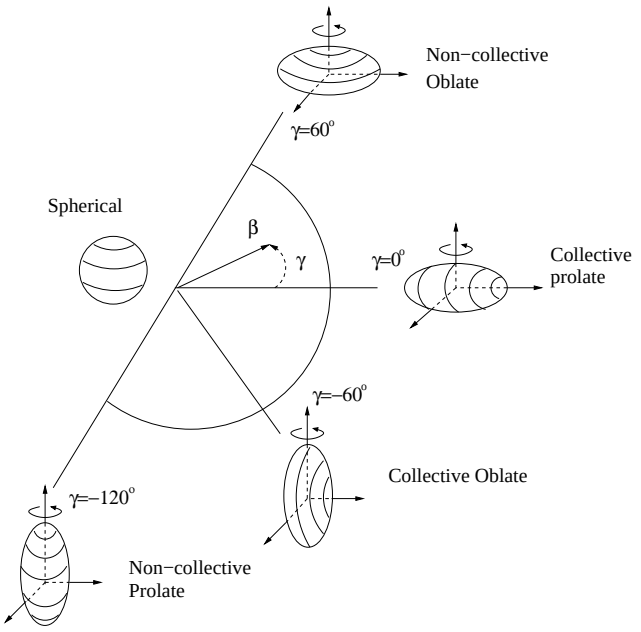

Figure 2.3: The Lund convention for the quadrupole deformation shapes in nuclei.

2.5 The Anisotropic Harmonic Oscillator Potential

The deformed potential is used to describe nuclei with shapes deviated from sphericity. The potential for axially symmetric nuclei along z-axis ($x = y \neq z$) is represented by anisotropic harmonic oscillator [Nil69],

$$V_{AHO} = \frac{1}{2}M\Big[\omega_{\perp}^2(x^2+y^2) + \omega_z^2 z^2\Big] \tag{2.11}$$

where $\omega_{\perp}$ and ω_z are the oscillator frequencies in the directions parallel and perpendicular to the symmetry axis respectively. They can be related to the oscillator frequency in the spherical case ω_0 and to the deformation parameter ε,

$$\omega_z \approx \omega_0\Big[1 - \frac{2}{3}\varepsilon\Big], \quad \omega_{\perp} \approx \omega_0\Big[1 + \frac{1}{3}\varepsilon\Big] \tag{2.12}$$

Thus, the oscillator frequencies ensure the volume conservation $\omega_0^3 = \omega_{\perp}^2\omega_z$. The oscillator frequency ω_0 can be deduced from the energy difference between two adjacent major shells and the expectation value of the nuclear radii for protons and neutrons [Won98],

$$\hbar\omega_0 = 41A^{-1/3}\Big[1 \pm \frac{N-Z}{3A}\Big] \qquad MeV \tag{2.13}$$

The numerical values for nuclear wave functions show that ω_0 has isospin dependence, so the positive sign used for neutrons and negative sign for protons. Nilsson [Nil55] transformed the problem of the anisotropic harmonic oscillator potential to stretched coordinates (ξ, η, ζ), in order to introduce the deformed potential in terms of the deformation ε_λ parameters and the angle of the stretched coordinates. The potential for the $\lambda = 2$ case is given by [Nil69],

$$V_{AHO} = \frac{1}{2}\hbar\omega_0(\varepsilon_2)\rho^2\Big[1 - \frac{2}{3}\varepsilon_2 P_2(cos(\theta_t)\Big] \tag{2.14}$$

The parameter ρ is defined as the radius in the stretched coordinates, $\rho^2 = \xi^2+\eta^2+\zeta^2$, $\theta_t = cos^{-1}(\frac{\zeta}{\rho})$, and ε_2 is the quadrupole deformation in the stretched coordinates, which is approximately equal to $0.95\beta_2$. To account for hexadecapole deformation

the $\varepsilon_4 \rho^2 P_4(cos\theta_t)$ term is added to the potential. The eigenvalues of the Hamiltonian for the anisotropic harmonic oscillator potential are given by:

$$E_{Nn_z n_\perp} \approx \left(N + \frac{3}{2}\right)\hbar\omega_0 - \frac{1}{3}\varepsilon(2n_z - n_\perp)\hbar\omega_0 \tag{2.15}$$

and

$$N = n_z + n_\perp \tag{2.16}$$

Where N is the major oscillator quantum, n_z is the number of oscillation quanta in the wave function along the symmetry axis. The single particle eigenstates in the deformed nuclear potential are labelled with asymptotic quantum numbers $[Nn_z\Lambda]\Omega^\pi$, Λ and Ω are the projections of the orbital and total angular momentum onto the symmetry axis respectively, and π is the parity of states identified by -1^N. The projection of total angular momentum on the symmetry axis is defined $\Omega = \Lambda \pm \Sigma = \Lambda \pm \frac{1}{2}$, where Σ is the projection of the intrinsic spin of the single particle onto the symmetry axis. Figure 2.4 illustrates this for a deformed axially symmetric nucleus in the absence of rotation.

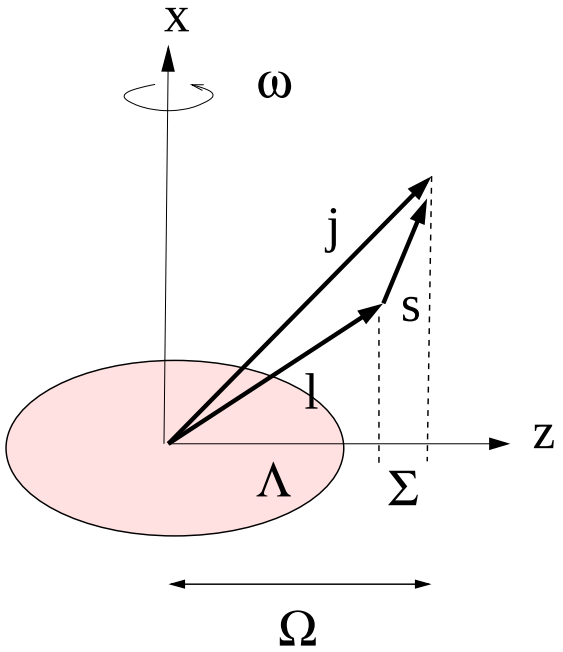

Figure 2.4: Illustration of the labelling of orbitals in the Nilsson model.

2.6 Nilsson Model

Nilsson introduced a unified nuclear model to describe the structure of the nucleus in a deformed potential and explain the behaviour of the single particle states with deformation. The potential that has been used in the Nilsson model is based on the anisotropic harmonic oscillator potential with contribution of a spin-orbit interaction and a l^2 term, which is known as Modified Harmonic Oscillator (MHO) potential or Nilsson Potential. Its most common form is written as;

$$V_{MHO} = V_{AHO} - \kappa\hbar\omega\Big[2l.s + \mu(l^2 - \langle l^2\rangle_N)\Big] \tag{2.17}$$

where κ and μ are adjustable coupling parameters, which are estimated for each major shell differently by fitting with the observed energy levels of the deformed nuclei experimentally. The $\kappa\hbar\omega[2l.s + \mu(l^2 - \langle l^2\rangle_N)$ term is added to reproduce the correct magic numbers and restore the spacing between two adjacent major shells as in the case of the spherical nucleus. Furthermore, the Nilsson potential splits each j shells in the spherical shell model at zero deformation into $j + 1/2$ and $j - 1/2$ states. Each state is specified by the projection of total angular momentum on the symmetry axis Ω and its parity π , which are the only conserved quantum numbers, and the states are twofold degenerate according to $\pm\Omega$. In the Nilsson model, the eigenvalues of Hamiltonian are represented as the diagrams of single particle energies of the nucleons as a function of quadrupole deformation, known as Nilsson diagrams. Figures 2.5 and 2.6 show Nilsson diagrams for neutrons and protons respectively. The energy of the eigenstates changes according to the spatial orientation of the orbits with respect to the nuclear symmetry axis. The levels of lowest Ω value are from the highest possible nodes of the wave function in the direction of the symmetry axis and their energies decrease with increasing prolate deformation, while the levels of higher Ω value are higher in energy and have a lower n_z value, ($N = n_z + \Lambda$, where Λ can be only 0 or 1 with a lowest energy level). On the other hand, for oblate deformation the low Ω eigenstates are of the higher energy than of the high Ω eigenstates. In Nilsson diagrams, the degenerated proton and neutron states arising from the same spherical j

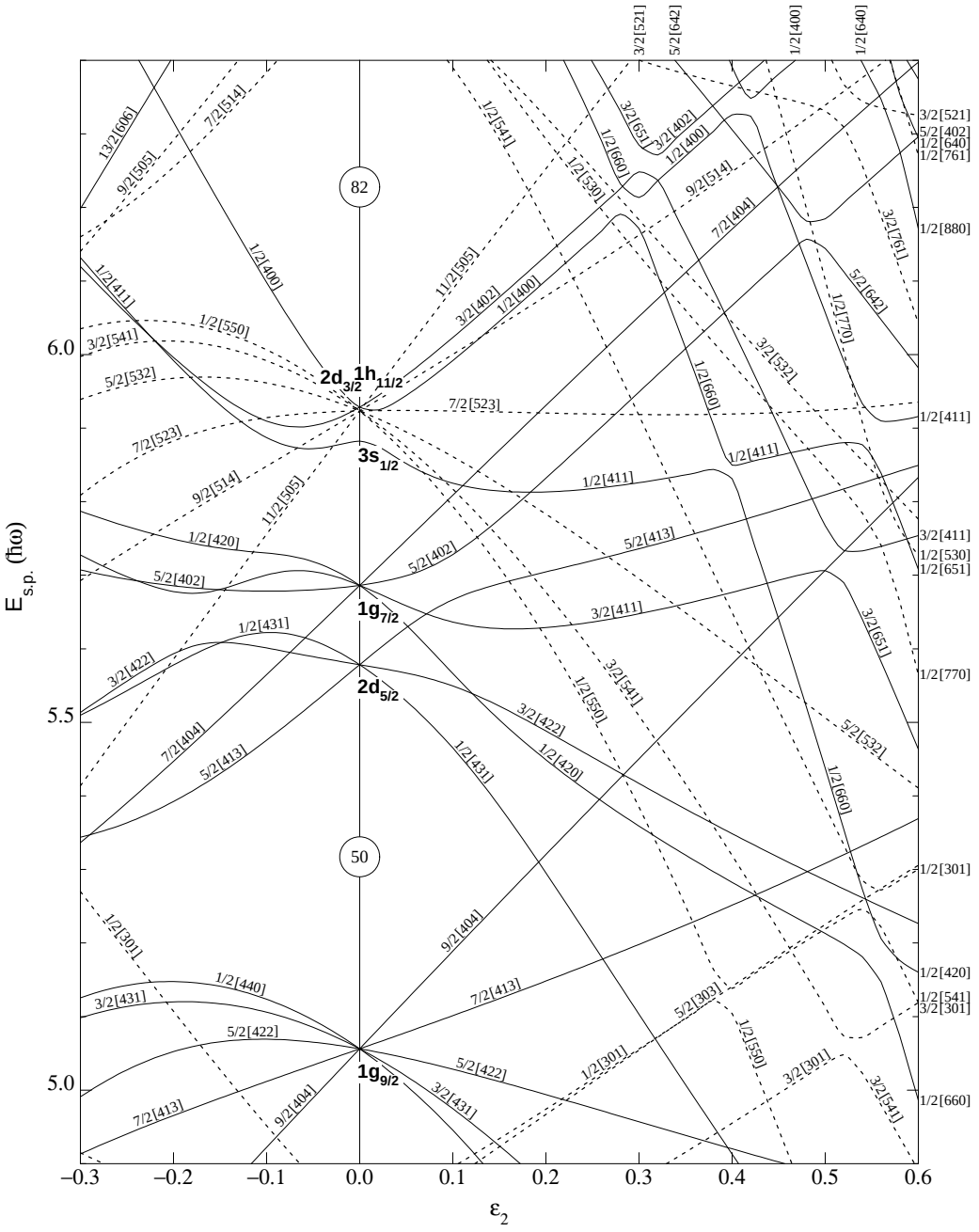

Figure 2.5: Nilsson diagram of single-neutron energies ($50 < N < 82$) as a function of the quadrupole deformation parameter ε_2. Full and dashed lines correspond to positive and negative parity respectively, [Fir96].

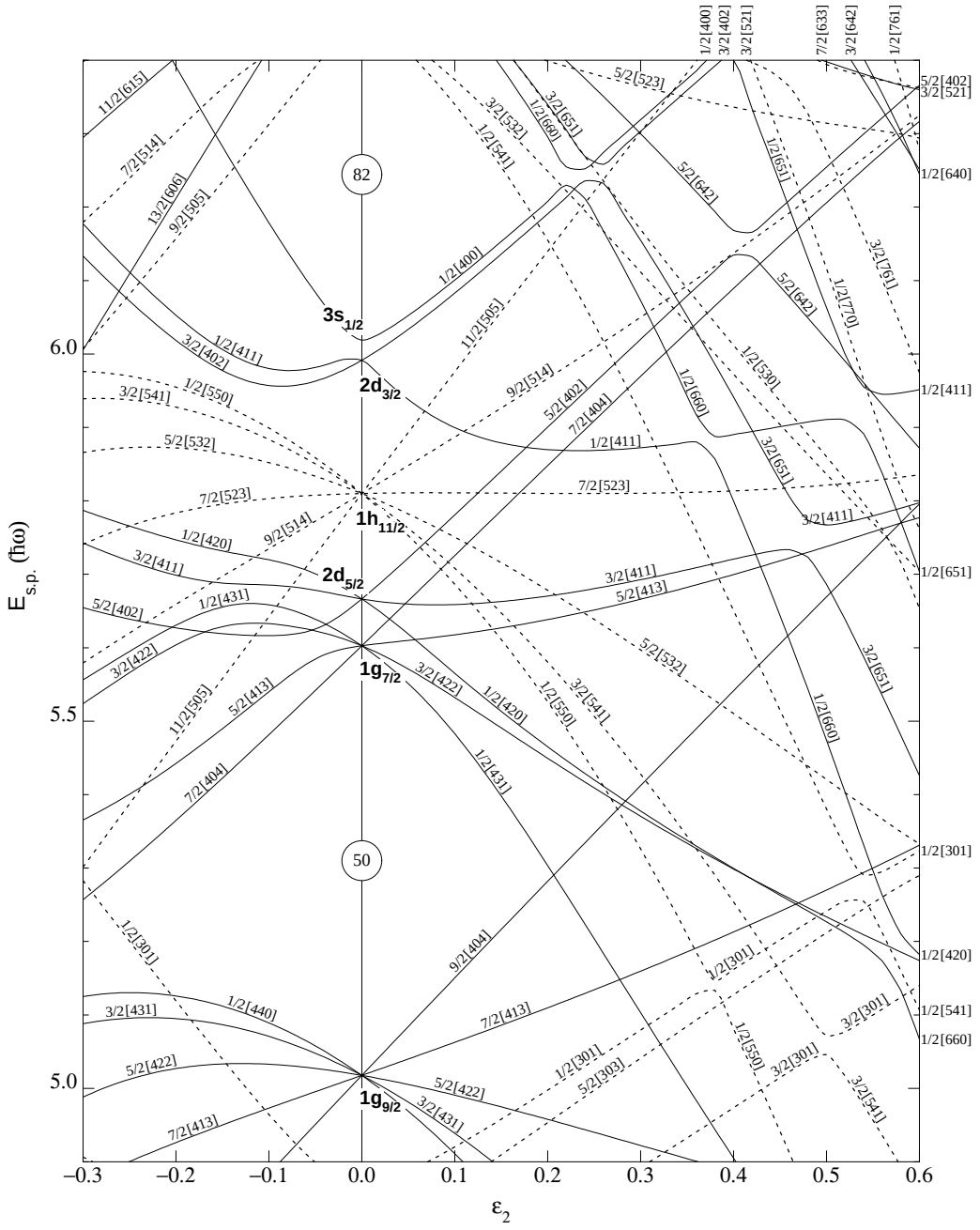

Figure 2.6: Nilsson diagram of single-proton energies ($50 < N < 82$) as a function of the quadrupole deformation parameter ε_2. Full and dashed lines correspond to positive and negative parity respectively, [Fir96].

shell are different in energy because of the isospin dependency of anisotropic harmonic oscillator. However at certain deformations low density regions of single particle states arises (deformed magic numbers) in the Nilsson spectra as a consequence of repulsive interaction between states of the same Ω^{τ}. These states approach each other and interchange the properties of their wave functions according to the Pauli Exclusion Principle.

2.7 The Strutinsky Shell Correction Procedure

In the previous sections, the nucleus has been described using two different concepts. The liquid drop model takes into account the contribution of all nucleons in the nucleus to calculate the nuclear binding energy and the macroscopic properties of the nucleus. In contrast, the shell model assumes that the protons and neutrons move in individual orbitals independently from one another in a certain average nuclear potential from all other nucleons in the nucleus. Particular nuclear properties can be identified from the behaviour of the specific single particles near to the Fermi surface. It is clear that both models ignore the influence of each other in the calculation of the total energy of the nucleus. This discrepancy led Strutinsky to propose the shell correction procedure [Str67, Str68] to obtain accurately the total energy of the nucleus and the nuclear ground state energies as a function of deformation. The shell correction procedure combines the successful features of the two models, in which, Strutinsky added an oscillatory energy from the microscopic shell model to the predicted nuclear binding energy from the liquid drop model.

$$E = E_{LDM} + \Delta E_{shell} \tag{2.18}$$

This oscillatory energy (ΔE_{shell}) arises from the fact that the nuclear binding energy per nucleon depends on the level density close to the Fermi surface. In the shell model the energy levels are grouped together with a separation between the major shells. When the Fermi surface is located near a region of low level density the binding energy of the nucleus is stronger than when it is near a region of high level density.

This correction in the model enabled the nuclear ground state energies as a function of deformation to be determined accurately, which are generally presented in the form of the potential energy surfaces of the nucleus.

2.8 Pairing and Quasiparticles

The pairing correlation is the characteristic of the strong nuclear force in the form of a short-range component between any two nucleons, which originates from the spatial overlap of the identical particles with the same quantum numbers and opposite spins, consequently their angular momenta couple to $I = 0$. The inclusion of the pairing interaction to the nuclear structure model was the key answer for a number of outstanding experimental observations, which could not be interpreted in the framework of the single particle shell models. For instance;

- The spin and parity (I^{π}) of the ground state in all even-even nuclei is 0^{+}.
- The energy difference between the first non-collective excited state and the ground state in even-even and even-odd nuclei.
- The differences in masses and binding energies of even-even and even-odd nuclei are related to the odd-even effect, the role of the last nucleon in the pairing regime. The masses of odd-even nuclei are higher than the average mass of the two neighbouring even-even nuclei, while in even-even nuclei all nucleons are paired and have higher binding energies.
- Nuclei in the region near the closed shells or close to closed shells preserve a spherical shape, because the influence of the pairing force overcomes the tendency to deform.
- The moment of inertia of rotational band structures at low spin in deformed nuclei are approximately one third of the calculated value of the rigid-body rotor.

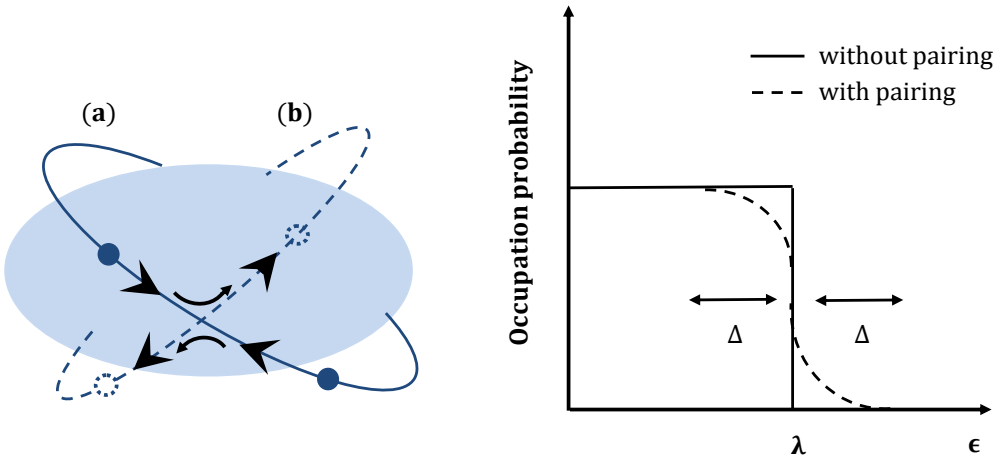

Figure 2.7: The left figure illustrates a pair of nucleons in time reversed orbital (a), scattered into another time reversed orbital (b). The figure on the right side illustrates the single particle occupation probability as a function of single particle energy and explains the effect of pairing correltion on the Fermi surface.

The Pauli Exclusion Principle does not allow paired particles to orbit in the same level, so each nucleon in a pair orbits in the time reversed orbits and to complete one orbit they scatter twice into free orbits of a different energy state near to the Fermi surface, as illustrated in Figure 2.7. Thus the scattered pairs in the time reversed orbits smear the Fermi surface in the energy domain over an energy of twice the pairing gap (Δ), and this simultaneous interaction process will produce a mixture of occupied (particle) and unoccupied (hole) states below and above Fermi surface.
This scattering model is considered as the fundamental concept to introduce quasi-particles, which represent the partially occupied (particle-hole) states with unity occupation probability in terms of the probability of fullness V_i^2 and emptiness U_i^2 of the orbits. Therefore the particle-hole excitation is replaced by the simultaneous creation and annihilation operator of quasiparticles. The quasiparticle energy of a state i in the presence of paring interaction is given by;

$$E_i = \sqrt{(\epsilon_i - \lambda)^2 + \Delta^2} \tag{2.19}$$

where, ϵ_i is the single-particle energy, λ is the Fermi energy and Δ is pair gap which has different values for protons and neutrons. It is of lower value for former because of the repulsive Coulomb interaction.

Chapter 3

Nuclear Rotation

3.1 Introduction

Rotation of spherically symmetric nuclei in space is forbidden in quantum mechanics, as those nuclei are invariant under rotation. When the shape of nucleus deviates from spherical symmetry, as shown in Figure 3.1, it possesses a deformed shape and rotates around one of the axes (x or y) perpendicular to the symmetry axis (z). Hence, the angular momentum of the rotated nuclear system is generated in two different mechanisms, non-collective excitation of unpaired valence nucleons and collective excitation of the rotating core (paired nucleons). Therefore, this chapter will introduce some basic concepts of nuclear rotation and discuss the interplay between collective and single particle modes to describe nuclear structure phenomena observed from the experimental spectra of the rotating nucleus.

3.2 Non-Collective Single Particle Excitation

In the region close to the closed shells, nuclei have spherical or near spherical shapes. Nuclear angular momentum in these nuclei is only generated non-collectively, by the alignment of the individual spins of the valance nucleons along the rotation axis which coincides with to the symmetry axis, as shown in Figure 3.2a. This mechanism gives

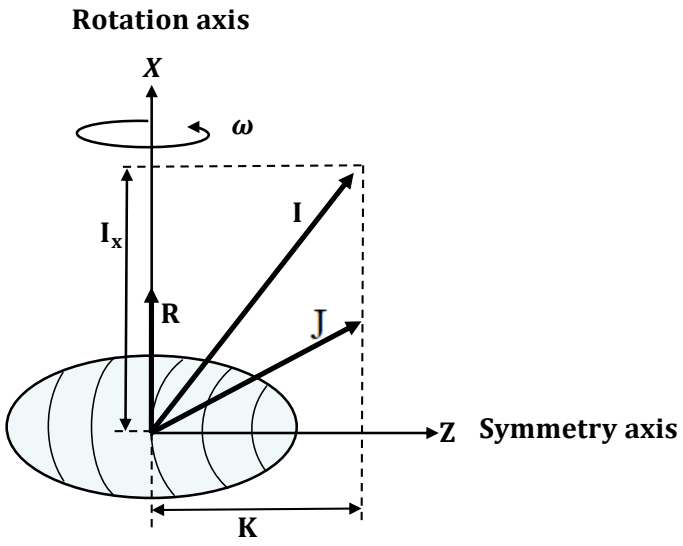

Figure 3.1: Illustrates rotation of an axial symmetric nucleus around an axis perpendicular to the symmetry axis, and its angular momenta projections.

rise to a large value of total angular momentum (J) of the nucleus corresponding to the sum of the single particle contributions of high j and large Ω orbitals near to the Fermi surface. Nuclear excited states that are based on this mode of angular momentum generation are known as single particle excited states which can be observed in both spherical and deformed nuclei.

3.3 Collective Excitation

The deformed nucleus rotates collectively around an axis perpendicular to the symmetry axis. All nucleons in the rotating core contribute to generate angular momentum coherently, which increases with rotational velocity of the nucleus. The total angular momentum of the nucleus, is identified from the vector coupling of angular momenta which is generated by the single particle contributions of the valance nucleons J, and of the rotated core R, as illustrated in Figure 3.1.

$$\mathbf{I} = \mathbf{R} + \mathbf{J} \tag{3.1}$$

The projection of total angular momentum onto the rotation axis I_x is defined as;

$$I_x = \sqrt{I(I+1) - K^2} \tag{3.2}$$

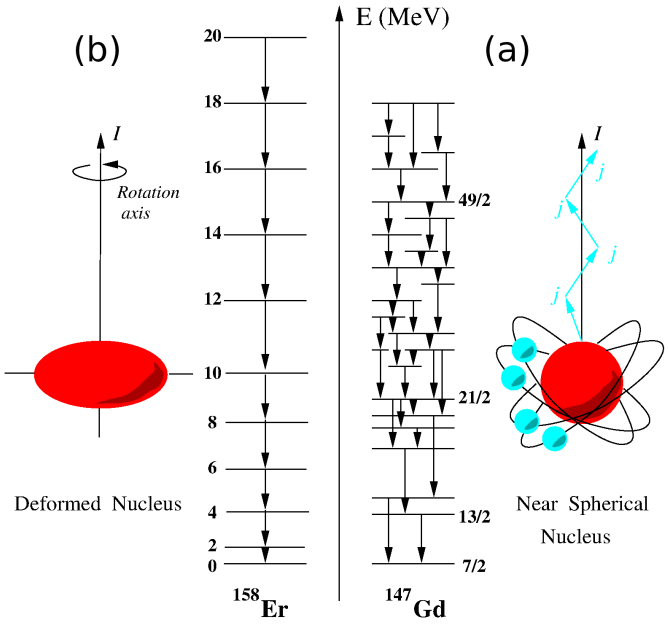

Figure 3.2: (a) Generation of angular momentum and single particle excite states in a near spherical nucleus ^{147}Gd as a consequence of single particle excitation. (b) Collective rotation in a deformed nucleus to generate angular momentum collectively and exhibit a rotational band in ^{158}Er.

Where, K is the projection of total angular momentum onto the symmetry axis. The collective rotation of an axially symmetric deformed nucleus exhibit different sequences of rotational spectra between successive sets of intrinsic nuclear excited states, known as rotational bands of different static moment of inertia $\mathcal{J}$, their energies are given by:

$$E(I,K) = \frac{\hbar^2}{2\mathcal{J}}[I(I+1) - K^2] \tag{3.3}$$

Single nucleons can not build angular momentum in even-even deformed nuclei up to spin 10-12$\hbar$, because all nucleons are paired in the ground state. For K=0 band, rotational energy in the above relation can be expressed as:

$$E(I) = \frac{\hbar^2}{2\mathcal{J}} I(I+1) \tag{3.4}$$

In a rotational band,as shown in Figure 3.2b. A transition occurs between any two successive states separated by angular momentum of 2$\hbar$, which leads to the emission

of gamma-ray with energy,

$$E_\gamma = E(I) - E(I-2) = \frac{\hbar^2}{2\mathcal{J}}(4I-2) \tag{3.5}$$

3.4 Rotational Frequency and Moment of Inertia

In the experimental investigation of high spin states, the behaviour of a rotating deformed nucleus is usually described in terms of rotational frequency. The rotational frequency is related to the energy difference between successive states of a rotational band, and approximately equal to half the energy of the emitted gamma-ray [Ray73];

$$\hbar\omega = \frac{dE}{dI_x} = \frac{\Delta(E_I - E_{I-2})}{\Delta I} = \frac{E_\gamma}{2} \tag{3.6}$$

This quantity varies with angular velocity, as a consequence of the changes that occur in the structure of a deformed nucleus during rotation. So, to explain the behaviour of rotating deformed nucleus, Bohr and Mottelson [Boh81] introduced kinematic $\mathcal{J}^{(1)}$ and dynamic $\mathcal{J}^{(2)}$ moments of inertia. The kinematic moment of inertia describes the rotating system of the deformed nucleus and is defined as:

$$\mathcal{J}^{(1)} = \left[\frac{2}{\hbar^2}\frac{dE(I)}{dI_x}\right]^{-1} = \hbar\frac{I}{\omega} \tag{3.7}$$

The dynamic moment of inertia $\mathcal{J}^{(2)}$ explains the influence of competition between interactions that are taking place in the structure of rotational bands in a deformed nucleus during rotation, and is defined as:

$$\mathcal{J}^{(2)} = \left[\frac{1}{\hbar^2}\frac{d^2E(I)}{dI_x^2}\right]^{-1} = \hbar\frac{dI}{d\omega} \tag{3.8}$$

$\mathcal{J}^{(1)}$, can be related to energy of the gamma-ray emitted in the rotational band for a given spin value,

$$\mathcal{J}^{(1)} = \hbar^2\frac{(2I-1)}{E_\gamma} \tag{3.9}$$

In addition, $\mathcal{J}^{(2)}$ can be calculated from the energy difference between of consecutive gamma-ray,

$$\mathcal{J}^{(2)} = \frac{4\hbar^2}{\Delta E_\gamma} \tag{3.10}$$

Therefore, it is clear that $\mathcal{J}^{(2)}$ does not depend on the spins of the excited states of the rotational band.

3.5 Particle-Rotor Coupling

The particle-rotor model [Ste72] is based on the prediction of Mottelson and Valatin [Mot60] for the Coriolis force. When the deformed nucleus rotates around the axis perpendicular to the symmetry axis, this Coriolis force tries to decouple the valance nucleons that are bound to the rotating deformed core of the nucleus. The maximum Coriolis force exerted on a particular valence nucleon with angular momentum j, in the potential of a deformed rotating nucleus of total angular momentum I can be defined as [Ste75],

$$\mathbf{E_{Cor}^{max}} \approx (\frac{\hbar^2}{\mathcal{J}})\mathbf{J}.\mathbf{I} \tag{3.11}$$

The above relation illustrates that the nucleons in high j orbitals (intruder orbitals) are very sensitive to this force. In the particle rotor model, the motion of nucleonic system (a valence nucleon and a core of the paired nucleons) is only constrained by the strength of the potential of the deformed core and the Coriolis force which is induced by the rotation of the nucleus. There are two different coupling limits: the deformation aligned limit (DAL) and the rotational alignment limit (RAL). Figure 3.3 illustrates the two coupling limits.

In the case of deformation aligned limit (DAL), when the nuclear system rotates slowly, the Coriolis force is not strong enough to overcome the potential strength of the rotating nuclear core. The strength of the latter is still sufficiently high to maintain motion of the unpaired valance nucleon with the deformation of the core. In addition, the coupled pairs of valence nucleons with opposite spins are oriented along the symmetry axis of the deformed potential. Thus, the angular momentum vector j of the unpaired nucleon precesses around the symmetry axis of the deformed potential of the rotating nucleus, as shown in Figure 3.3a. When, the angular velocity of the rotating nuclear system becomes higher compared to the internal nucleon motion,

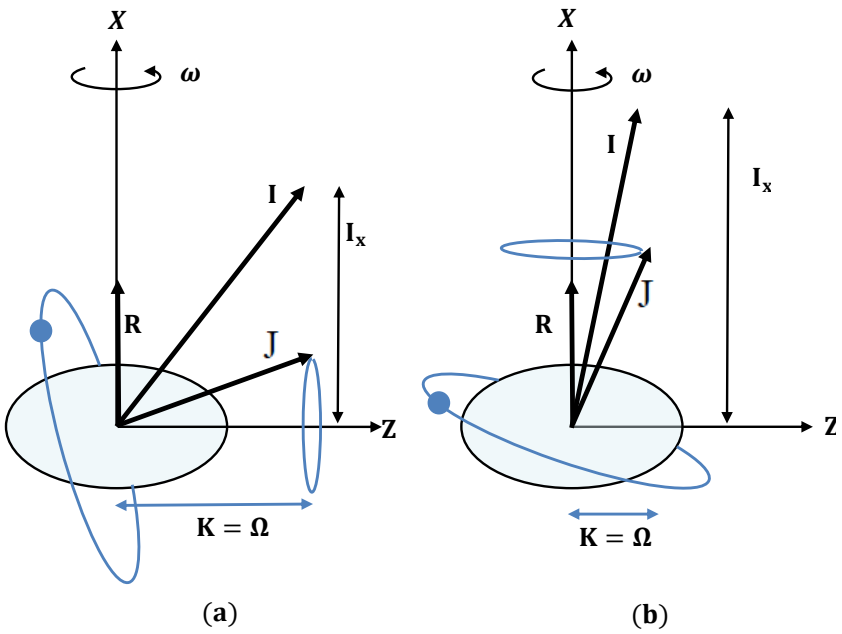

Figure 3.3: Particle rotor coupling scheme (a) Deformation aligned and (b) Rotational alignment.

the rotational frequency will increase as well as the Coriolis force which predominates over the deformed potential of the core. The unpaired valence nucleon is affected by the Coriolis force, and it will be decoupled from the deformed core and finally its angular momentum vector j couples with the rotation axis of the potential of the rotating uncles. The coupling scheme in the rotating nuclear system changes to the rotational alignment limit (RAL) as shown Figure 3.3b. Moreover, the Coriolis force becomes strong enough to act on the angular momenta of the paired valence nucleons and decouples the pairing correlation between the two nucleons. The paired nucleons in high j, low Ω orbitals will be affected first. Consequently the angular momenta of the decoupled pair of nucleons aligns with the collective angular momentum of the rotating core, along the rotation axis of the deformed potential. This results in a decrease in the rotational frequency and an increase in the moment of inertia of the rotating nucleus. This causes the back-bending phenomena [Joh71, Gro73] in the structure of the rotational band. This mechanism can generate angular momentum up to ultra-high spins.

3.6 The Cranking Model

The Cranking model was introduced by Inglis [Ing54, Ing56], to explain the microscopic description of behaviour of the rotating nucleus around an axis of rotation, perpendicular to the symmetry axis, under influence of a deformed nuclear potential field along the symmetry axis. In the Cranking model single-particle and collective excitations of the nucleus are taken into account as independent particles moving in a rotating potential with constant angular velocity ω. The energy of independent single particles in the rotating system has been identified by using a cranking Hamiltonian (Routhian). The transformation of the intrinsic coordinate system to the rotating frame reference is through the rotation operator.

$$\hat{\mathbf{R}}_x = \exp^{-i\omega t i_x} \tag{3.12}$$

The cranking Hamiltonian for an independent single particle takes the following form:

$$h^{\omega} = h_{int} - \hbar\omega i_x \tag{3.13}$$

The cranking Hamiltonian over all the independent single particles of the system defines the total cranking Hamiltonian of the rotating nucleus as,

$$H^{\omega} = \sum h^{\omega} = H_{int} - \hbar\omega I_x \tag{3.14}$$

Where, H_{int} is sum of the single particle Hamiltonians in the intrinsic frame of reference, and I_x represents the sum of the projections of all single particle angular momenta onto the rotation axis. The term $\hbar\omega I_x$ in the above equation represents Coriolis and centrifugal forces in the rotating coordinate system. The effect of this term has been taken into account for single particle energies of the deformed shell model (Nilsson model) by Bengtsson and Frauendorf [Ben79], and introduced in the form of the Cranked Shell Model (CSM). The various forms of CSM [Naz85, Cwi87] can be used to interpret the structure of nuclei at high angular momentum, in terms of quasiparticle configurations and either quasiparticle or single particle Routhains for protons and neutrons independently, as in the case of ^{159}Er that will be presented in chapter six.

3.7 Nuclear Symmetries

In the introduction of rotation to an axially symmetric nucleus, the two fold degeneracy of Nilsson orbits with respect to time reversal symmetry ($\pm\Omega$) is broken by the Coriolis force and results in Nilsson orbits split into two single particle levels. The splitting between the two levels depends on the projection of the single particle angular momentum onto the rotation axis corresponding to that orbit, and increases with rotational frequency. Consequently, the only remaining symmetries for the cranking Hamiltonian are invariance with respect to the spatial reflection and with rotations of 180° around the axis of rotation. These two symmetries are called parity (π) and signature (α). They label the nuclear states of the rotating nucleus, and will be outlined in next two sections. A schematic illustration of the effect of cranking on the single particle energy levels of Nilsson orbits originating from principal quantum number N=2, in a harmonic oscillator potential is illustrated in Figure 3.4.

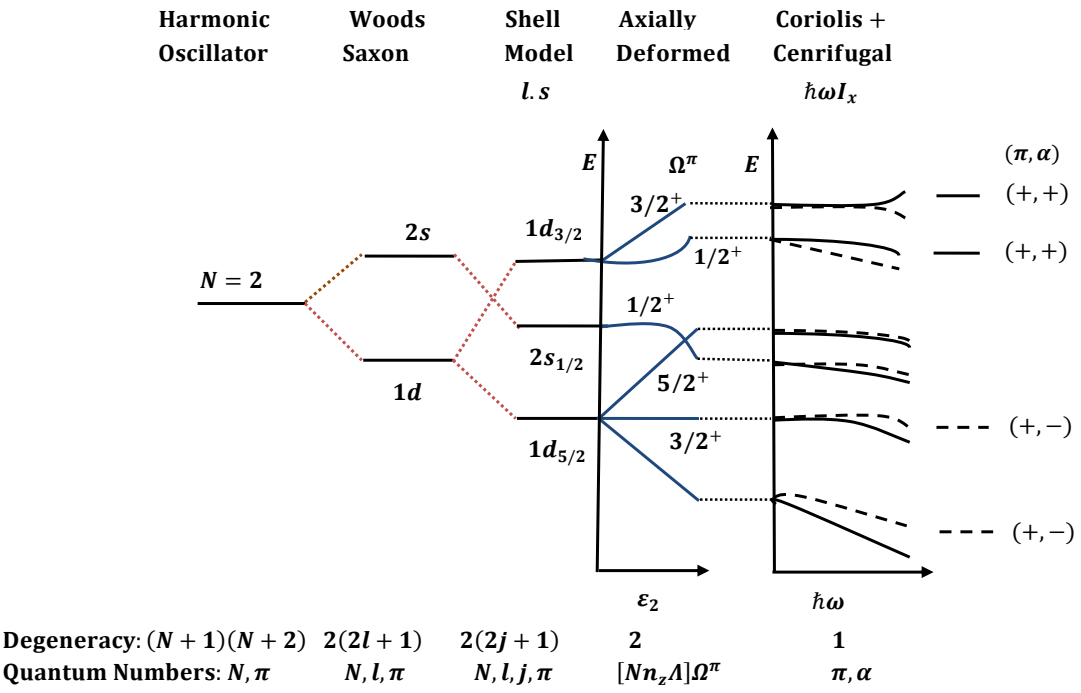

Figure 3.4: Illustration of the effects of cranking on the remaining symmetries that describe a particular configuration of nucleons.

3.7.1 Parity

Parity is an operator which describes the reflection symmetry through the origin of the spatial part of particle wavefunction relative to all coordinates. The eigenvalues of the parity operator $\hat{\pi}\psi(-\vec{r})$ have two values, firstly;

$$\psi(-\vec{r}) = +\psi(\vec{r}) \tag{3.15}$$

The reflected wavefunction remains unchanged and the parity will be even, then the parity of single particle state is labelled +, and if;

$$\psi(-\vec{r}) = -\psi(\vec{r}) \tag{3.16}$$

this means that the reflected wavefunction is inverted and parity is odd. Here the parity of single particle state is labelled −. The total parity of a nuclear state is given by the product of the parities of all occupied single particle orbitals:

$$\pi_{total} = \prod_{occ} \pi_i, \tag{3.17}$$

3.7.2 Signature

Signature arises from the invariance of the cranking Hamiltonian with respect to a rotation of 180° around the x-axis through the rotation operator $\hat{\mathbf{R}}$ [Syz83],

$$\hat{\mathbf{R}}_x = \exp^{-i\pi I_x} \tag{3.18}$$

The eigenvalues (r) of the rotation operator, result in the signature exponent quantum number (α),

$$r \equiv \exp^{-i\pi\alpha} \tag{3.19}$$

The allowed values of eigenvalues are restricted to the total number of nucleons in the rotating nucleus that are of even or odd A.

For even-A nucleus, r takes values +1 and −1 with $\alpha = 0$ and 1 respectively, giving rise to nuclear states of spin

$$I = 0, 2, 4, 6, ... \tag{3.20}$$

$$I = 1, 3, 5, 7, ... \tag{3.21}$$

Whereas for odd-A nucleus, r has values $-i$ and $+i$ with $\alpha = +\frac{1}{2}$ and $-\frac{1}{2}$ respectively,

$$I = \frac{1}{2}, \frac{5}{2}, \frac{9}{2}, \frac{13}{2}, ... \tag{3.22}$$

$$I = \frac{3}{2}, \frac{7}{2}, \frac{11}{2}, \frac{15}{2}, ... \tag{3.23}$$

The split energy levels from Nilsson states are signature partners, which have been labelled with two opposite signature exponent quantum numbers, as shown on the right in Figure 3.4. The energy levels labelled with $+$, are known as favoured signature. While those labelled with $-$, are known as unfavoured signature.

Chapter 4

Experimental Details

4.1 Introduction

The following chapter will describe the reaction carried out to populate the excited states in ^{159}Er up to ultra high spin. The interactions in the detection system used during the experiment will also be discussed. In addition, the spectroscopic techniques that were employed in the work to identify and study the nuclear structure of the populated nucleus will be outlined.

4.2 Heavy Ion Fusion Evaporation Reaction

The Heavy Ion Fusion Evaporation Reaction has been employed to populate the highest spin states in nuclei [New70]. Niels Bohr in 1936 proposed using the fusion mechanism of projectile on target in nuclear reactions to form a compound nucleus [Boh36]. In fusion, the projectile beam of heavy ions may fuse with the target nucleus to form a highly excited compound nucleus at high spin, provided that the centre of mass energy is sufficient to overcome the Coulomb barrier between projectile and target nuclei [Hod78]:

$$E_{CB} = \frac{Z_p Z_t e^2}{R_{CB}} MeV \tag{4.1}$$

Where $Z_p e$ and $Z_t e$ are the total positive charge (atomic number) of the projectile and target nuclei respectively, and R_{CB} represents the Coulomb interaction radius, which corresponds to the separation distance between the centres of the projectile and target nucleus in unit of fm (10^{-15}m), the best approximation of interaction radius may be expressed as [Hod78]:

$$R_{CB} = 1.35(A_p^{1/3} + A_t^{1/3} + 0.5)fm \tag{4.2}$$

A_p and A_t represent the mass number of the projectile and target nuclei respectively. When the impact parameter (b) of the new compound system is equivalent to separation distance (Coulomb interaction radius), R (R is constrained to be smaller than the glancing collision illustrated in Figure 4.1), the reaction mechanism brings the maximum angular momentum to the compound nucleus system. The l_{max} is given by [Dia80]:

$$l_{max} = 0.219(R_p + R_t)\sqrt{\mu(E_{CM} - E_{CB})} \tag{4.3}$$

The parameters R_p, R_t, μ, E_{CM} and E_{CB} in equation 4.3 are the radii of the projectile and the target, reduced mass, bombarding energy of the projectile and Coulomb barrier energy in the centre of mass system in units femtometere, MeV/C^2 and MeV respectively.

The different stages of the reaction process, for formation and decay of the compound nucleus as explained by Bohr, to populate ^{159}Er nuclus are shown in Figure 4.2. Fusion of the projectile beam occurs first after a series of successive collisions between individual nucleons, which takes a period of time equal to the time taken for the incident particle to travel across the diameter of the target nucleus. The compound system is highly excited and carries a large amount of angular momentum. During the formation period (approximately 10^{-22} sec), its kinetic energy is shared uniformly among all constituent nucleons until the system has no "memory "of its mode of formation. The decay mode of the compound system is independent of the formation mode if the two modes are separated in time by a period of about 10^{-19} sec. Particle emission occurs, while the excitation energy remains higher than the separation energy of alphas, protons, or neutrons.

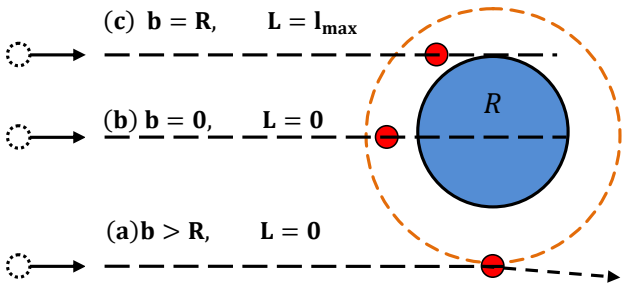

Figure 4.1: Schematic illustration of the dependance of angular momentum of the nuclear excited system on the impact parameter (b) and the separation distance (R) between the centres of colliding nuclei.

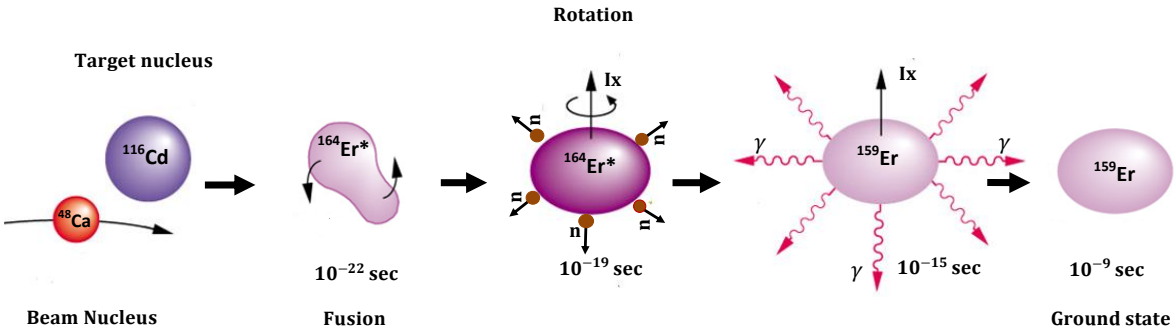

Figure 4.2: Various stages with time scales of the heavy ion fusion evaporation reaction for product nucleus ^{159}Er.

In each step of the de-exatation process (evaporation of nucleons) the evaporated particle removes one or two units of angular momentum and an amount of excitation energy equal to the sum of separation energy and kinetic energy of the evaporated particle.

When the width of the region between yrast line and the entry line reduces to the threshold value ($\approx$ 8 MeV), the excitation energy of the compound nucleus becomes less than the neutron separation energy. Here, the compound nucleus begins to emit

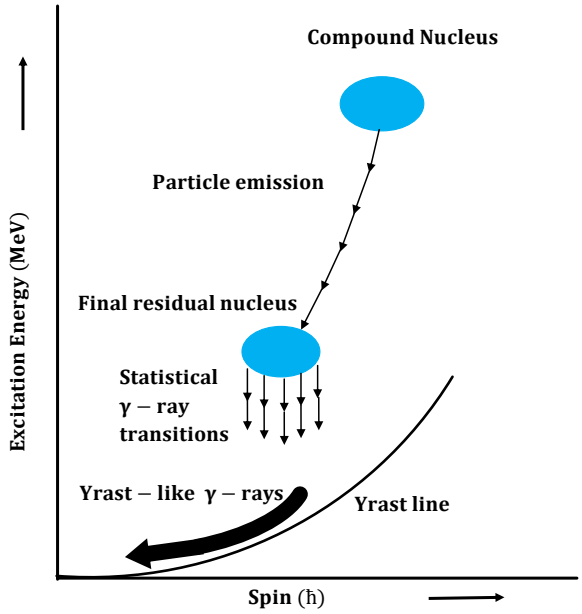

Figure 4.3: Schematic illustation of the de-excitation modes of highly excited compound nucleus.

statistical gamma-rays due to high density of states, that cool the product nucleus toward the yrast line. These gamma-rays are usually of electric dipole character. Then the compound nucleus, with high angular momentum, decays by Yrast-like gamma ray emission through the yrast path (which connects the states with lowest energy levels in the nucleus for each spin value) towards the ground state as in Figure 4.3. Most discrete gamma rays arise from yrast levels with an energy distribution ranging from zero to a few MeV above the yrast line. Due to the competition of varied reaction channels, the product nucleus in its ground state depends on the probability of particle evaporation.

4.3 Gamma-ray Interaction Processes with Matter:

In the detection system, gamma-rays interct with matter, leading to either a total or partial transfer of gamma-ray energy through an atomic electron within the absorber. There are three main interaction processes, which depend on the energy of incident gamma ray and the properties of the absorber material; photoelectric absorption, Compton scattering and Pair production. The gamma-ray interaction processes are outlined in the following sub-sections, for more details see reference [Kno10].

4.3.1 Photoelectric Absorption

Photoelectric absorption is the most probable interaction process at low gamma-ray energies below 0.2 MeV for Z 32 (Ge), in which, the gamma-ray energy is totally absorbed by a bound inner atomic electrons near the nucleus. Consequently, an electron is liberated from the atom with a kinetic energy by:

$$T_e = E_\gamma - E_B \tag{4.4}$$

Where, E_B is the binding energy of the ejected electron in the atom. The photoelectron energy represents the gamma ray energy in the detection system as the photopeak energy. The liberation of a photoelectron leaves a vacancy in the atomic shell, that is immediately filled by an electron from the outer shells resulting in emission of characteristic X-ray or Auger electrons. The probability of photoelectric absorption depend on the atomic number of the absorber materials and the gamma ray energy which is given by ($\sigma_{ph} = \frac{Z^n}{E_\gamma^{3.5}}$). Where n varies betwen 4 and 5 over the gamma ray region of interest. The photoelectric absorption process schematically illustrated in Figure 4.4(a).

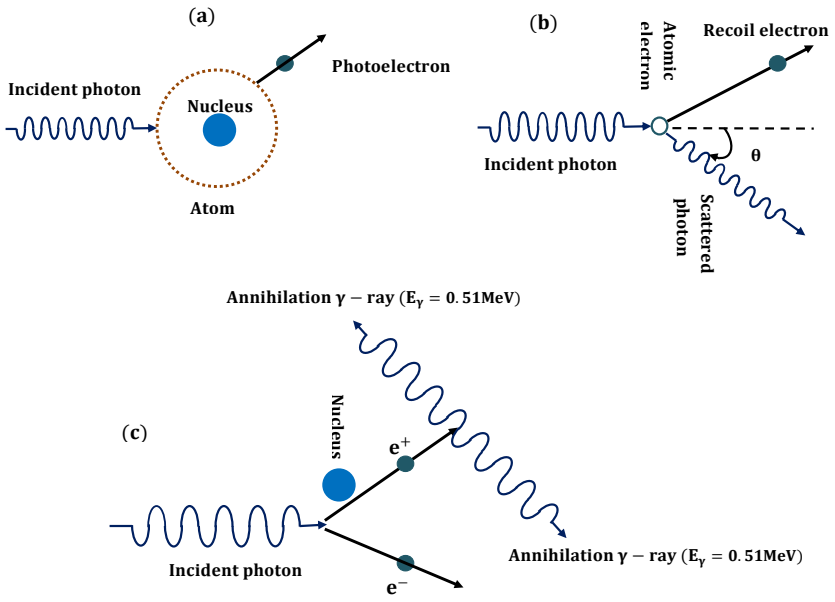

Figure 4.4: Schematic illustation for the interction processes of gamma-ray with matter, (a) photoelectric absorsorption, (b) Compton scattering and (c) pair production.

4.3.2 Compton Scattering

Compton scattering is most probable in the gamma-ray energy domain, 0.2 MeV $\leq E_\gamma \leq$ 10 MeV, in which, the incoming photon (gamma-ray) collides with an electron of the most outer atomic shells in the absorber within the detector. The electron recoils from its orbit and the gamma-ray energy is partially imparted to the electron. The incoming photon is then scattered through an angle, θ from its original direction and has a reduced energy. The scattering process is considered as an elastic collision as illustrated in Figure 4.4(b), and the energy of the scattered photon can be related to the scattering angle using conversation of energy and momentum:

$$E_\gamma^{'} = \frac{E_\gamma}{1 + \frac{E_\gamma}{m_o c^2} \cos\theta} \tag{4.5}$$

$E_\gamma^{'}$ and E_γ are represent the energy of the scattered and incident photon, $m_o c^2$ is the rest mass energy of the atomic electron and θ is the angle between the incoming and

the scattered directions of photon. The probability of a gamma-ray interaction via Compton scattering is directly proportional to the atomic number (Z) of the absorber material, as well as depending on the number of electrons in the scattering process.

4.3.3 Pair Production

Pair production is the process of gamma-ray interaction with an atomic electron surrounded by the Coulomb field of the nucleus; this interaction is energetically possible if the gamma-ray has energy more than of 1.022 MeV, the gamma-ray completely disappeared and an electron- positron pair is created. The excess energy from the creation process is carried off in the kinetic energy of the electron and positron:

$$E_\gamma = 2m_o c^2 + E_{e^-} + E_{e^+} \tag{4.6}$$

The created particles slow down in the absorber material and upon stopping, the positron annihilates with another electron producing two back to back annihilation gamma-rays each with an energy 0.511 MeV. This process is illustrated in Figure 4.4(c). The probability of pair production depends on the gamma-ray energy being above the threshold energy (1.022 MeV), and its proportional to the square of the atomic number (Z^2) of the absorber material.

4.4 Gamma-ray Detectors

Various types of gamma-ray detection systems have been developed to obtain information on nuclear structure physics through the measurements of the gamma-rays emitted either from radioactive sources or from the de-excitation of a nucleus after the occurence of a nuclear reaction. The following sections describe the properties of the detectors, which have been used in the design of the Gammasphere array, built to study high-spin gamma-ray spectroscopy.

4.4.1 Scintillation Detectors

The most commonly used scintillation detectors for this work are thallium-activated sodium iodide NaI(Tl) and bismuth germinate $Bi_4Ge_3O_{12}$ (BGO). The large atomic numbers of iodine (Z= 53) and bismuth (Z= 83), give a high probability of interaction within the scintillation materials for gamma-ray photons. The absorbed gamma-ray energy causes the excitation of electrons from the valence band to the conduction band of the inorganic scintillator crystals. The excitation and subsequent de-excitation of an electron causes the emission of visible light in the scintillation processes. In the case of NaI(Tl), the small amount of thallium impurity is used as an activator to promote the rate of light emission, whereas the BGO detectors do not require the activators to enhance the scintillation processes.

The scintillation light is converted into electric pulses through a photomultiplier tube. Here, the photoelectric interaction occurs with a photosensitive surface, and produces photoelectrons directed to the electron multiplier. After a series of electron multiplications, the output current is proportional to the gamma-ray energy deposited in the detector material.

For same size scintillation detectors, BGO detectors are of higher efficiencies than NaI(Tl) detectors, because of the high density density (7.13 gm/cm^3) and atomic number of bismuth component. On the other hand a NaI(Tl) detector has a better energy resolution than a BGO detector, where typically the resolution at 0.662 MeV (^{137}Cs) is 6-7% for Na(Tl). Scintillation detectors, typically BGO, mainly contribute in the design of multi-detector arrays as escape suppression shields.

4.4.2 High-Purity Germanium (HPGe) Detectors

In Germanium detectors, the interaction of ionising radiation (gamma-rays) occurs within the depletion region of the reverse biased p-n junction. The required energy to produce an electron-hole pair in this type of detectors is small (around 3eV). For a specific amount of gamma-ray energy deposited, a large number of electrons are excited to conduction band. This property improves the energy resolution of the

detector as a consequence of reduction of the statistical fluctuations. The typical HPGe detectors used in Gammasphere have an energy resolution of $\sim$ 2 MeV and peak-to-total ratio of 20%, for 1.332 MeV photo-peak energy of the standard radioactive ^{60}Co source. Figure 4.5 shows the typical spectrum relevant to this gamma-ray energy. The photons in the background are removed by using the suppression shields surrounding the detector. The HPGe detectors are continuously cooled with Liquid Nitrogen during operation to reduce electric noise by thermal excitations and the appearance of leakage current.

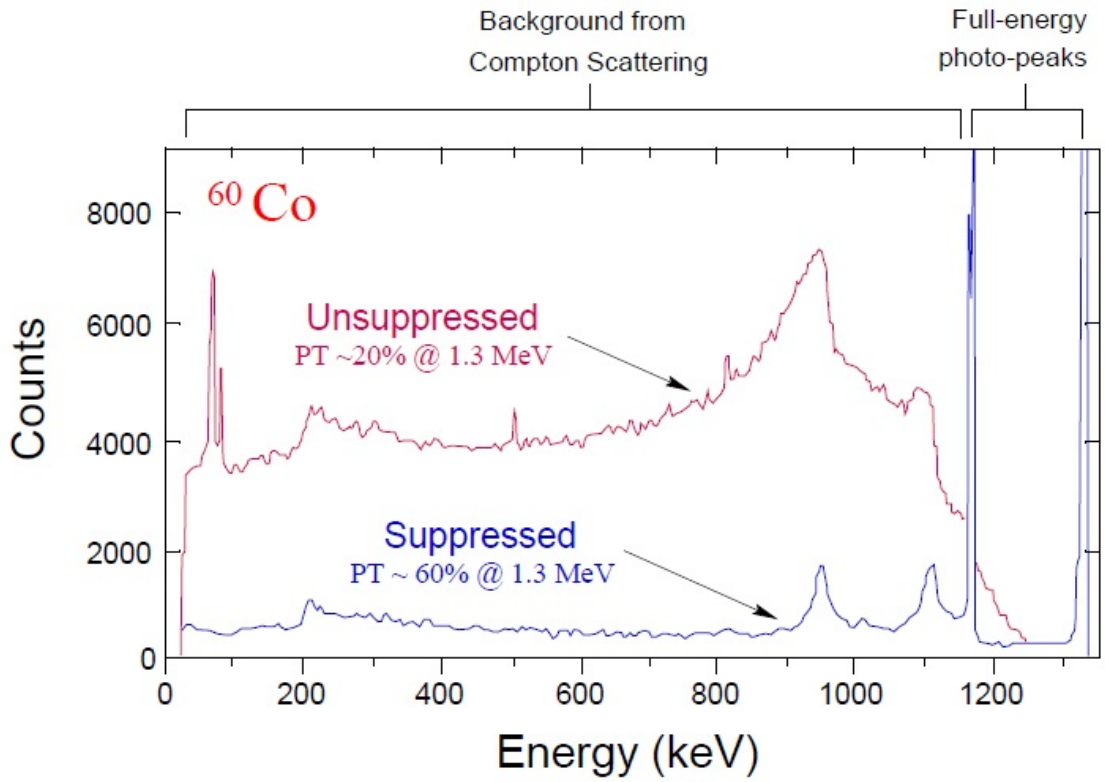

Figure 4.5: Gamma-ray spectra for 1.173 MeV and 1.332 MeV of ^{60}Co source obtained by using the HPGe detector used in the Gammasphere array, with Compton suppressed shield and without suppressed shield [Aki06]. The original figure is taken from Gammasphere booklet, http://nucalf.physics.fsu.edu/ riley/gamma/gamma3.html

4.4.3 Compton Suppressed Germanium Detector

The contribution of incomplete gamma-ray energy deposition in HPGe detectors appears as continuous background, which can be reduced by surrounding the HPGe detector with a high density scintillation detector, most commonly BGO is used for suppression shield purposes. A typical schematic diagram of a Compton suppressed HPGe detector used in Gammasphere is shown in Figure 4.6 [Eva04], in which, the gamma-rays scattered out interact with a BGO detector shield placed around the cylindrical HPGe detector and forward scattered gamma-rays interact with backplug BGO detector. The signals from the suppression shields are operated electronically in

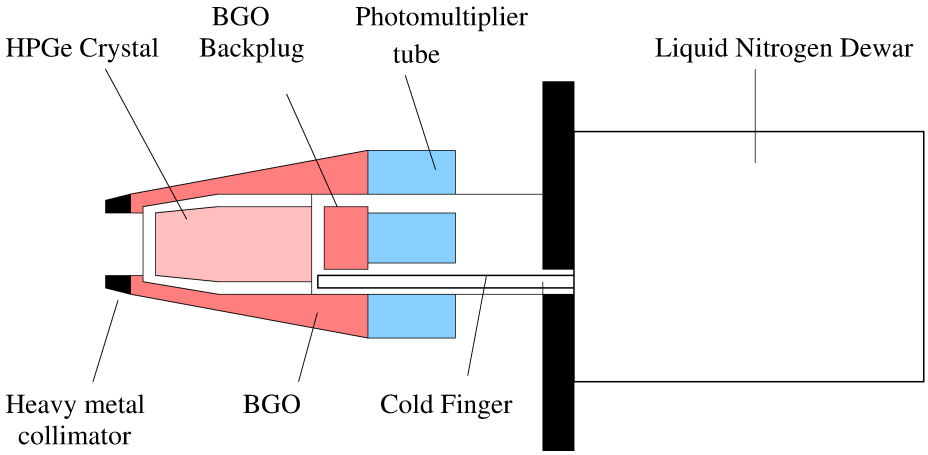

Figure 4.6: Schematic illustation of Compton-suppressed HPGe detecter used in the Gammasphere array. The figure is taken from [Eva04].

anticoincidence with HPGe signals. The front face of the BGO detector shield is collimated with 40 mm heavy metal to prevent the direct interaction of emitted gamma rays from the decaying nucleus with the BGO detector [Nol85, Nol94, Bax92, Car94]. Thus, the ratio of counts in the photopeak to the total number of the counts in the gamma ray spectrum rises. For instance in single suppressed HPGe used in the Gammasphere, the peak-to total ratio for emitted gamma-ray of 1.332 MeV from ^{60}Co source becomes about 60%, this improvement in peak- to- total ratio for ^{60}Co source is illustrated in Figure 4.5 [Aki06], shows the suppressed and unsuppressed spectra

produced with HPGe detector which has been used in Gammasphere.

The improvement in peak-to-total ratio (PT) is significant in high fold coincidence spectroscopy, for the photopeak coincidence probability which varies with $(PT)^n$, where n is number of fold event. As well as PT an important parameter in an array design to identify its sensitivity, which is measured by resolving power of the array and defined as [Bea96]:

$$R = \left(\frac{SE_\gamma}{\Delta E_\gamma}\right) PT \tag{4.7}$$

where SE_γ is the average energy between gamma-rays in the cascade of the studied nucleus and ΔE_γ is the full width of the gamma-rays at half maximum in the spectrum.

4.5 Gammasphere Array

The Gammasphere array [Lee90] (as shown in Figure 4.7) is one of the most powerful gamma-ray spectrometers used in the last two decades. It comprised of 110 HPGe n-type crystals each of size (7.2 cm $\times$ 8.4 cm) with BGO Compton Suppression shields in an electronic honeycomb design mounted in a 4π configuration around the target chamber. These are arranged into two symmetrical hemispherical shells, designed from a 122 element polyhedron comprised of 110 hexagonal faces for holding the Compton suppressed HPGe detectors and 12 pentagonal faces (one is used for beam access). The Compton suppressed HPGe detectors form 17 rings at different forward and backward angels relative to the beam direction. For analysis purposes this is reduced to nine rings. Table 4.1 lists the angles of HPGe detector rings in the Gammasphere array, relative to the beam direction. In the full implementation of 110 detectors, each HPGe detector subtends 0.418% of the total solid angle providing a total coverage of 46% for the array. The target is 24.8cm from the front of the HPGe detectors. The detectors that are mounted at 50.1°, 58.3°, 69.8°, 79.2° and 80.7° forward and backward angles around 90° have each been segmented into two D shapes electrically to reduce the Doppler broadening and increasing the resolving

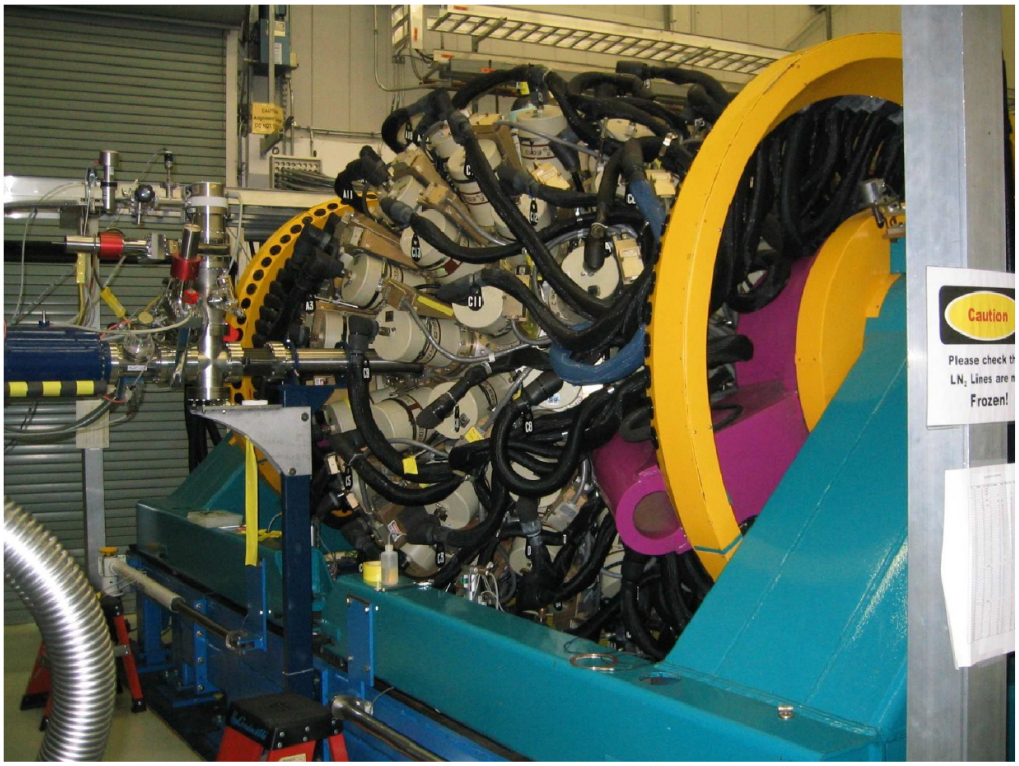

Figure 4.7: The Gammasphere array at Argonne National Laboratory. The figure is taken from [Tea09].

power of the array. The full Gammasphere array, for 1.332 MeV gamma-ray has a total photopeak efficiency of 9.4% and a resolving power of 9.4 (60% PT, 2 keV FWHM).

4.6 The Experimental Details

Excited states of ^{159}Er were populated by using the ATLAS accelerator at Argonne National Laboratory in United States of America to provide the reaction beam (^{48}Ca) with an energy of 215 MeV, bombarding the reaction target which comprised of two stacked thin self-supporting ^{116}Cd foils with a total thickness 1.3 mg/cm^2. The emitted gamma rays resulting from the reaction were detected by using the Gammasphere array spectrometer, A total of $\sim 1.9 \times 10^9$ high-fold coincidence gamma-ray events

Ring Number	Angle (Degrees)	New Ring Number	Number of Detectors
1	17.3°	1	5
2	31.7°	2	5
3	37.4°	2	5
4	50.1°	3	10
5	58.3°	3	5
6	69.8°	4	10
7	79.2°	5	5
8	80.7°	5	5
9	90.0°	5	10
10	99.3°	5	5
11	100.8°	5	5
12	110.2°	6	10
13	121.7°	7	5
14	129.9°	7	10
15	142.6°	8	5
16	148.3°	8	5
17	162.7°	9	5

Table 4.1: The numbers of HPGe detecctor in the rings of the Gammasphere array residing at different angles relative to the beam direction.

were collected under trigger conditions, at least seven of the 101 Compton suppressed HPGe detectors fired in prompt coincidence (γ^n, n$\geq$7). The data were collected during five days, and the events were unfolded off-line into 3.5 $\times$ 10^{10} quadruple and 1.4 $\times$ 10^{11} triple coincidence events. In the present work, the quadruple events were replayed off-line into RADWARE- format four dimensional(E^4_γ) hypercubes for analysis [Rad95], to investigate the 5n reaction channel ^{116}Cd(^{48}Ca, 5n) ^{159}Er. The data were used to construct the level scheme of the nucleus ^{159}Er.

4.7 Data Analysis

Gammasphere allows more than one gamma ray to be detected simultaneously. The detected gamma rays are collected in the form of high fold coincidence events. The acquired data is unfolded off-line into lower fold events (quadruple, triple, and double). For example, an event of four gamma-rays is unfolded into four triple-fold events or six double-fold events. The unfolded quadruple coincidence events have been used for the work of this thesis, in which, each coincidence quadruple event is arranged in a group of four gamma-rays(γ_1, γ_2, γ_3, γ_4) and sorted in four dimensional matrices (hypercube) as a single count at the axes (E_{γ_1}, E_{γ_2}, E_{γ_3}, E_{γ_4}) symmetrically by using the RADWARE programme [Rad95]. The programme has also been used to analyse hypercube coincidence events.

4.7.1 Hypercube Analysis

In four (three) and (two) dimensional symmetric matrix analysis, the spectra of coincidence gamma-ray cascade belonging to product nucleus could be produced for each possible reaction channel, and displayed by the 4DG8R (LEVIT8R) and (ESCL8R) programmes. To perform the analysis, gates were set on the specified gamma-rays, in the case of 4-Dimensional, (3-D) and (2-D) coincidence events, triple, (double), (single) gates set on the three, (two), (one) axes of the hypercube (cube), (matrix) axes, and all coincidence gamma-ray transitions simultaneously can be projected out onto the fourth (third), (second) axis. The resultant projected spectrum obtained from such gating conditions will be presented in the form of a one dimensional spectrum as a triple, (double), (single) gated spectrum, which is background subtracted [Cro95] using a new form of background subtraction incorporated into the RADWARE format and implemented by K. Lagergren [Lag04]. The hypercube coincidence analysis has been used for energy and intensity measurement of the detected gamma-ray for ^{159}Er, to construct the level scheme and to study of the structure of the nucleus.

4.7.2 Angular Intensity Ratio Measurment

In nuclear reactions, the spins of the populated nuclear excited states of the product nucleus have been oriented in the plane perpendicular to the direction of the beam axis. Classically, the multipole character of the emitted gamma-rays from decay between the populated nuclear excited states can be obtained by performing an analysis of the Directional Correlation of Oriented states [Ste73], which known as DCO measurement.

The multipolarity of transitions from these oriented states can be determined experimentally from the angular intensity ratio of the emitted gamma-rays, which is based on the DCO analysis and described [Pau95], [Tor97]. In this work, the MTSORT (MIDAS) software has been used to sort unfolded data into γ-γ matrices, by setting lists of gates on coincidence transitions that produce one dimensional spectra for the coincidence transitions at different detector ring angles of the Gammasphere relative to the beam direction. The angular intensity ratio of a specific gamma-ray has been identified from the intensity measurements (Iγ), which were detected by detectors positioned at ring two (34.55°) and ring nine (145.45°) angles, and at ring five (90.0°), perpendicular to the beam axis. Thus, the angular intensity ratio can be defined as:

$$R = \frac{I_{\gamma},(35^{\circ}/145^{\circ})}{I_{\gamma},(90^{\circ})} \tag{4.8}$$

The multipolarity of the electromagnetic transitions are assigned from the angular intensity ratio values. Typically, the extracted value from this analysis for stretched quadrupole (E2) transitions (ΔI = 2) and pure non-stretched dipole transitions (ΔI = 0) is approximately a factor two larger than for pure stretched dipole (M1 and E1) transitions (ΔI = 1) or for those are of the mixed M1/E2 character. This technique can allow one to assign the spin and parity of nuclear levels.

4.8 Gamma Decay

The nucleus could be in an excited state under the influence of an electromagnetic field. As a consequence of the interaction of nucleons (protons and neutrons) with the external field, the nucleus undergoes decay (de-excitation) to a low-lying excited state and then to the ground state. When the nucleus de-excites between its excited states, the predominant decay mode is the emission of electromagnetic photons in the energy domain of 0.1-10 MeV, in the form of gamma-rays. The angular momentum carried away by gamma-ray in each subsequent nuclear decay identifies the multipole order of the emitted gamma-ray, which provides the information on initial and final nuclear excited states in terms of energy, angular momentum (spin) and parity, leading to an understanding of the structure of the nucleus. The character of the electromagnetic radiation of the emitted gamma-rays is constrained by conservation of angular momentum and parity between initial and final excited states:

$$|I_i - I_f| \leq L \leq I_i + I_f \tag{4.9}$$

The multipole order of the emitted radiation (L) is determined by the possible value of quantized angular momentum (2^L), so the emission of a gamma-ray is not allowed for L = 0. The electromagnetic nature of multipole orders of the emitted radiation (gamma-rays) is identified from the change of parity between the initial and final states as follow:

For electric transitions

$$\pi_{EL} = (-1)^L \tag{4.10}$$

and for magnetic transitions

$$\pi_{ML} = (-1)^{L+1} \tag{4.11}$$

This means that, the transitions between states of the same parity are of the even multipole order electric transitions and of the odd multipole order magnetic transitions (M1, E2, M3, E4,..), on the other hand transitions between the states of different parity are of the odd multipole order electric transitions and of the even multiple order magnetic transitions (E1, M2, E3, M4,...).

Chapter 5

^{159}Er Results

5.1 Introduction

The rare-earth Erbium nuclei have been at the forefront of high-spin nuclear structure research. In this work, the gamma-ray transitions from excited states of ^{159}Er have been investigated up to terminating states using the Gammasphere spectrometer. Excited states in ^{159}Er were populated using the heavy-ion fusion-evaporation reaction of ^{116}Cd(^{48}Ca, 5nγ) at a beam energy of 215 MeV. Newly observed gamma-rays have been positioned in three new bands and, in addition, previously reported bands have been extended and amended. These include high-spin bands and high-K quasiparticle structures [Del87, Sim98]. To confirm the multipolarity of the previously observed transitions and identify the multipolarity of new transitions, angular intensity-ratio measurements have been performed.

5.2 Motivation

The development of gamma-ray spectrometer arrays, such as Eurogam and Gammasphere, have increased the opportunity to investigate how nuclear angular momentum is generated up to ultrahigh-spin. The transitional rare-earth nuclei ($A = 150 - 160$) have been at the forefront in revealing a variety of nuclear structure phenomena

through the generation of nuclear angular momentum [Gro73]. The angular momentum in atomic nuclei can be generated from collective motion of the core and from single particle contributions. The deformed prolate ($\beta_2 \geq 0.2$) heavy rare-earth nuclei ($N \approx 90$) exhibit the behaviour of a quantum rotor, through the collective rotational motion along the axis perpendicular to the symmetry axis, leading to the formation of rotational bands whose excited states follow the $E(I) \propto I(I+1)$ relation. The prolate nucleus loses its collective behaviour with increasing angular momentum as a result of Coriolis induced alignments, which break pairs of neutrons and protons, causing their spin vectors to align along the axis of rotation. As more and more valence nucleons align the contribution of single particle spins dominate in the generation of nuclear angular momentum. Eventually, the prolate nucleus undergoes a dramatic transition from collective behaviour to oblate noncollective single particle behaviour. The regular rotational bands terminate [Ben83, Tjø85, Ste85, Sim94] and the angular momentum of the excited states is generated entirely by the alignment of specific valence nucleons in equatorial orbits outside the spherical core of the $^{146}_{64}Gd_{82}$ nucleus.

5.3 ^{159}Er Results

The level scheme constructed for $^{159}_{68}Er_{91}$ in the present work will be presented in two sections; high spin structures and strongly coupled high-K bands. The transitions in each specific band were obtained from data collected using the Gammasphere spectrometer, which have been sorted into unfolded four-dimensional hypercubes using the RADWARE graphical analysis package 4DG8R developed by D. C. Radford [Rad00], as discussed in chaper 4. Analysis of the hypercubes involves applying a triple gate or sum of triple gates to a hypercube, and allows coincidence relationships between transitions to be deduced, and relative intensities of the transitions to be measured. Based on the coincidences and intensities observed, the gamma-ray transitions are ordered in the level scheme in distinct bands. While some of the transitions observed

in this work represent significant extensions to previously observed bands, three new bands have been observed in the level scheme, as shown in Figure 5.1 and 5.2 for the high-spin positive and negative parity structures respectively, and in Figure 5.16 for the strongly coupled high-K bands. Many previously observed transitions [Del87, Sim98] have been verified, however some of the gamma-ray transitions in the branches parallel to the yrast band and in one of the strongly coupled bands have been positioned differently in the level scheme in the present work, with small differences in transition energy of about 1-2 keV. The transition energies have been measured in keV, and the intensity measurements have been performed for the observed transitions using RADWARE to deduce the relative intensity of the gamma-ray transitions (I_γ), which were normalized relative to the intensity of the 208 keV $17/2^+ \rightarrow 13/2^+$ yrast transition with a value of 100. The gamma-ray energies are esimated to be accurate to ± 0.3 keV for the strong transitions ($I_\gamma > 10$), rising to ± 0.6 keV for weaker transitions.

5.4 High Spin Structure

The level scheme of the high-spin structure of ^{159}Er determined in the present work are presented in Figures 5.1 and 5.2. High-spin bands observed previously are labelled as yrast, Band 1, Band 2, Band 3, Band 4 and TSD1, and the newly observed bands are labelled as Band 5, Gamma-Band and Band 10. Multipolarities have been assigned for the new transitions and verified for the previously observed transitions by measuring angular intensity-ratios, as discussed in section 4.7.2. The angular intensity-ratios for the previously observed bands and for the three new bands are displayed in Figures 5.3 and 5.4 respectively.

5.4.1 Yrast Band (+, +1/2)

In the positive parity yrast band of ^{159}Er transitions have been previously reported by Deleplanque *et al.,* [Del87] up to a tentative excited state of spin and parity ($93/2^+$)

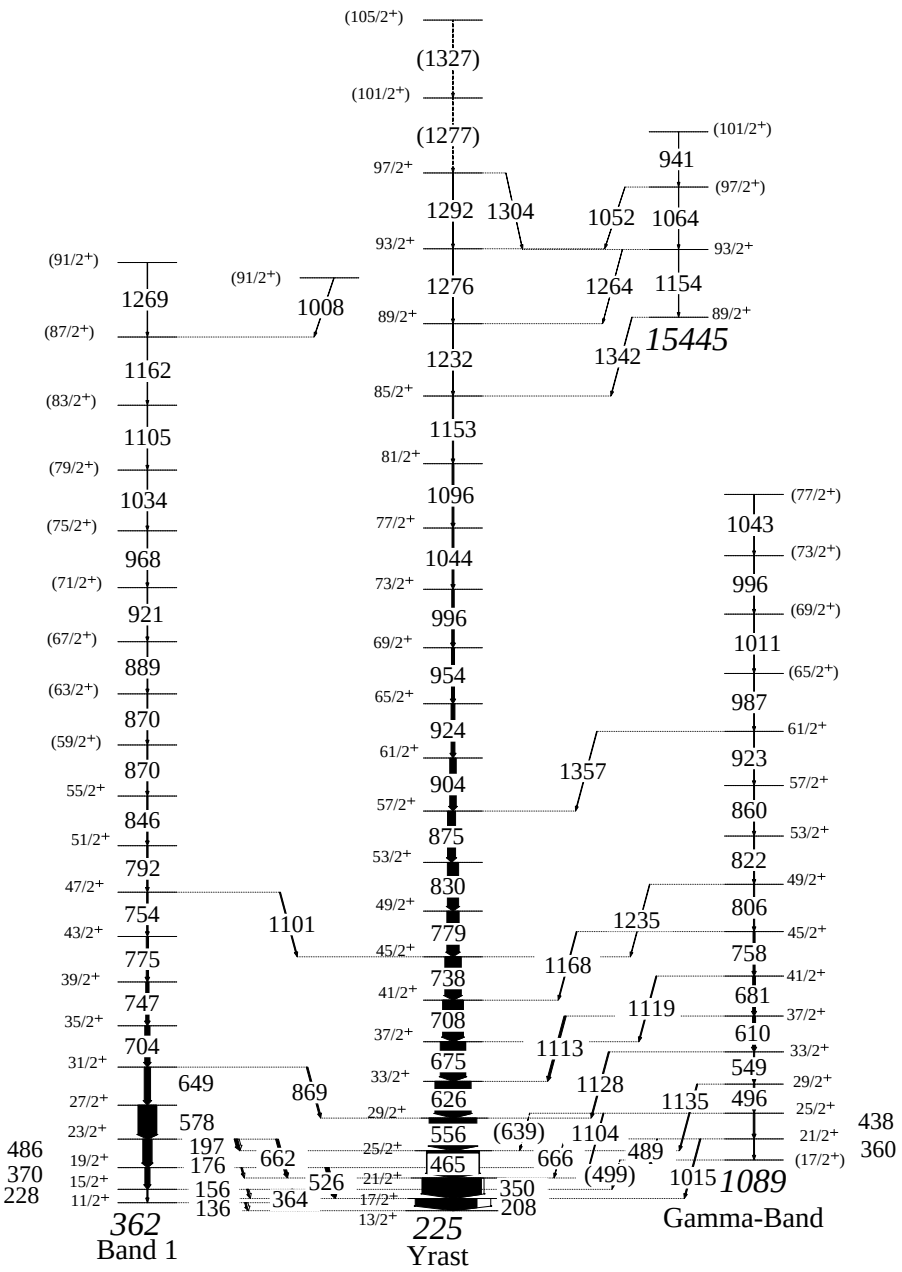

Figure 5.1: Partial level scheme for ^{159}Er constructed from the present work for positive parity high-spin band structures. The transition energies are given in keV, and the width of the arrows indicate the relative intensities of the transitions. Beneath each band in italics, the bandhead energy is given in keV. Spins and parities are based on measurements of angular intensity-ratios, and parenthesis indicate tentative spin and parity assigments. Where the observation of a transition is considered tentative, a dashed arrow and parenthesis are used.

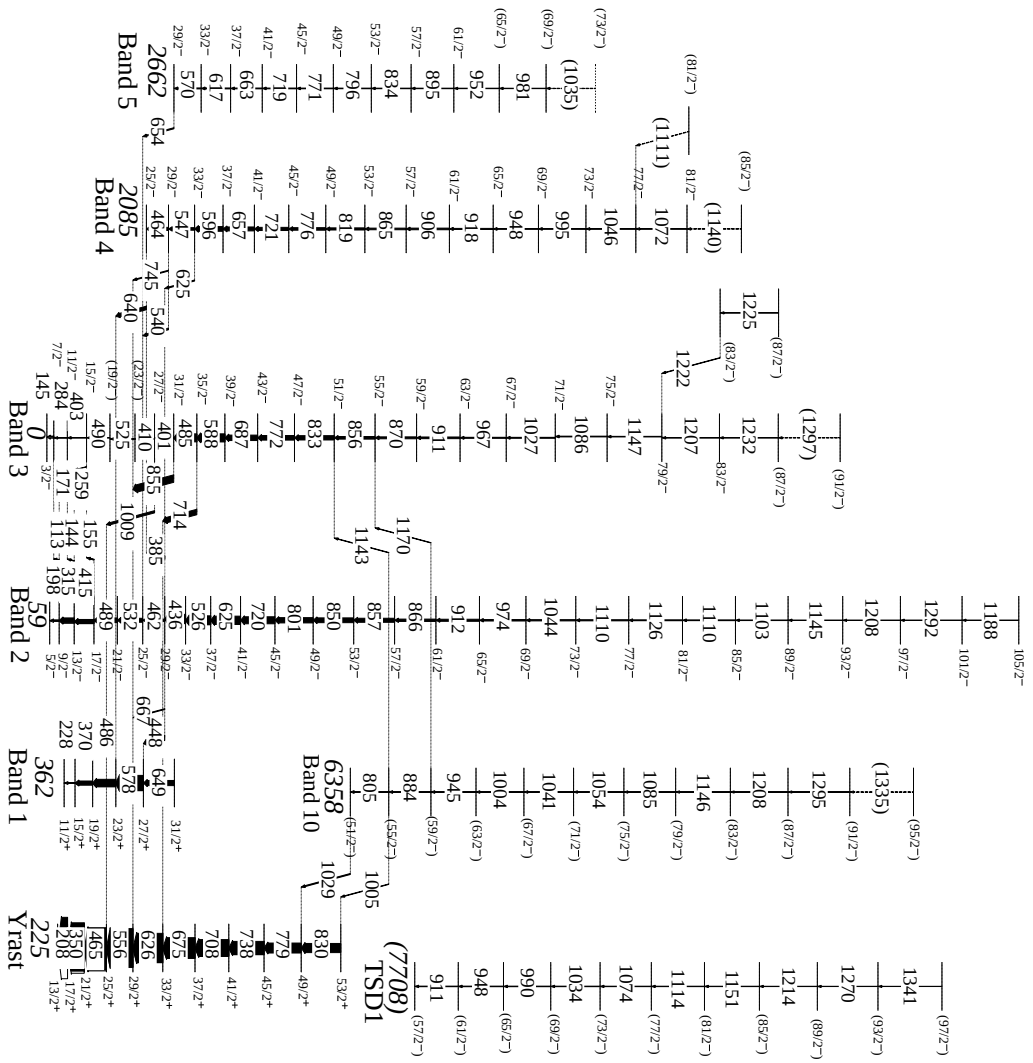

Figure 5.2: Partial level scheme for ^{159}Er constructed from the present work for negative parity high-spin band structures. The transition energies are given in keV, and the width of the arrows indicate the relative intensities of the transitions. Beneath each band in italics, the bandhead energy is given in keV. Spins and parities are based on measurements of angular intensity-ratios, and parenthesis indicate tentative spin and parity assigments. Where the observation of a transition is considered tentative, a dashed arrow and parenthesis are used.

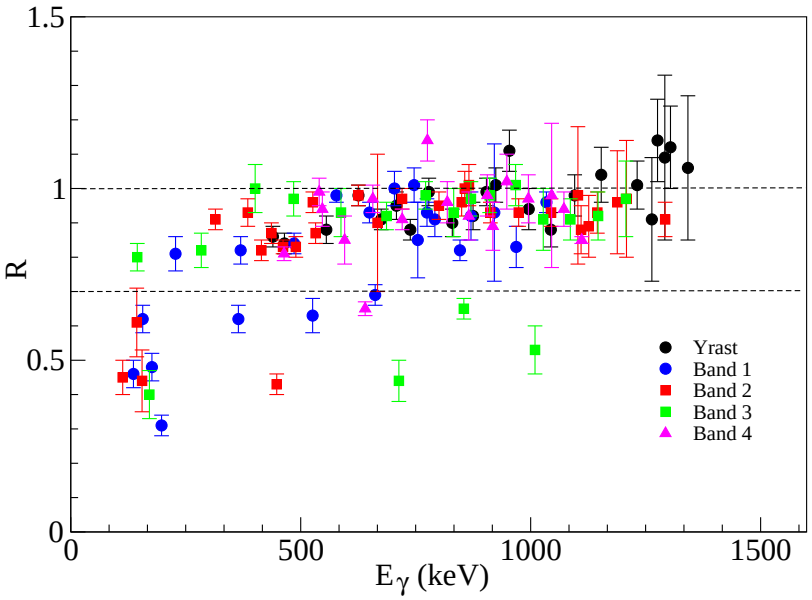

Figure 5.3: Angular intensity-ratios, R, for gamma-rays as a function of transition energy for the previously observed bands; Yrast, Band 1, Band 2, Band 3 and Band 4 in ^{159}Er.

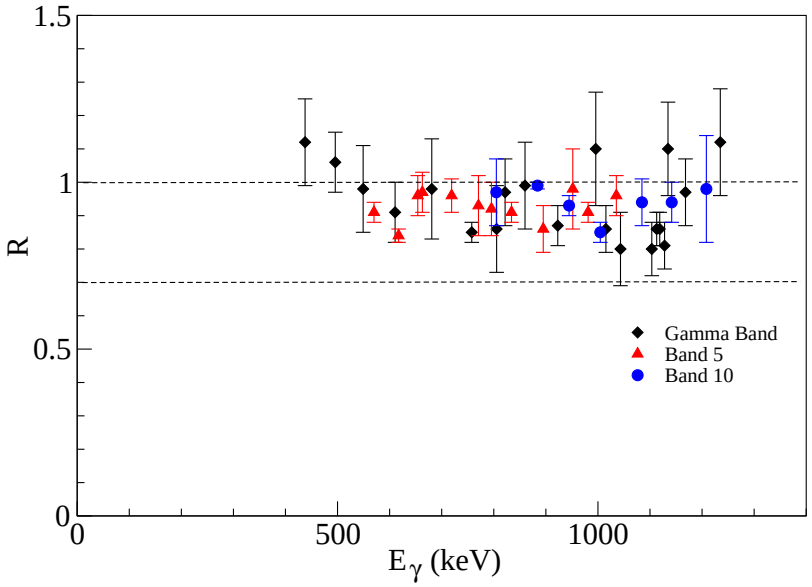

Figure 5.4: Angular intensity-ratios, R, for gamma-rays as a function of transition energy for new bands; Gamma-Band, Band 5 and Band 10 in ^{159}Er.

with a parallel sequence of two transitions 1152-keV and 1341-keV branching off from a tentative yrast ($85/2^+$) state. The yrast band and its parallel branch at high spin were extended up to states of spin/parity ($105/2^+$) and ($101/2^+$) respectively. The work of Kondev *et al.,* [Kon99] observed transitions at high-spin in the yrast band and its parallel branch, including a tentative transition of 941-keV gamma ray, when branched out from $81/2^+$ yrast state from the work of [Del87]. These transitions have been reordered and positioned in the yrast band and a parallel sequence branching out from the $85/2^+$ yrast state. The new linking transitions of 1052-keV, 1264-keV, 1304-keV and 1342-keV have been established between states in the parallel branch and yrast band, as shown in Figure (5.1). The spectra of high-energy gamma-ray transitions in the yrast band are presented in Figure 5.5, and the gamma-rays depopulated from the $33/2^+$ yrast state up to the terminating states of ($101/2^+$) and ($105/2^+$) are presented in Figure 5.5(a).

The photopeaks in the yrast band and its parallel branch above the state $81/2^+$ can be observed individually in coincidence at this high-energy region in Figures 5.5 (b) and (c) respectively. Spectrum (b) was produced with a sum of triple gates set on yrast transitions from the 830-keV to the 1153/1154-keV transitions in coincidence with the 1342-keV linking transition of the parallel sequence, and spectrum (c) was produced with a sum of triple gates set on yrast transitions from 830-keV to 1232-keV (excluding the 1153/1154-keV transitions) in coincidence the 1276-keV transition.

The intensity of the upper line transitions in Figure 5.5 indicate that the 1153-keV and 1154-keV transition are not resolved, and confirm that the gamma-ray transition of 941 keV depopulates the fully aligned terminating state $101/2^+$. A spectrum for all observed photopeaks in the yrast band is presented in Figure 5.6, produced with a sum of triple gates set on the transitons positioned in the present level scheme up to the $81/2^+$ state (1096-keV) of the yrast band. Angular intensity-ratio measurements for the 1264-keV, 1304-keV and 1342-keV linking transitions were performed and their multipolarity found to be stretched quadrupole (E2) transitions, which establishes positive parity and positive signature (π, α) = (+,+1/2) for the levels in the parallel

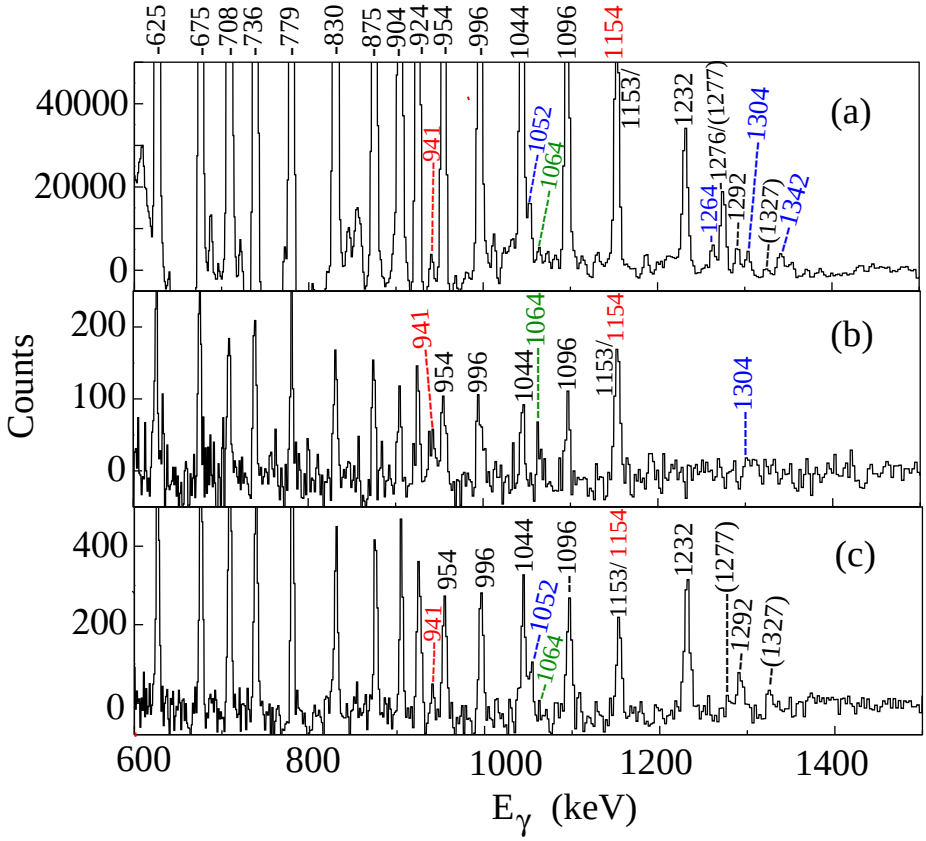

Figure 5.5: Coincidence spectra showing transitions from the decay of states in the yrast band of ^{159}Er, from the $33/2^+$ state up to the terminating $101/2^+$ and $105/2^+$ states. Linking transitions above the $85/2^+$ state are marked blue, and transitions in the parallel sequence are marked red. The coincidence spectrum (b) verifies that the initial state of the 941-keV transition is depopulated from the fully aligned terminating $101/2^+$ state. Spectra (a) and (c) provide the evidence for re-ordering the transitions in the yrast band shown in the level scheme of Figure (5.1). The spectra were produced from varoius sum of triple gates set on yrast transitions; (a) from 208-keV to 1096-keV, and (b) from 830-keV to the 1153/1154-keV transitions in coincidence with the 1342-keV, and (c) from 830-keV to the 1232-keV except the 1153/1154-keV transitions in coincidence with the 1276-keV transition.

branch to the yrast band. The gamma-ray energies measured as part of this work and their assignments in the yrast band are given in Table 5.1.

Band	$E_{ex.}$ (keV)	E_γ (keV)	I_γ	R	Multipol.	Transition
Yrast	433.3	208.0	100(3)		E2*	$17/2^+ \rightarrow 13/2^+$
	782.8	349.5	94.7(2.9)	0.86(0.03)	E2	$21/2^+ \rightarrow 17/2^+$
	1247.4	464.6	84.3(2.6)	0.84(0.03)	E2	$25/2^+ \rightarrow 21/2^+$
	1803.0	555.7	76.4(2.4)	0.88(0.04)	E2	$29/2^+ \rightarrow 25/2^+$
	2428.7	625.6	57.9(1.8)	0.98(0.03)	E2	$33/2^+ \rightarrow 29/2^+$
	3103.7	675.0	41.0(1.3)	0.91(0.03)	E2	$37/2^+ \rightarrow 33/2^+$
	3811.9	708.2	33.4(1)	0.95(0.04)	E2	$41/2^+ \rightarrow 37/2^+$
	4550.2	738.3	26.2(0.9)	0.88(0.03)	E2	$45/2^+ \rightarrow 41/2^+$
	5328.8	778.6	19.7(0.7)	0.99(0.04)	E2	$49/2^+ \rightarrow 45/2^+$
	6158.5	829.6	18.1(0.7)	0.90(0.04)	E2	$53/2^+ \rightarrow 49/2^+$
	7033.2	874.7	13.1(0.5)	0.92(0.04)	E2	$57/2^+ \rightarrow 53/2^+$
	7937.1	903.9	10.5(0.4)	0.99(0.04)	E2	$61/2^+ \rightarrow 57/2^+$
	8861.3	924.2	6.2(0.4)	1.01(0.05)	E2	$65/2^+ \rightarrow 61/2^+$
	9815.0	953.7	4.9(0.3)	1.11(0.06)	E2	$69/2^+ \rightarrow 65/2^+$
	10810.8	995.9	4(0.3)	0.94(0.06)	E2	$73/2^+ \rightarrow 69/2^+$
	11854.7	1043.9	3.1(0.3)	0.88(0.05)	E2	$77/2^+ \rightarrow 73/2^+$
	12950.4	1095.7	3(0.3)	0.98(0.06)	E2	$81/2^+ \rightarrow 77/2^+$
	14103.2	1152.8	2(0.3)	1.04(0.08)	E2	$85/2^+ \rightarrow 81/2^+$
	15335.4	1232.1	1.4(0.4)	1.01(0.07)	E2	$89/2^+ \rightarrow 85/2^+$
	15445.0	1342.1	0.86(0.2)	1.06(0.21)	E2	$89/2^+ \rightarrow 85/2^+$
	16598.8	1153.9	0.59(0.2)	1.04(0.08)	E2	$93/2^+ \rightarrow 89/2^+$
		1263.6	0.41(0.2)	0.91(0.18)	E2	$93/2^+ \rightarrow 89/2^+$
	16611.2	1275.9	0.95(0.2)	1.14(0.12)	E2	$93/2^+ \rightarrow 89/2^+$
	17662.9	1064.0	0.52(0.2)			$(97/2^+) \rightarrow 93/2^+$
		1052.5	0.48(0.2)			$(97/2^+) \rightarrow 93/2^+$
	17902.9	1291.7	0.84(0.2)	1.09(0.24)	E2	$(97/2^+) \rightarrow 93/2^+$
		1304.0	0.54(0.2)	1.12(0.12)	E2	$97/2^+ \rightarrow 93/2^+$
	18603.9	941.0	0.40(0.2)			$(101/2^+) \rightarrow (97/2^+)$
	(19179.9)	(1277.0)				$(101/2^+) \rightarrow 97/2^+$
	(20506.9)	(1327.0)				$(105/2^+) \rightarrow (101/2^+)$

Table 5.1: The measured properties of the γ-ray transitions in yrast band of ^{159}Er. * The multipolarity of 208 keV assigned according to [Gro73].

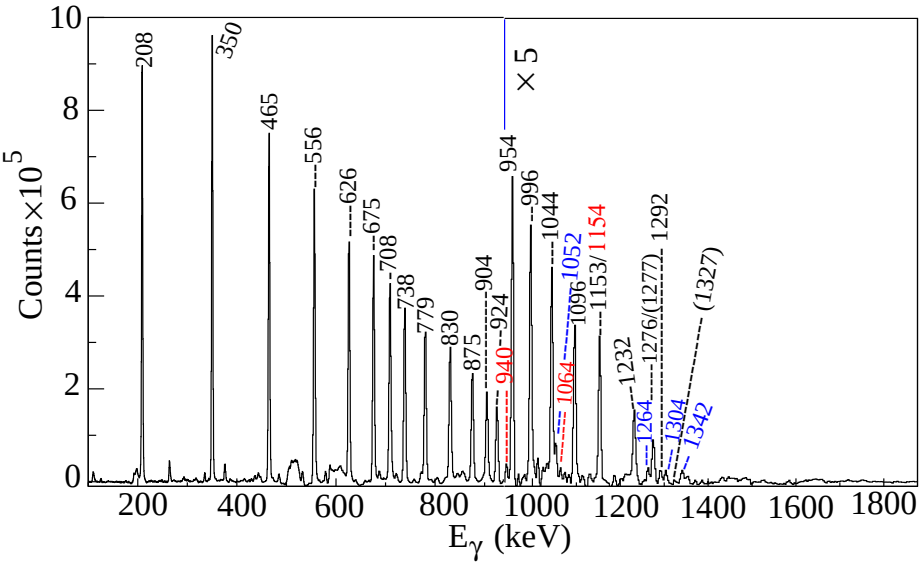

Figure 5.6: Coincidence spectrum produced from a sum of triple gates set on transitions from 208-keV to 1096-keV in the yrast band of ^{159}Er.

5.4.2 Band 1 (+, −1/2)

Band 1 (+,−1/2) is the unfavoured signature partner of the yrast band, the transitions in which were previously established up to a $43/2^+$ state by Simpson *et al.*, [Sim87]. The observation of thirteen new transitions in the present study has meant this band has been extended up to a possible excited state of spin and parity $(91/2^+)$. The intensity measurements for the spectra produced from the sum of triple gates on in-band transitions up to $(83/2^+)$ in this band, as shown in Figure 5.7(b), confirm that a 870-keV transition is a doublet and can be seen in coincidence with itself. The identification of the new transitions has been established from the sum of three double-gates on the four transitions, 846-keV, 870-keV, 870-keV, and 889-keV from the $51/2^+$ to $(67/2^+)$ state, as shown in Figure 5.7(a). The existence of both the 1008-keV and the 1269-keV transitions of the highest spin in this band, has been demonstated in the spectrum. The angular intensity-ratio measurements for the 136-keV, 156-keV, 176-keV, 197-keV, 364-keV and 526-keV linking transitions to the yrast

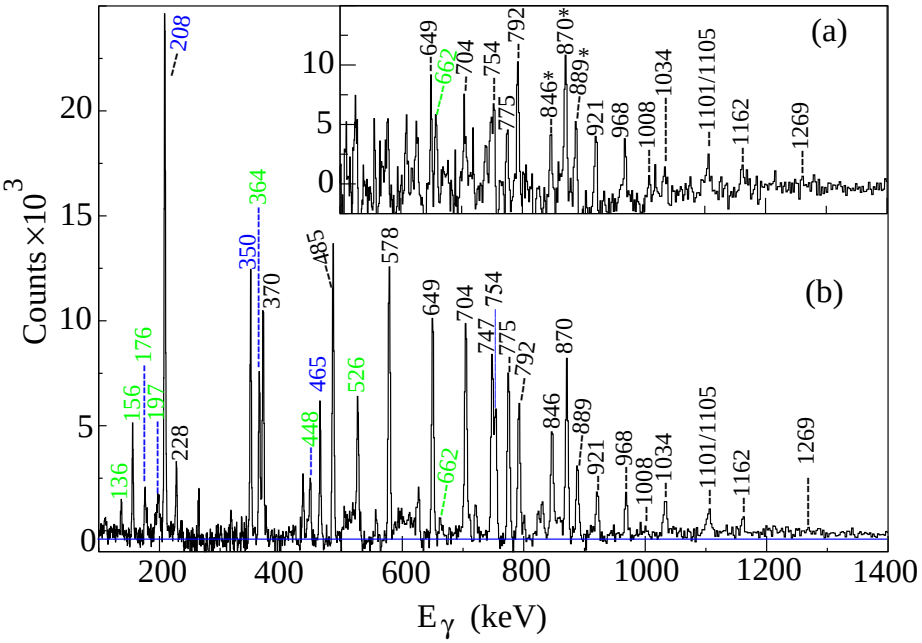

Figure 5.7: Coincidence spectra showing transitions from the decay of states in the Band 1 of ^{159}Er. (a) is proudced with a sum of double gates set on transitions from the decay of the $55/2^+$ state to $(67/2^+)$ state in Band 1, marked with asterisks, and clearly shows the 1008-keV transition which has initial state $91/2^+$. Coincidence spectrum in (b) is produced with a sum of triple gates set on in-band transitions from the 228-keV to 1105 keV in Band 1, which shows all transitions coincidence with Band 1. The linking transitions are marked in green, and clearly shows transition of 1008-keV depopulated from state $91/2^+$.

band confirm the previous assignments reported by Simpson *et al.,* [Sim87]. The presence of the 870-keV doublet transition means the multipolarity of the 870-keV transitions are tentative, thus the spin and parity assinments for states above the $55/2^+$ state are also tentative. In addition, the angular intensity-ratio measurement could not be performed for the 889-keV transition, but the angular intensity-ratios for the rest of the in-band transitions up to the $(79/2^+)$ state are consistent with that of stretched electric quadruple (E2) transitions. Band 1 depopulates to the $29/2^+$ and $45/2^+$ yrast states through two newly observed transitions of 869-keV and 1101-keV.

Furthermore the low spin excited states of $27/2^+$ and $23/2^+$ in this band have been mainly populated via transitions of 448-keV and 640-keV respectively, shown in Figure 5.2, which were observed previously by Deleplanque *et al.,* [Del87]. The transition of 448-keV decays from the $29/2^-$ state of Band 2, the ground state band, and the transition of 640-keV decays from the band-head of Band 4 at an excitation energy of 2085 keV. The angular intensity-ratio measurements for these two gamma-rays confirm the previous electric dipole (E1) multipolarity assignments, and the spin and parity assignment for the band-head of Band 4. Table 5.2 shows the gamma-ray energies, relative intensities, angular intensity-ratios, and the multipolarity assignments of the gamma ray transitions in Band 1 for ^{159}Er.

5.4.3 Band 2 (−, +1/2)

Band 2, the favoured spin-parity signature (α, $\pi = -$, $+1/2$) band, and it is the ground state band of ^{159}Er. However the excitation energy of this band is 59-keV higher than the excitation energy of Band 3, its unfavoured signature partner ($-$, $-1/2$) structure. This band has previously been observed up to highest excited state of spin/parity $105/2^-$, without any published spectum or level scheme for gamma-ray transitions [Kon99]. However, Deleplanque *et al.,* had previously established the gamma-ray transitions in this band tentatively up to $(97/2^-)$ [Del87]. As part of this work, gamma-ray transitions in this band have been observed up to a spin of $105/2^-$ with the observation of two new 1292-keV and 1188-keV photopeaks. The in-band transition energies are determined with a difference by 1-2 keV from previous measurements ([Del87]) for some transition energies. The coincidence spectra showing the 1292-keV and 1188-keV photopeaks corresponding to the gamma-decay of the states above $49/2^-$ state are presented in Figure 5.8 (a and b). The spectra in Figure 5.8 (a and b) are produced with a sum of triple gates on in-band transitions from the decay of the $53/2^+$ state to $(93/2^+)$ state, in parallel with the 1208-keV and 1292-keV transitions respectively. Both spectra indicate the presence of 1188-keV with no clear candidate for the decay of a higher lying state. The spectrum in Figure 5.8 (c) is

Band	$E_{ex.}$ (keV)	E_γ (keV)	I_γ	R	Multipol.	Transition
1→yrast	361.5	136.3	2.4(0.3)	0.46(0.04)	M1/E2	$11/2^+ \rightarrow 13/2^+$
1	589.7	227.9	1.4(0.1)	0.81(0.05)	E2	$15/2^+ \rightarrow 11/2^+$
1→yrast		156.5	2.0(0.1)	0.62(0.04)	M1/E2	$15/2^+ \rightarrow 17/2^+$
		364.5	2.9(0.4)	0.62(0.04)	M1/E2	$15/2^+ \rightarrow 13/2^+$
1	959.3	369.5	7.8(0.4)	0.82(0.04)	E2	$19/2^+ \rightarrow 15/2^+$
1→yrast		176.5	1.5(0.1)	0.48(0.04)	M1/E2	$19/2^+ \rightarrow 21/2^+$
		526.0	6.2(0.4)	0.63(0.05)	M1/E2	$19/2^+ \rightarrow 17/2^+$
1	1444.8	485.6	14.6(0.6)	0.84(0.03)	E2	$23/2^+ \rightarrow 19/2^+$
1→yrast		197.4	5.5(0.2)	0.41(0.03)	M1/E2	$23/2^+ \rightarrow 25/2^+$
		662.0	4.4(0.4)	0.69(0.03)	M1/E2	$23/2^+ \rightarrow 21/2^+$
1	2022.4	577.6	30.1(1.3)	0.98(0.02)	E2	$27/2^+ \rightarrow 23/2^+$
	2671.6	649.4	10.1(0.5)	0.93(0.03)	E2	$31/2^+ \rightarrow 27/2^+$
1→yrast		868.6	2.5(0.4)			$31/2^+ \rightarrow 29/2^+$
1	3375.5	703.9	8.4(0.6)	1.00(0.05)	E2	$35/2^+ \rightarrow 31/2^+$
	4122.1	746.6	5.3(0.4)	1.01(0.05)	E2	$39/2^+ \rightarrow 35/2^+$
	4896.7	774.6	3.6(0.3)	0.93(0.04)	E2	$43/2^+ \rightarrow 39/2^+$
	5651.1	754.5	2.5(0.2)	0.85(0.11)	E2	$47/2^+ \rightarrow 43/2^+$
1→yrast		1101.5	1.8(0.3)			$47/2^+ \rightarrow 45/2^+$
1	6442.8	791.7	2.2(0.2)	0.91(0.05)	E2	$51/2^+ \rightarrow 47/2^+$
	7289.0	846.2	2.1(0.2)	0.82(0.03)	E2	$55/2^+ \rightarrow 51/2^+$
	8159.2	870.2	1.7(0.4)	0.92(0.07)	(E2)	$(59/2^+) \rightarrow 55/2^+$
	9029.3	870.2	1.4(0.4)	0.92(0.07)	(E2)	$(63/2^+) \rightarrow (59/2^+)$
	9918.0	888.7	1.3(0.2)			$(67/2^+) \rightarrow 63/2^+$
	10839.0	921.0	1.2(0.2)	0.93(0.2)	E2	$(71/2^+) \rightarrow (67/2^+)$
	11807.2	968.1	1.1(0.2)	0.83(0.06)	E2	$(75/2^+) \rightarrow (71/2^+)$
	12841.4	1034.2	1.0(0.2)	0.96(0.03)	E2	$(79/2^+) \rightarrow (75/2^+)$
	13946.2	1104.7	0.9(0.2)			$(83/2^+) \rightarrow (79/2^+)$
	15108.2	1162.1	0.83(0.1)			$(87/2^+) \rightarrow (83/2^+)$
	16116.2	1007.9	0.73(0.1)			$(91/2^+) \rightarrow (87/2^+)$
	163377	1268.8	0.78(0.1)			$(91/2^+) \rightarrow (87/2^+)$

Table 5.2: Illustrates the measured properties (Relative intensity, Angular-intensity ratios and multipolarity assignment) of the γ-ray transitions in Band 1 of ^{159}Er.

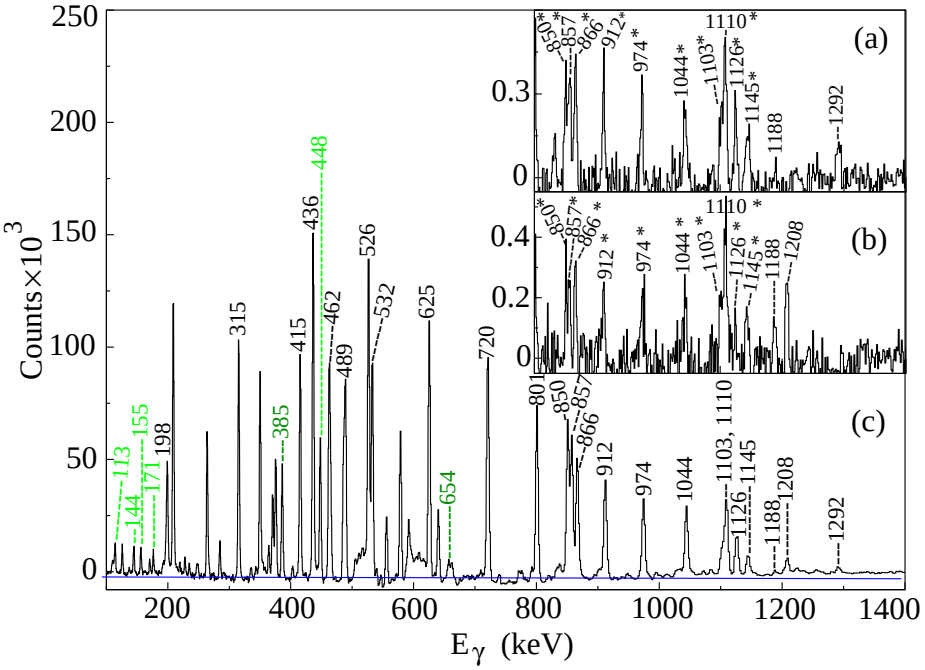

Figure 5.8: Coincidence spectra from the decay of states in Band 2 of ^{159}Er. (a) Transitions above the state $49/2^-$ in coincidence with 1292-keV, proudced with a sum of triple gates set on coincidence transitions from the decay of the $53/2^+$ state to $(93/2^+)$ state marked with asterisks and 1208-keV. (b) Transitions above the state $49/2^-$ in coincidence with the 1188-keV, produced with a sum of triple gates set on coincidence transitions from the decay of the $53/2^+$ state to $(93/2^+)$ state marked with asterisks and 1292-keV. (c) Produced with a sum of triple gets set on all in-band transitions up to the $(97/2^-)$ state in Band 2, which shows all transitions coincidence with Band 1. The linking transitions are marked in green.

presented to show transitions in coincidence with transitions in Band 2 up to $105/2^-$ state. The spectrum is produced with a sum of triple gates set on in-band transitions up to the $(97/2^-)$ state. The intensity measurements from doubly gated coincidence spectra show that the 1110-keV transition is doublet. The relative order of the 1110, 1110, 1103 and 1126 keV transitions has been established from the intensity measurments. Using spectra produced from double-gates on the 974 and 1044 keV. The multipolarity of the transitions in this band has been established by measuring

angular intensity-ratios. All of the in-band transition were found to be stretched electric quadrupole (E2) transitions. The multipolarity of linking transitions has been assigned the 113-keV, 144-keV and 155-keV transitions were of the mixed M1/E2 character. The 448-keV, 385-keV, and the newly observed 667-keV transition, which decay to Band 1, Band 4 and the yrast band, have the multipolarity of a stretched E1, E2 and E1 respectively. The transition energies, relative intensities and angular intensity-ratios of the gamma-rays in Band 2 for ^{159}Er are given in Table 5.3.

5.4.4 Band 3 (−, −1/2)

Band 3 is the unfavoured signature partner of the ground state band, and has previously been studied by Deleplanque *et al.,* [Del87] up to a tentative state of spin and parity $(83/2^-)$, as two discontinous sequences at low-spin and high-spin with a gap of $6\hbar$ between them. The low-spin structure was composed of three transitions, which were previously established by Simpson *et al.,* [Sim87] up to the excitation energy of 832 keV. The high-spin structure of this band started from the $27/2^-$ state at excitation energy 2257 keV up to the tentative $(87/2^-)$ state. This band is linked to the yrast band by the 1009-keV, 855-keV, and 714-kev transitions. In the present work three new transitions of energy 410-kev, 490-keV and 525-keV have been found to fill the discontinuity between the low-spin and high-spin structures. The spectrum in Figure 5.9(a) which illustrates the three new transitions, and is produced with a sum of triple gates set on the 145-keV, 284-keV and 403-keV transitions, and is in coincidence with of the 485-keV, 588-keV, and 687-keV transitions in this band. In addition, this band has been extended up to spin $(91/2^-)$ with a new transition of 1232-keV and another (tentative) transition of (1297)-keV. A spectrum of most of the transitions in this band is shown in Figure 5.9(b) produced with a sum of triple gates on in-band transitions from the decay of the $31/2^-$ state to $83/2^-$ state. A parallel sequence originating from the $79/2^-$ state has been found, with two newly observed transitions of 1222-keV and 1225-keV. The excitation energy of the two new states is higher than that of the $83/2^-$ and $87/2^-$ states in band 3. The spectra of the high

Band	$E_{ex.}$ (keV)	E_γ (keV)	I_γ	R	Multipol.	Transition
2	257.5	198.2	2.4(0.8)		E2*	$9/2^- \rightarrow 5/2^-$
2→3		112.9	1.1(0.01)	0.45(0.05)	M1/E2	$9/2^- \rightarrow 7/2^-$
2	572.1	314.6	10.0(0.4)	0.91(0.03)	E2	$13/2^- \rightarrow 9/2^-$
2→3		143.6	0.5(0.1)	0.61(0.10)	M1/E2	$13/2^- \rightarrow 11/2^-$
2	986.6	414.5	8.1(0.3)	0.82(0.03)	E2	$17/2^- \rightarrow 13/2^-$
2→3		155.1	0.96(0.1)	0.44(0.09)	M1/E2	$17/2^- \rightarrow 15/2^-$
2	1476.0	489.4	9.0(0.3)	0.83(0.03)	E2	$21/2^- \rightarrow 17/2^-$
	2008.4	532.4	7.8(0.5)	0.87(0.03)	E2	$25/2^- \rightarrow 21/2^-$
	2470.0	461.6	4.5(0.2)	0.83(0.02)	E2	$29/2^- \rightarrow 25/2^-$
2→4		385.0	6.3(0.3)	0.93(0.04)	E2	$29/2^- \rightarrow 25/2^-$
2→1		447.8	9.7(0.4)	0.43(0.03)	E1	$29/2^- \rightarrow 27/2^+$
2→yrast		667.0	1.5(0.3)	0.90(0.2)	E1	$29/2^- \rightarrow 29/2^+$
2	2906.3	436.3	18.1(0.6)	0.87(0.03)	E2	$33/2^- \rightarrow 29/2^-$
	3432.7	526.4	17.5(0.6)	0.96(0.03)	E2	$37/2^- \rightarrow 33/2^-$
	4058.2	625.5	16.3(0.6)	0.98(0.03)	E2	$41/2^- \rightarrow 37/2^-$
	4778.6	720.4	13.9(0.6)	0.97(0.03)	E2	$45/2^- \rightarrow 41/2^-$
	5579.2	800.6	10.5(0.4)	0.95(0.04)	E2	$49/2^- \rightarrow 45/2^-$
	6429.2	850.0	9.5(0.4)	0.96(0.04)	E2	$53/2^- \rightarrow 49/2^-$
	7285.9	856.7	8.0(0.4)	1.00(0.05)	E2	$57/2^- \rightarrow 53/2^-$
	8151.7	865.8	4.7(0.3)	1.01(0.06)	E2	$61/2^- \rightarrow 57/2^-$
	9064.0	912.3	4.1(0.3)	0.93(0.03)	E2	$65/2^- \rightarrow 61/2^-$
	10037.9	974.0	2.9(0.3)	0.93(0.04)	E2	$69/2^- \rightarrow 65/2^-$
	11082.2	1044.3	2.5(0.3)	0.93(0.04)	E2	$73/2^- \rightarrow 69/2^-$
	12191.8	1109.6	2.2(0.3)	0.88(0.07)	E2	$77/2^- \rightarrow 73/2^-$
	13318.0	1126.2	1.8(0.2)	0.89(0.09)	E2	$81/2^- \rightarrow 77/2^-$
	14427.8	1109.7	1.5(0.2)	0.88(0.07)	E2	$85/2^- \rightarrow 81/2^-$
	15530.5	1102.7	1.1(0.2)	0.98(0.20)	E2	$89/2^- \rightarrow 85/2^-$
	16675.4	1145.0	0.9(0.1)	0.93(0.06)	E2	$93/2^- \rightarrow 89/2^-$
	17883.8	1208.4	0.8(0.1)	0.97(0.17)	E2	$97/2^- \rightarrow 93/2^-$
	19176.2	1292.4	0.7(0.1)	0.91(0.05)	E2	$101/2^- \rightarrow 97/2^-$
	20364.6	1188.3	0.6(0.1)	0.97(0.17)	E2	$105/2^- \rightarrow 101/2^-$

Table 5.3: The measured properties of the transitions in Band 2 of ^{159}Er, *[Str75].

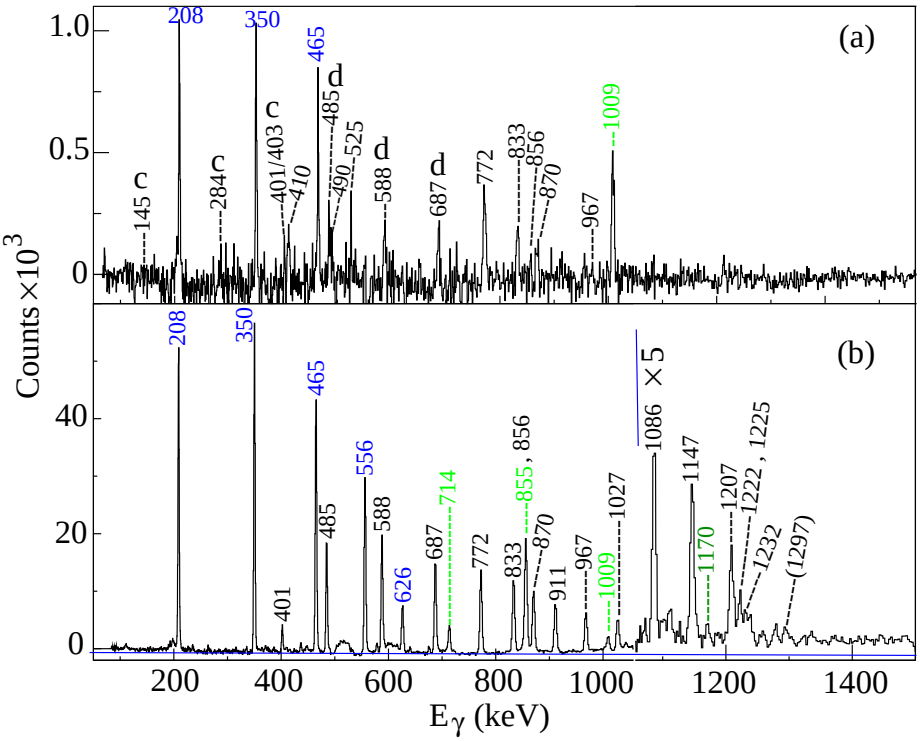

Figure 5.9: Coincidence spectra from the decay of states in the Band 3 of ^{159}Er. Spectrum in (a) shows the three new transitions of 403-keV, 410-keV and 490-keV in coincidence with the previously observed transitions, produced with a sum of triple gates set on transtions marked with c, 145-keV, 284-keV, 403-keV and 1009-keV in coincidence with the transitions marked with d, 485-keV, 588-keV and 687-keV. Spectrum in (b) displays the majority of transitions in Band 3 in coincidence with the most intense transitions of the yrast band. Produced with a sum of triple gates on in-band transitions from the decay of the $31/2^+$ state to $83/2^+$ state. In the specta, linking transitions are marked in green and transitions of the yrast band in blue.

energy transitions in this band are presented in Figure 5.10. The coincidence spectrum shown in (a) is produced with a sum of triple gates set on in-band transitions from the decay of the $43/2^-$ state to $79/2^-$ state in coincidence with the 1207-keV transition, and in (b) is produced with a sum of the same triple gates in coincidence with the 1222-keV transition. These spectra verify that the 1232-keV and 1297-keV transitions are in coincidence with 1207-keV. The transition of 1225-keV, in a parallel sequence,

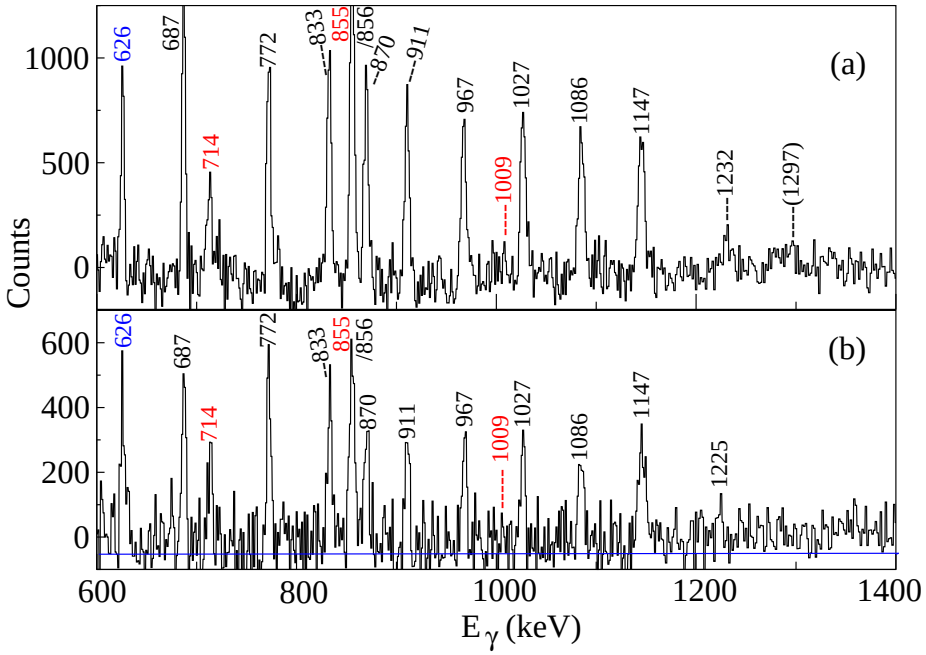

Figure 5.10: Spetra of coincidence transitions from the decay of states above $39/2^-$ in band 3. A Spectrum in (a) is produced from a sum of triple gates set on the coincidence transitions from the decay of the $39/2^-$ state to the $79/2^-$ state in coincidence with 1209-keV transition, and in (b) is produced from a sum of the same triple gate in coincidence with 1222-keV transition. In the specta, the transitions that are linking Band 3 to the yrast band marked in red, and a yrast transition of 625-keV is marked in in blue.

is in coincidence with the 1222-keV transition above the $79/2^-$ state. The spectra also show the dramatic reduction in the gamma-ray intensity above this state.
Angular intensity-ratio measurements have been performed to identify the multipolarity of transitions but, because of the low of statistics, in many cases this has not been possible. Otherwise the obtained values confirm previously reported transitions in this band [Sim87, Del87]. The measured properties of the transitions (Relative intensity, Angular-intensity ratios and multipolarity assignment) in Band 3 are given in Table 5.4.

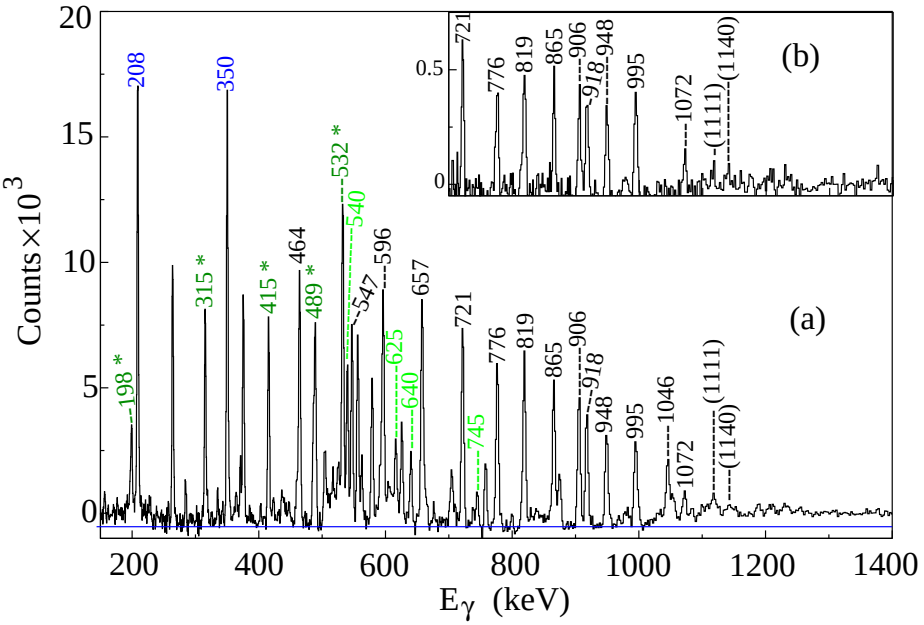

Figure 5.11: Coincidence spectra produced with a sum of triple gates set on in-band transitions in the Band 4 of ^{159}Er. (a) from the decay of the $29/2^-$ to the $77/2^-$ state, that shows all coincidence transitions in Band 4 with the five first transitions of the Band 2, ground state band, and the most intense two transitions in the bottom of the yrast band of ^{159}Er. The linking transitions are marked in green, the transitions of the Band 2 are marked with asterisks and yrast transitions in blue. (b) from the decay of the $29/2^-$ state to the $69/2^-$ state in coincidence with the 1046-keV transition. A spectrum shows coincidence transition from the decay of states above $41/2^-$.

5.4.5 Band 4 (−, +1/2)

This band has the same signature $(-1/2)$ as Band 2, the ground state band, and has been previously studied up to a tentative spin and parity of $(77/2^-)$ by Deleplanque *et al.,* [Del87]. In the current work this band has been extended by two new transitions up to state of $85/2^-$ with gamma-ray energies of 1072-keV and (1140)-keV tentatively, in addition a tentative gamma-ray of (1111)-keV, which populates the $77/2^-$ level. The spectrum in Figure 5.11(a) produced with a sum of triple gates set on in-band

Band	$E_{ex.}$ (keV)	E_γ (keV)	I_γ	R	Multipol.	Transition
3	144.6	144.6	2.4(0.2)	0.8(0.04)	E2	$7/2^- \rightarrow 3/2^-$
	428.4	283.8	0.87(0.1)	0.82(0.05)	E2	$11/2^- \rightarrow 7/2^-$
3→2		171.0	0.85(0.1)	0.4(0.07)	M1/E2	$11/2^- \rightarrow 9/2^-$
3	831.5	403.1	1.1(0.1)		E2*	$15/2^- \rightarrow 11/2^-$
3→2		259.5	0.7(0.1)			$15/2^- \rightarrow 13/2^-$
3	1321.7	490.1	1.0(0.1)			$(19/2^-) \rightarrow 15/2^-$
3	1846.3	524.7	0.9(0.1)			$(23/2^-) \rightarrow (19/2^-)$
3	2256.7	410.4	0.8(0.1)			$27/2^- \rightarrow (23/2^-)$
3→yrast		1009.4	4.3(0.4)	0.53(0.07)	E1	$27/2^- \rightarrow 25/2^+$
3	2657.8	401.0	2.2(0.2)	1.00(0.07)	E2	$31/2^- \rightarrow 27/2^-$
3→2		854.7	14.4(0.6)	0.65(0.03)	E1	$31/2^- \rightarrow 29/2^+$
3	3142.4	484.6	15.5(0.4)	0.97(0.05)	E2	$35/2^- \rightarrow 31/2^-$
3→2		713.5	8.5(0.4)	0.44(0.06)	E1	$35/2^- \rightarrow 33/2^+$
3	3729.7	587.6	15.7(0.6)	1.35(0.07)	E2	$39/2^- \rightarrow 35/2^-$
	4416.5	686.6	10.8(0.4)	0.92(0.04)	E2	$43/2^- \rightarrow 39/2^-$
	5188.1	771.6	9.1(0.4)	0.98(0.04)	E2	$47/2^- \rightarrow 43/2^-$
	6020.7	832.6	8.6(0.4)	0.93(0.07)	E2	$51/2^- \rightarrow 47/2^-$
	6876.6	855.9	5.1(0.3)		E2*	$55/2^- \rightarrow 51/2^-$
	7746.7	870.1	3.8(0.3)	0.97(0.05)	E2	$59/2^- \rightarrow 55/2^-$
	8657.6	910.9	3.3(0.3)	0.98(0.05)	E2	$63/2^- \rightarrow 59/2^-$
	9624.7	967.2	2.1(0.3)	1.01(0.06)	E2	$67/2^- \rightarrow 63/2^-$
	10652.1	1027.3	1.9(0.3)	0.91(0.09)	E2	$71/2^- \rightarrow 67/2^-$
	11738.6	1086.3	1.5(0.2)	0.91(0.06)	E2	$75/2^- \rightarrow 71/2^-$
	12885.2	1146.6	1.2(0.2)	0.92(0.07)	E2	$79/2^- \rightarrow 75/2^-$
	14092.6	1207.4	1.0(0.2)	0.97(0.11)	E2	$83/2^- \rightarrow 79/2^-$
	14106.8	1221.6	0.8(0.1)			$(83/2^-) \rightarrow 79/2^-$
	15324.7	1232.1	0.7(0.1)			$(87/2^-) \rightarrow 83/2^-$
	15331.8	1225.0	0.6(0.1)			$(87/2^-) \rightarrow (83/2^-)$
	16621.3	1296.6	0.6(0.1)			$(91/2^-) \rightarrow (87/2^-)$

Table 5.4: Illustrates the measured properties (Relative intensity, Angular-intensity ratios and multipolarity assignment) of the γ-ray transitions in Band 3 of ^{159}Er, * the multipolarity of 403 and 856 keV transitions assigned acoording to [Del87]

.

Band	$E_{ex.}$ (keV)	E_γ (keV)	I_γ	R	Multipol.	Transition
4→1	2085.0	640.2	6.8(0.3)	0.65(0.02)	E1	$25/2^- \rightarrow 23/2^+$
4	2548.5	463.8	1.5(0.1)	0.81(0.02)	E2	$29/2^- \rightarrow 25/2^-$
4→2		540.1	3.4(0.2)	0.99(0.04)	E2	$29/2^- \rightarrow 25/2^-$
4→yrast		745.4	1.7(0.1)		E1*	$29/2^- \rightarrow 29/2^+$
4	3095.4	547.0	5.1(0.3)	0.94(0.05)	E2	$33/2^- \rightarrow 29/2^-$
4→2		625.4	2.0(0.2)			$33/2^- \rightarrow 29/2^-$
4	3691.4	595.6	9.3(0.2)	0.85(0.07)	E2	$37/2^- \rightarrow 33/2^-$
	4347.9	656.8	7.8(0.5)	0.97(0.04)	E2	$41/2^- \rightarrow 37/2^-$
	5068.5	720.7	6.2(0.5)	0.91(0.03)	E2	$45/2^- \rightarrow 41/2^-$
	5844.0	775.5	5.0(0.3)	1.14(0.06)	E2	$49/2^- \rightarrow 45/2^-$
	6662.8	818.7	4.3(0.3)	0.96(0.06)	E2	$53/2^- \rightarrow 49/2^-$
	7528.2	865.5	3.4(0.3)	0.92(0.06)	E2	$57/2^- \rightarrow 53/2^-$
	8434.0	905.8	3.2(0.3)	0.98(0.06)	E2	$61/2^- \rightarrow 57/2^-$
	9351.6	917.7	2.1(0.3)	0.89(0.07)	E2	$65/2^- \rightarrow 61/2^-$
	10299.9	948.2	1.6(0.2)	1.02(0.08)	E2	$69/2^- \rightarrow 65/2^-$
	11294.9	995.0	1.5(0.2)	0.97(0.07)	E2	$73/2^- \rightarrow 69/2^-$
	12340.5	1045.6	1.2(0.2)	0.98(0.21)	E2	$77/2^- \rightarrow 73/2^-$
	13412.6	1072.3	0.9(0.2)	0.94(0.05)	E2	$81/2^- \rightarrow 77/2^-$
	13451.2	(1111.0)	0.7(0.1)			$(81/2^-) \rightarrow 77/2^-$
	14552.3	(1139.7)	0.85(0.1)			$(85/2^-) \rightarrow 81/2^-$

Table 5.5: Illustrates the measured properties (Relative intensity, Angular-intensity ratios and multipolarity assignment) of the γ-ray transitions in Band 4 of ^{159}Er, * the multipolarity of 745.4-keV transition assigned acoording to [Del87].

transitions from the decay of the $33/2^-$ state to the $77/2^-$ state, clearly shows all the transitions in Band 4, in coincidence with the five first transitions of the Band 2, ground state band. A spectrum of gamma-ray transitions from the decay of states above $41/2^-$ is presented in Figure 5.11(b) which was produced with a sum of triple

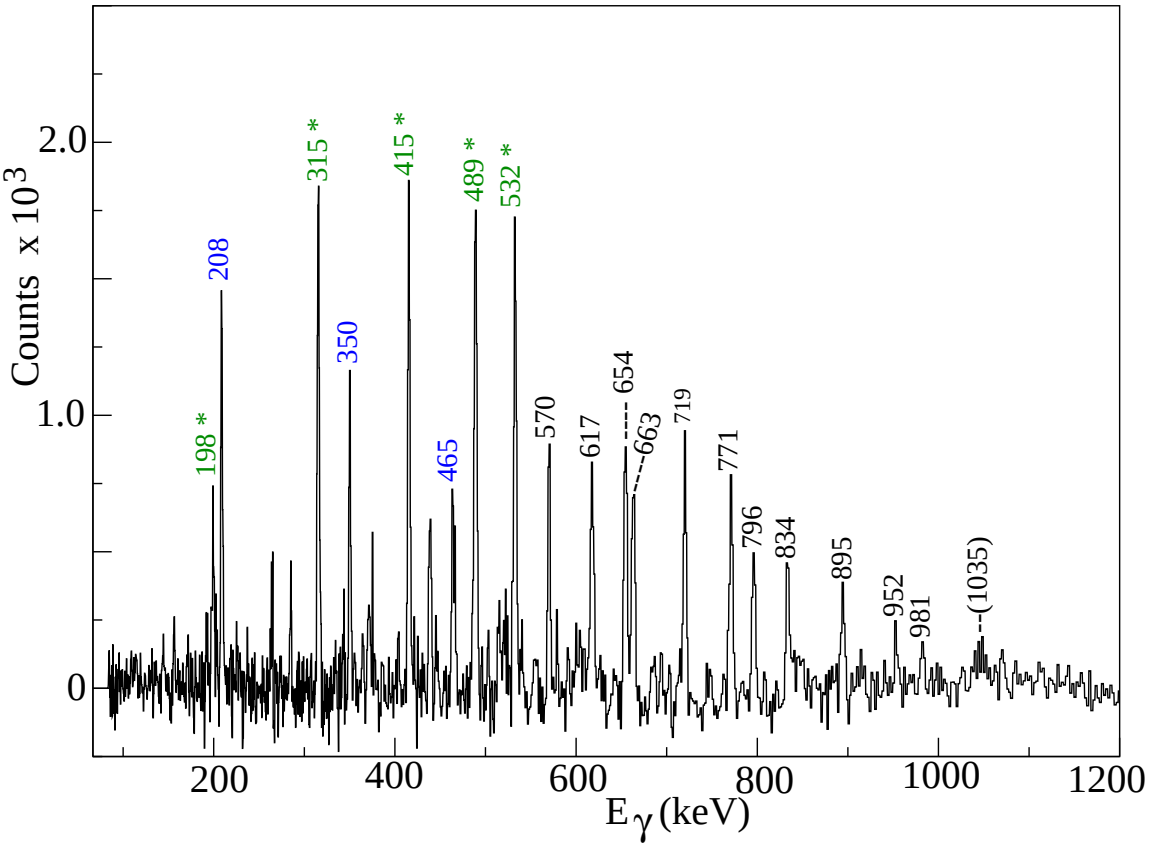

Figure 5.12: Spectrum produced with a sum of triple gates set on the in-band transitions of Band 5, from the decay of the $33/2^-$ state up to $61/2^-$ state. Transitions in band 5 can be seen, with the five first transitions of the ground state and the most intense first three transitions of the yrast band. The transitions of the ground state band are marked with asterisks and yrast transitions in blue.

gates set on in-band transitions from the decay of the $33/2^-$ state to the $69/2^-$ state in coincidence with 1046-keV. The excitation energy of Band 4 has been altered from 2007-keV to 2085-keV as shown in the decay scheme Figure 5.2. The obtained angular intensity-ratios confirm that the 385-keV and 540-keV transitions have stretched electric quadrupole (E2) character, and 640-keV transition is of a stretched electric dipole (E1) charactor, as illustrated in Figure 5.3, and Tables 5.5 and 5.3. Thus the first transition in this band becomes 464-keV.

Band	$E_{ex.}$ (keV)	E_γ (keV)	I_γ	R	Multipol.	Transition
5→2	2662.5	654.1	2.1(0.2)	0.96(0.06)	E2	$29/2^- \rightarrow 25/2^-$
5	3232.7	570.0	1.9(0.2)	0.91(0.03)	E2	$33/2^- \rightarrow 29/2^-$
	3849.6	617.2	1.8(0.2)	0.84(0.02)	E2	$37/2^- \rightarrow 33/2^-$
	4512.5	662.9	1.7(0.2)	0.97(0.06)	E2	$41/2^- \rightarrow 37/2^-$
	5231.6	719.1	1.5(0.2)	0.96(0.05)	E2	$45/2^- \rightarrow 41/2^-$
	6002.2	770.6	1.4(0.2)	0.93(0.09)	E2	$49/2^- \rightarrow 45/2^-$
	6797.8	795.6	1.2(0.2)	0.92(0.08)	E2	$53/2^- \rightarrow 49/2^-$
	7631.9	834.1	1.1(0.2)	0.91(0.02)	E2	$57/2^- \rightarrow 53/2^-$
	8526.9	895.0	1.0(0.2)	0.86(0.07)	E2	$61/2^- \rightarrow 57/2^-$
	9478.7	951.7	0.9(0.1)	0.98(0.12)	E2	$65/2^- \rightarrow 61/2^-$
	10455.4	981.1	0.8(0.1)	0.91(0.03)	E2	$69/2^- \rightarrow 65/2^-$
	11495.1	(1035.4)	0.7(0.1)	0.96(0.07)	E2	$(73/2^-) \rightarrow 69/2^-$

Table 5.6: Illustrates the measured properties (Relative intensity, Angular-intensity ratios and multipolarity assignment) of the γ-ray transitions in Band 5 of ^{159}Er.

5.4.6 Band 5 (−, +1/2)

Band 5 has not been discussed previously, but a sequence of four gamma-rays with energies of 570-keV, 617-keV, 663-keV and 719-keV appearing to decay into the $25/2^-$ state of Band 2 , has previously been observed by Deleplanque *et al.,*[Del87]. The present results indicate that Band 5 has the same parity and signature as the Band 2, ground state band (−,+1/2), and is based on these four transitions, decaying to the $25/2^-$ state of the ground state band by a newly found gamma-ray transition of enregy 654-keV. The nature of this decay has been established definitely as a stretched E2 transition, using the angular intensity-ratio measurement technique, which confirms the assignment of negative parity for Band 5. Furthermore, Band 5 has been extended up to possible state of $(73/2^-)$ with a sequence of six new stretched E2 transitions, and in addition a tentatively assigned (1035)-keV transition. A coincidence spectrum

of transitions in Band 5, which shows them to be in coincidence with the transitions in Band 2 up to the $25/2^-$ state, is displayed in Figure 5.12. This is produced from employing a sum of triple gates of in-band transitions from the decay of the $33/2^-$ state to the $61/2^-$ state. Table 5.6 illustrates the properties of all the transitions in Band 5.

5.4.7 Band 10 (−, −1/2)

A sequence of three tentative coincidence transitions of gamma-ray energies 1053-keV, 1005-keV and 941-keV has been previously observed by Deleplanque *et al.,*[Del87], and thought to decay to the main level scheme through the $81/2^+$ state in the yrast band. In the present analysis, the transitions have been found to be part of a new rotational sequence, Band 10, of ten low intensity transitions and a tentative transition, which extends from $(51/2^-)$ up to a possible $(95/2^-)$ state. This band depopulates mainly to the $49/2^+$ and $53/2^+$ states of the yrast band through 1029-keV and 1005-keV transitions, but also decays to the $51/2^-$ and $55/2^-$ states of Band 3 through 1143-keV and 1170-keV transitions. The 1005-keV gamma-ray appeared remarkably strongly in coincidence with transitions of the yrast band, and this gamma-ray (1005 keV) looks to be in coincidence with the 1004-keV gamma-ray ordered after the 884-keV and 945-keV transitions. Photopeaks of coincidence transitions observed in Band 10 are presented in the spectrum of Figure 5.13, which were observed in coincidence with the transitions in the yrast band up to state $53/2^+$. This spectrum is produced with a sum of triple gates set on in-band transitions from the decay of the $(55/2^-)$ state to the $(91/2^-)$ state, shows the 805-keV, 884-keV, 945-keV, 1004-keV, 1054-keV, 1085-keV, 1146-keV, 1208-keV and 1295-keV transitions in this new band, in coincidence with the first three transitions, 208-keV, 350-keV and 465-keV, of the yrast band. The angular intensity-ratio measurement for the linking transition of 1143-keV is consistent with the value of that of a stretched electric quadrupole (E2) transition, suggesting that Band 10 has negative parity and a signature of $-1/2$. The measurements for gamma-ray transitions are tabulated in Table 5.7, the multipolarity

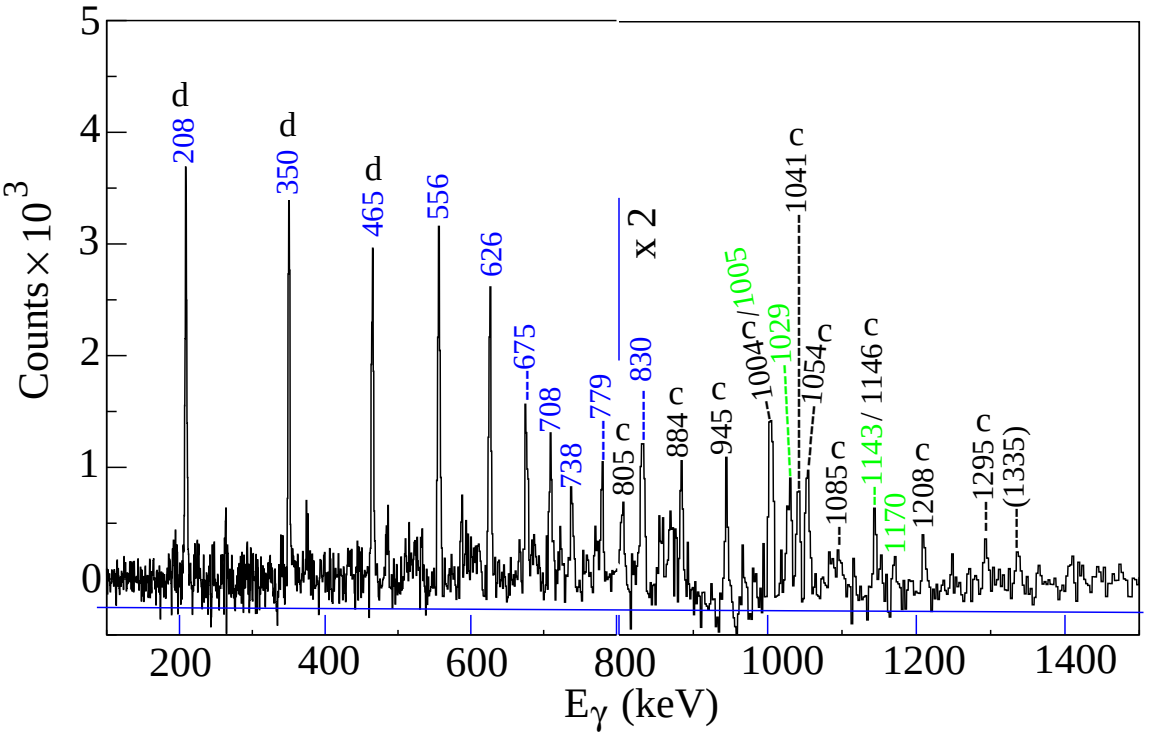

Figure 5.13: Coincidence spectra produced with a sum of triple gates set on in-band transitions in the Band 10 of ^{159}Er from the decay of the $(55/2^-)$ state to the $(91/2^-)$ state, marked with c, in coincidence with the first three transitions, 208-keV, 350-keV and 465-keV, of the yrast band marked with d. The transitions of the yrast band are marked in blue and linking transitions in green.

of the majority of transitions in Band 10 have not been assigned, due to this band being extremely weakly populated with low intensity transitions.

5.4.8 TSD 1 (−, +1/2)

This band comprises of ten weakly populated transitions of 911-keV, 948-keV, 990-keV, 1034-keV, 1074-keV, 1114-keV, 1151-keV, 1214-keV, 1270-keV and 1341-keV, which were observed previously by Ollier and Simpson [Oll09] in a study of the triaxial strongly deformed structures in ^{159,160}Er. The spectrum of this weakly populated structure is shown in Figure 5.14. The gamma-ray transitions in the TSD1 band are

Band	$E_{ex.}$ (keV)	E_γ (keV)	I_γ	R	Multipol.	Transition
10→yrast	63578.5	1029.3	2.0(0.4)			$(51/2^-) \rightarrow 49/2^+$
10	7163.4	805.4	1.5(0.3)	0.97(0.1)	E2	$(55/2^-) \rightarrow (51/2^-)$
10→yrast		1004.9	0.9(0.4)			$(55/2^-) \rightarrow 53/2^+$
10→3		1142.7	0.8(0.1)	0.94(0.06)	E2	$(55/2^-) \rightarrow 51/2^-$
10	8047.0	883.6	1.5(0.3)	0.99(0.01)	E2	$(59/2^-) \rightarrow (55/2^-)$
10→3		1170.4	0.7(0.2)			$(59/2^-) \rightarrow 55/2^-$
10	8991.6	944.6	1.4(0.3)	0.93(0.03)	E2	$(63/2^-) \rightarrow (59/2^-)$
	9995.5	1003.8	1.3(0.3)	0.85(0.03)	E2	$(67/2^-) \rightarrow (63/2^-)$
	11036.0	1040.6	1.2(0.3)			$(71/2^-) \rightarrow (67/2^-)$
	12090.3	1054.3	1.0(0.2)			$(75/2^-) \rightarrow (71/2^-)$
	13174.9	1084.6	0.9(0.3)	0.94(0.07)	E2	$(79/2^-) \rightarrow (75/2^-)$
	14320.7	1145.7	0.8(0.3)			$(83/2^-) \rightarrow (79/2^-)$
	15528.7	1208.2	0.6(0.3)	0.98(0.16)	E2	$(87/2^-) \rightarrow (83/2^-)$
	16823.8	1295.1	0.5(0.2)			$(91/2^-) \rightarrow (87/2^-)$
	18158.5	(1334.7)	0.4(0.2)			$(95/2^-) \rightarrow (91/2^-)$

Table 5.7: Illustrates the measured properties (Relative intensity, Angular-intensity ratios and multipolarity assignment) of the γ-ray transitions in Band 10 of ^{159}Er.

observed in coincidence with transtions of the yrast band in ^{159}Er. This spectrum was produced with a sum of double gates set on all transitions in the TSD1 band, in the three dimensional (E_γ^3) cube analysis. The multipolarity of the transitions, or the spins and parities of the states, could not be assigned definitely. The assignments have previously ([Oll09]) been assumed to be E2 transitions in the calculation of the dynamic moment of inertia $\mathcal{J}^{(2)}$, for a negative parity band of signature $-1/2$. The excitation energy of this band assumed on the comparisons with results from Cranked Nilsson-Strutinsky (CNS) calculations [Oll09]. The measured gamma-ray energies and relative intensities of the transitions in the TSD1 band are presented in Table 5.8.

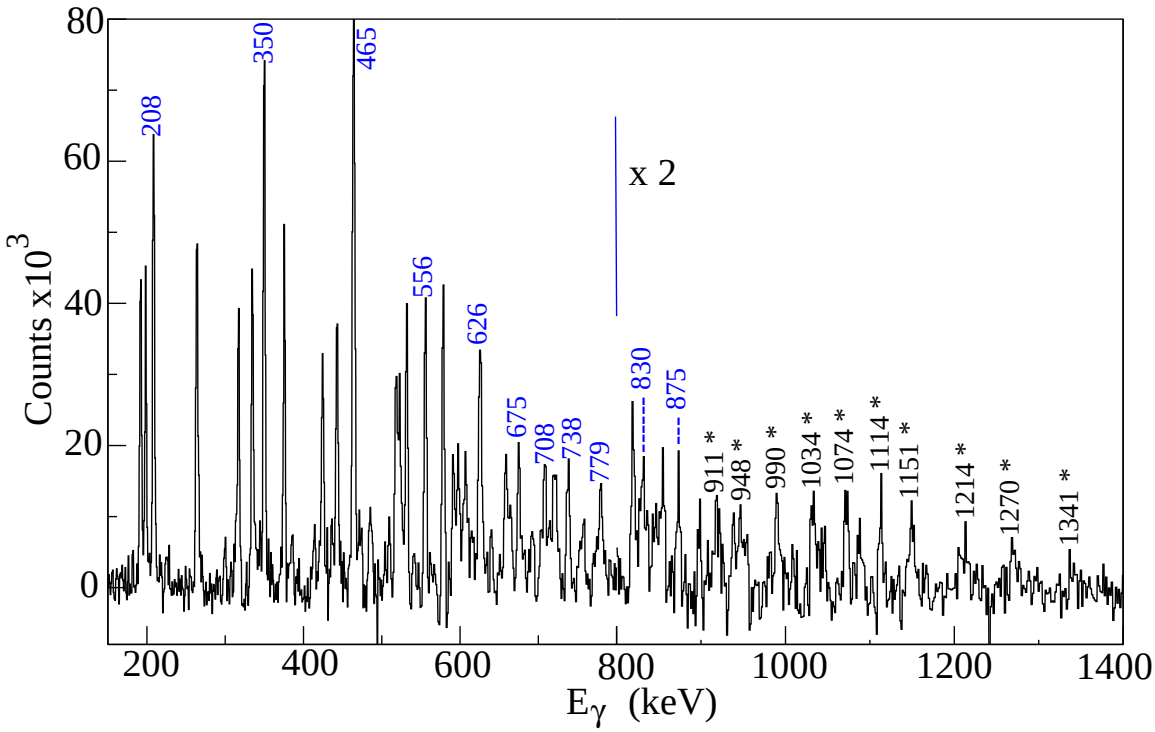

Figure 5.14: A spectrum produced with a sum of double gates set on transitions of the 911-keV, 948-keV, 990-keV, 1034-keV, 1074-keV, 1114-keV, 1151-keV, 1214-keV, 1270-keV and 1341-keV gamm-rays marked with asterisks. All transitions in the Triaxial Strongly Deformed band (TSD1) are in coincidence with transitions of the yrast band in ^{159}Er.

5.4.9 Gamma Vibrational Band (+, +1/2)

The gamma-vibrational band in ^{159}Er was unknown previously. A new sequence of fifteen in-band gamma-ray transitions has been observed for the first time in the current work. The excited states from $21/2^+$ to $49/2^+$ in this band are strongly coupled to the yrast, through a series of high-energy gamma-ray transitions of 1015-keV, 1104-keV, 1135-keV, 1128-keV, 1113-keV, 1119-keV, 1168-keV and 1235-keV. The linking transition at each state was observed in coincidence by setting double gates on two coincidence gamma-rays above the state of interest. A representative

Band	$E_{ex.}$ (keV)	E_γ (keV)	I_γ	R	Multipol.	Transition
TSD1	(8619.4)	911.0	1.15(0.5)			$(61/2^-) \rightarrow (57/2^-)$
	(9567.4)	948.0	1.14(0.5)			$(65/2^-) \rightarrow (61/2^-)$
	(10557.8)	990.5	1.1(0.3)			$(69/2^-) \rightarrow (65/2^-)$
	(11591.4)	1033.6	1.0(0.3)			$(73/2^-) \rightarrow (69/2^-)$
	(12665.0)	1073.6	0.9(0.2)			$(77/2^-) \rightarrow (73/2^-)$
	(13778.6)	1113.6	0.8(0.2)			$(81/2^-) \rightarrow (77/2^-)$
	(14929.6)	1151.0	0.7(0.2)			$(85/2^-) \rightarrow (81/2^-)$
	(16143.3)	1213.7	0.6(0.1)			$(89/2^-) \rightarrow (85/2^-)$
	(17413.8)	1270.5	0.5(0.1)			$(93/2^-) \rightarrow (89/2^-)$
	(18754.6)	1340.9	0.4(0.1)			$(97/2^-) \rightarrow (91/2^-)$

Table 5.8: The measured properties of the γ-ray transitions in TSD1 band of ^{159}Er.

spectra for coincidence transitions in this band is shown in Figure 5.15, produced with a sum of triple gates on low-spin transitions from the decays of the $21/2^+$ state to the $57/2^+$ state in coincidence with the 208-keV yrast transition is displayed in (a), whilst the coincidence events from a sum of triple gates set on transitions from the decay of the $21/2^+$ state to the $57/2^+$ state is displayed in (b). The coincidence events in Figure 5.15(b) clearly show the 360 keV transition that populates a tentative state $(17/2^+)$ below the state $21/2^+$. The spectra show extremely low intensity coincidence transitions of gamma-ray energies 489-keV, (499)-keV, (639)-keV and 666-keV, which are connecting γ-vibrational band at low spins $(17/2^+)$, $21/2^+$ and $25/2^+$ to the yrast band and with its signature partner (Band 1) through a $\Delta I = 1$ transition. Thus the band-head excitation energy of the γ-vibrational band has been identified at 1089-keV. Angular intensity-ratios have been measured for seven of the linking transitions, and all are consistent with that of a stretched electric quadrupole (E2) transitions, which means this band can be assigned positive-parity with signature (+, 1/2). The assignment of the multipolarity of in-band transitions means the spin and parity of states has been identified from $21/2^+$ to $61/2^+$. The measured transition energies,

relative intensities and angular intensity-ratios for the gamma-rays in the γ-vibrational band are presented in Table 5.9.

5.5 Strongly Coupled High K Structures

The partial level scheme for ^{159}Er constructed from the present work showing the strongly coupled high-K structures is displayed in Figure 5.16. Three strongly coupled structures associated with transitions in ^{159}Er have been observed by Simpson *et al.,* [Sim98], but in this work only two strongly coupled high-K bands were observed. The first pair are labelled as Bands 6 and 7 and the second structure comprises of the coupling of Bands 8 and 9. The third strongly coupled band is not reported in the current work, and it has been associated with transitions in ^{161}Er and discussed in [Che11]. Angular intensity-ratio measurements have been performed to confirm the multipolarity of linking transitions, as well as in-band and crossover transitions in the coupled bands, observed previously by Simpson *et al.,* [Sim98] and Deleplanque *et al.,* [Del87]. Typical measurements for the angular intensity-ratios as a function of transition energy for gamma-ray transitions in the two strongly coupled high-K structures in ^{159}Er are presented in Figure 5.17.

5.5.1 Strongly Coupled Bands 6 and 7

The first candidate for a strongly coupled high-K structure in ^{159}Er was observed by Deleplanque *et al.,* [Del87], and in the present work is represented by Bands 6 and 7 in Figure 5.16. This coupled band had previously been extended by Simpson *et al.,* [Sim98] up to spin $87/2^-$ and $85/2^-$ by two transitions for each signature, and in addition two linking transitions were observed. The two transitions decaying out of the structure are the 1795-keV and 1445-keV gamma-rays linking the tentatively assigned $19/2^-$ state in Band 6 to the $17/2^+$ and $21/2^+$ yrast states. The spin and parity of Band 7 levels had in fact been previously assigned by Deleplanque *et al.,* [Del87] based on the angular intensity-ratio measurements for linking transitions

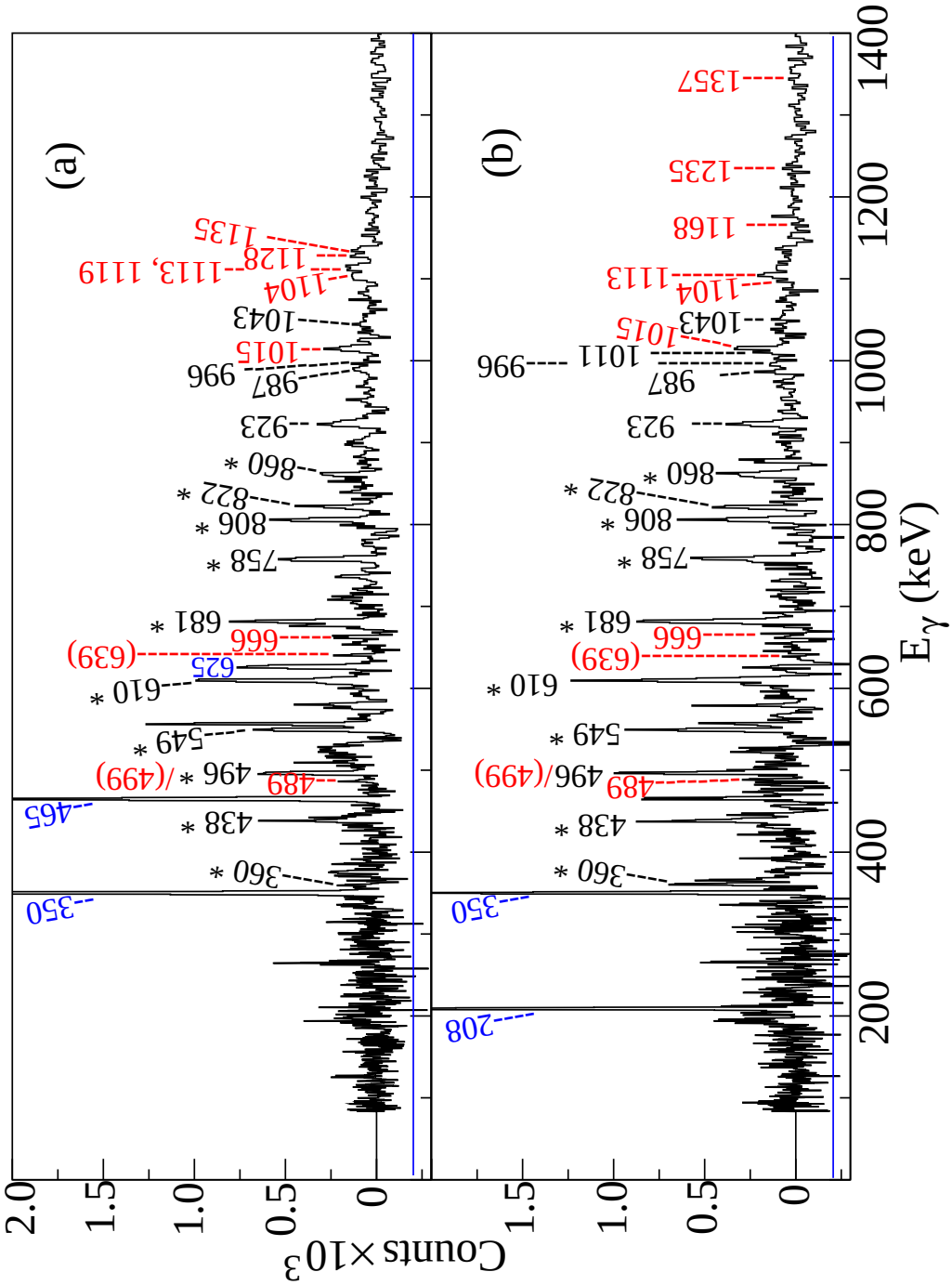

Figure 5.15: Coincidence spectra showing transitions in γ-vibrationl band of ^{159}Er. Spectrum (a) produced with a sum of triple gates on in-band transitions in γ-Vibrationl band (marked with asterisks) from the decay of the $21/2^+$ state to the $57/2^+$ state in coincidence with the 208-keV yrast transition. Spectrum (b) is produced with a sum of triple gates set on the in-band transitions marked with asterisks to display a transition of 360-keV in coincidence with low-spin linking transitions and in-band transitions of the γ-vibration band.

Band	$E_{ex.}$ (keV)	E_γ (keV)	I_γ	R	Multipol.	Transition
γ-Band$\rightarrow$1	1089	(499.4)	0.6(0.1)			$(17/2^+) \rightarrow 15/2^+$
γ-Band	1448.7	359.6	1.5(0.5)			$21/2^+ \rightarrow (17/2^+)$
$\rightarrow$yrast		665.9	0.8(0.1)			$21/2^+ \rightarrow 21/2^+$
		1015.4	1.9(0.3)	0.86(0.07)	E2	$21/2^+ \rightarrow 17/2^+$
$\rightarrow$1		489.4	0.7(0.2)			$21/2^+ \rightarrow 19/2^+$
γ-Band	1886.3	437.6	2.6(0.3)	1.12(0.13)	E2	$25/2^+ \rightarrow 21/2^+$
$\rightarrow$yrast		(638.9)	0.9(0.2)			$25/2^+ \rightarrow 25/2^+$
$\rightarrow$yrast		1103.5	1.5(0.2)	0.8(0.08)	E2	$25/2^+ \rightarrow 21/2^+$
γ-Band	2381.9	495.6	2.3(0.2)	1.06(0.09)	E2	$29/2^+ \rightarrow 25/2^+$
$\rightarrow$yrast		1134.5	2.1(0.1)	1.1(0.14)	E2	$29/2^+ \rightarrow 25/2^+$
γ-Band	2931.0	549.1	1.9(0.1)	0.98(0.13)	E2	$33/2^+ \rightarrow 29/2^+$
$\rightarrow$yrast		1127.9	2.0(0.1)	0.81(0.07)	E2	$33/2^+ \rightarrow 29/2^+$
γ-Band	3541.4	610.5	4.8(0.4)	0.91(0.09)	E2	$37/2^+ \rightarrow 33/2^+$
$\rightarrow$yrast		1112.8	3.5(0.4)	0.86(0.05)	E2	$37/2^+ \rightarrow 33/2^+$
γ-Band	4222.3	680.9	4.5(0.4)	0.98(0.15)	E2	$41/2^+ \rightarrow 37/2^+$
$\rightarrow$yrast		1118.7	1.7(0.4)	0.86(0.05)	E2	$41/2^+ \rightarrow 37/2^+$
γ-band	4980.0	757.7	3.3(0.3)	0.85(0.03)	E2	$45/2^+ \rightarrow 41/2^+$
$\rightarrow$yrast		1168.2	1.4(0.3)	0.97(0.1)	E2	$45/2^+ \rightarrow 41/2^+$
γ-Band	5785.6	805.5	1.9(0.3)	0.86(0.13)	E2	$49/2^+ \rightarrow 45/2^+$
$\rightarrow$yrast		1235.4	0.9(0.1)	1.16(0.16)	E2	$49/2^+ \rightarrow 45/2^+$
γ-Band	6607.4	821.8	1.7(0.3)	0.97(0.10)	E2	$53/2^+ \rightarrow 49/2^+$
γ-Band	7467.7	860.0	1.6(0.3)	0.99(0.13)	E2	$57/2^+ \rightarrow 53/2^+$
γ-Band	8390.5	922.9	1.5(0.3)	0.87(0.06)	E2	$61/2^+ \rightarrow 57/2^+$
$\rightarrow$yrast		1357.3	1.0(0.2)			$61/2^+ \rightarrow 57/2^+$
γ-Band	9377.2	986.6	1.3(0.1)			$(65/2^+) \rightarrow 61/2^+$
	10387.8	1010.6	1.2(0.1)			$(69/2^+) \rightarrow (65/2^+)$
	11383.7	995.8	1.1(0.1)	1.1(0.17)	E2	$(73/2^+) \rightarrow (69/2^+)$
	12426.9	1043.3	0.8(0.1)	0.8(0.11)	E2	$(77/2^+) \rightarrow (73/2^+)$

Table 5.9: Illustrates the measured properties (Relative intensity, Angular-intensity ratios and multipolarity assignment) of the γ-ray transitions in γ-Vibrational band of ^{159}Er.

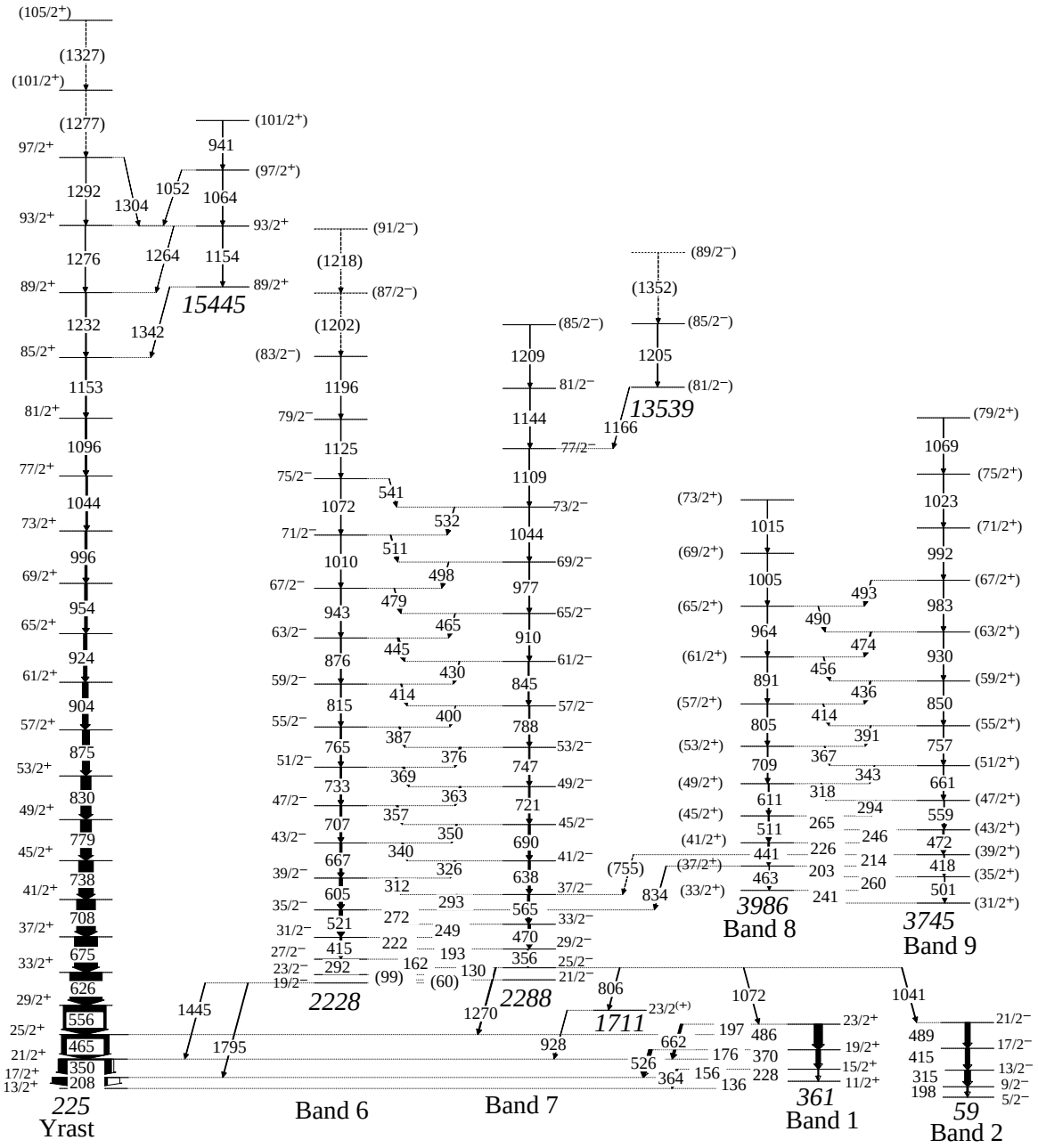

Figure 5.16: partial level scheme for ^{159}Er costructed from the present work for the strongly coupled bands connected with the yrast Band, Band 1 and Band 2. The transition energies are given in keV, and the width of the arrows indicate the relative intensities of the transitions. Beneath each band in italics, the bandhead energy is given in keV. Spins and parities are based on measurements of angular intensity-ratios, and parenthesis indicate tentative spin and parity assigments. Where the observation of a transition is considered tentative, a dashed arrow and parenthesis are used.

decaying from the state $25/2^-$ state. The 1270-keV transition decays to the $25/2^+$ excited state of the yrast band, the 1072-keV transition to the $23/2^+$ state of Band 1, the 1041-keV transition to the $21/2^-$ state of the Band 2, and the 806-keV transition decays to a tentative parity $23/2^{(+)}$ state of excitation energy 1711-keV. The present work confirms the previous observations of gamma-ray transition energies in Bands 6 and 7 with small differences of 1-2 keV from the previously reported values. The position of the 1166-keV, 1196-keV and 1209-keV transitions have been changed between favoured and unfavoured signature bands at high spins. In addition, Band 6 has been extended by two tentative transitions of (1202)-keV and (1218)-keV, and a new sequence of transitions of 1205-keV and (1352)-keV in parallel with band 7 has been established at high spin, which feed into the $77/2^-$ state via a previously observed transition of 1166-keV. Gamma-ray spectra in Figure 5.18 (a) and (b) show coincidence transitions in Bands 6 and 7. The spectrum in Figure 5.18 (a) is obtained from a sum of triple gates set on crossover transitions from 162-keV to 340-keV. The spectra confirm the linking transitions that connect Bands 6 and 7 to the yrast band and Bands 1 and 2, as well as the linking transitions with energy 806-keV and 929-keV which infer an excited state at 1171-keV. The spectrum in (b) is obtained from a sum of triple gates set on crossover transitions from 162-keV to 445-keV. The coincidence spectra from the decay of highest spin transitions in these strongly coupled bands are presented in Figures 5.19 (a) and (b), which were produced from a sum of triple gates set on crossover transitions from 130-keV to 326-keV in coincidence with (a) the 1072-keV, 1125-keV and 1196-keV transitions from Band 6 and (b) the 1109-keV transition from Band 7.

In the current work angular intensity-ratio measurements have been performed for these strongly coupled bands, the measurements for linking transitions confirm the previous multipolarity assignment for the 1270-keV. The value was consistent with that of the stretched electric dipole transition (E1). The multipolarity of the 806-keV gamma-ray, which decays to a tentative parity $23/2^{(+)}$ state and of the 928 keV transition decays from this tentative state to the yrast band, were found to have

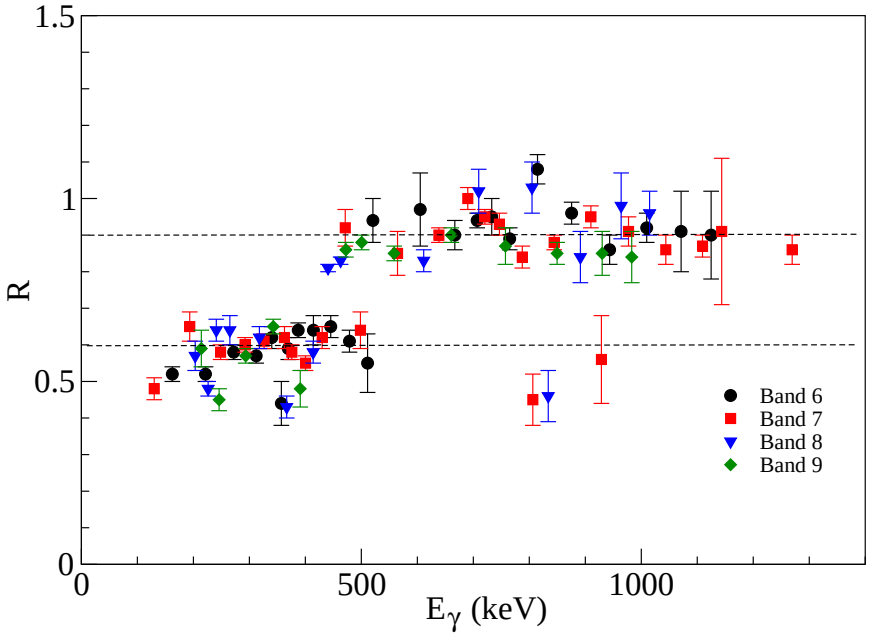

Figure 5.17: Angular intensity-ratios, R, for gamma-rays as a function of transition energy for the strongly coupled high-K bands in ^{159}Er, labelled as Band 6, Band 7, Band 8 and Band 9.

angular intensity-ratios consistent with the character of a stretched dipole (E1 or M1) transitions. Consequently the spin of the state at excitation energy of 1711-keV has been established as $23/2(^{+})$ with a tentative parity. The obtained values of the angular intensity-ratios for $\Delta I = 1$ crossover transitions and $\Delta I = 2$ in-band transtions were consistent with charactor of the mixed M1/E2 and of the stretched electric quadrupole (E2) transitions respectively. The gamma-ray energies, relative intensities, angular intensity-ratios, and the electromagnetic character of coincidence transitions in Bands 6 and 7 are presented in Tables 5.10, 5.11, 5.12 and 5.13.

5.5.2 Strongly Coupled Bands 8 and 9

Bands 8 and 9 in Figure 5.16 represent the second pair of strongly coupled bands in ^{159}Er, observed previously by Simpson *et al.,* [Sim98] with seven transitions in each signature. The bands for both signatures were connected via fourteen crossover

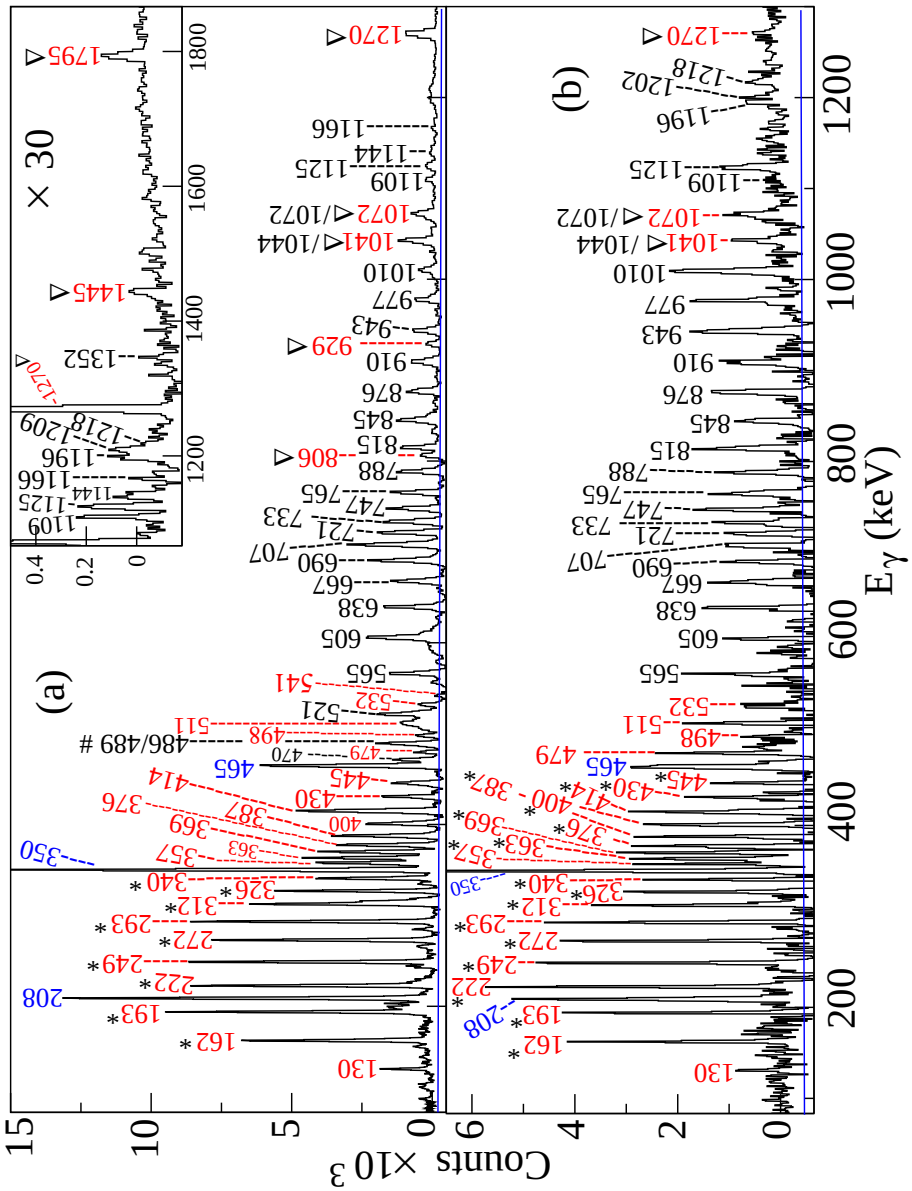

Figure 5.18: Coincidence spectra for gamma-ray transitions in strongly coupled bands 6 and 7 of ^{159}Er, produced with a sum of triple gates set on ΔI=1 transitions from the decay of the $27/2^-$ state to the $43/2^-$ state, and from the decay of the $27/2^-$ state to the $63/2^-$ state in (a) and (b) respectively, both spectra showing the transitions up to energy range of 1300-keV. The upper panel spectrum in (a) is magnified 30 times relative to the photo-peaks in (a) to display linking transitions of 1270-keV, 1445-keV and 1795 keV. The photopeaks correspond to crossover transitions are marked in red, yrast transitions in blue, those are correspond to the transitions in bands 1 and 2 are labelled with #, and the linking transitions are labelled with triangles.

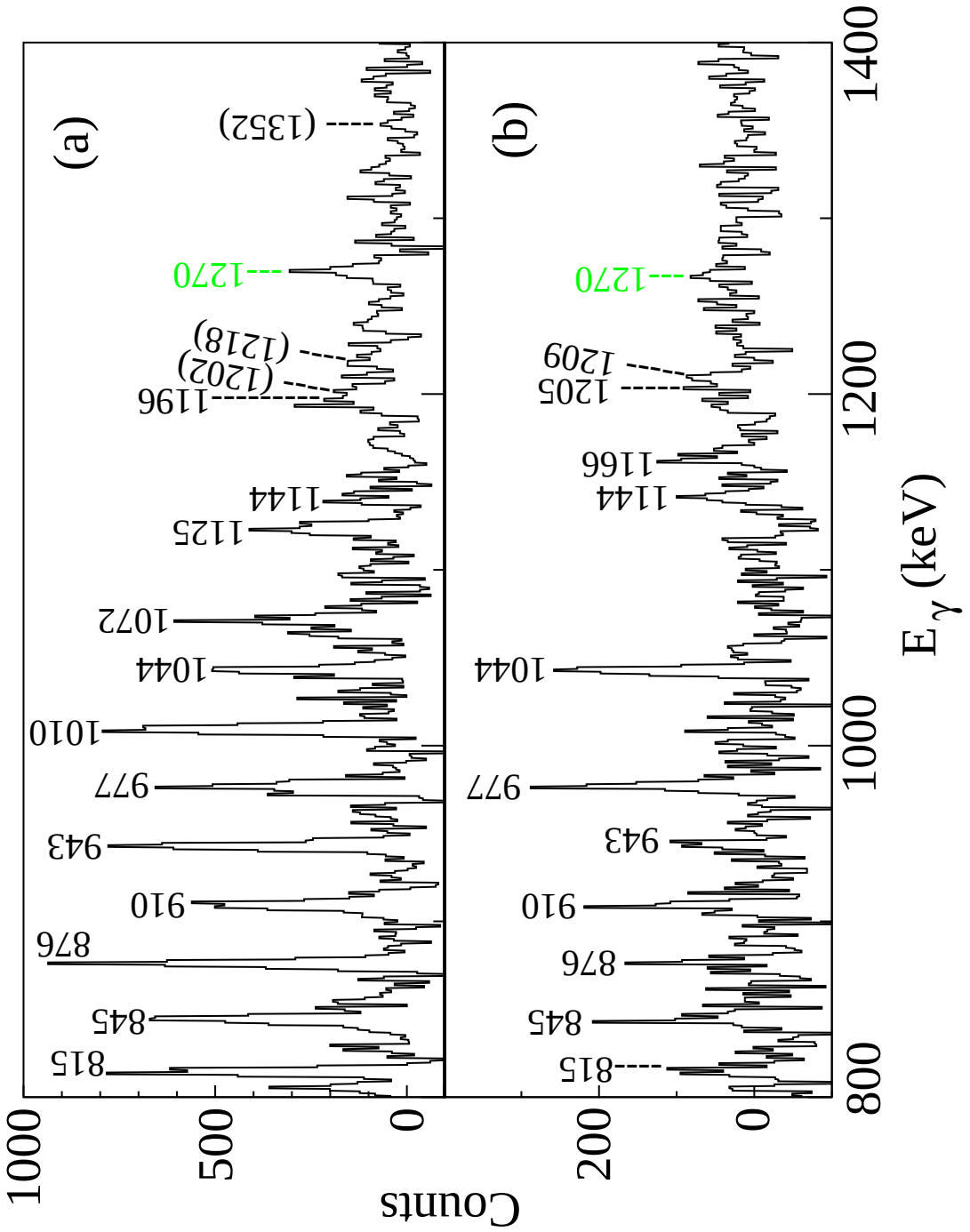

Figure 5.19: The spectra produced with a sum of triple gates set on $\Delta I = 1$ transitions from 130-keV to 326-keV in the strongly coupled bands 6 and 7, and (a) the 1072-keV, 1125-keV and 1196-keV transitions from Band 6, and (b) the 1109-keV transition from Band 7. Spectra demonstates all in-band transitions observed from decay of states above $55/2^-$ and the presense of photopeaks at highest spin. Photopeaks that correspond to linking transitions are marked with green.

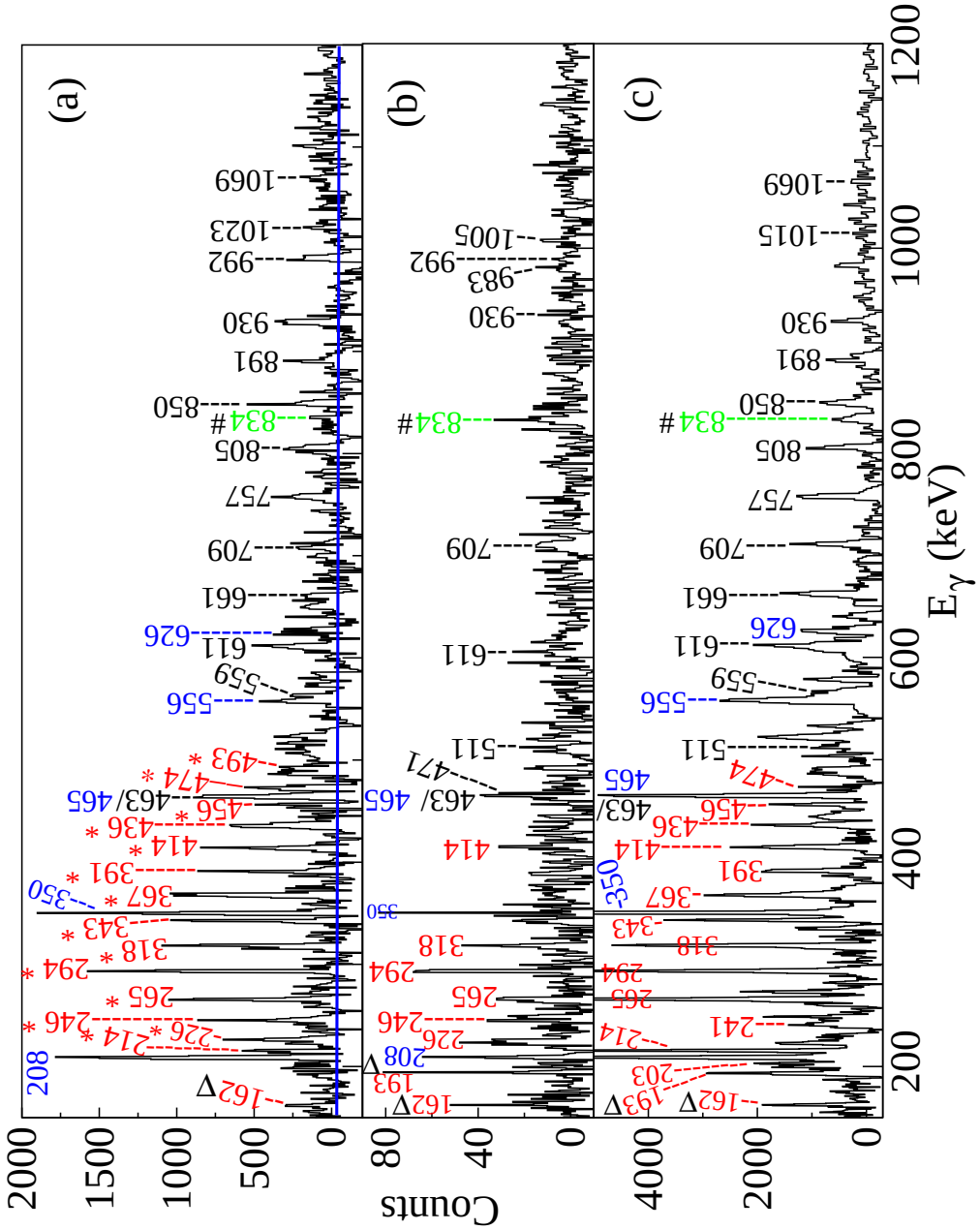

Figure 5.20: Coincidence spectra for gamma-ray transitions in strongly coupled bands and 9 of ^{159}Er, (a) produced with a sum of triple gates set on $\Delta I = 1$ transitions marked with asterisks, from the $(33/2^+)$ state to the $(67/2^+)$ state incoincidence with the 983-keV transition, spectrum (b) was produced with a triple gate set on the 249-keV and 272-keV transitions, from the decay of Bands 6 and 7, and the 214-keV transition from band 9, and (c) was produced with a double gate on 226-keV and 246-keV transitions from the decay of the $(41/2^+)$ and $(43/2^+)$ states in bands 8 and 9. The photopeaks corresponding to crossover transitions are marked in red, the low-spin transitions in bands 6 and 7 are labelled with triangles, yrast transitions are marked in blue, and the linking transitions of 834-keV are labelled with #.

Band	$E_{ex.}$ (keV)	E_γ (keV)	I_γ	R	Multipol.	Transition
6→yrast	2228.0	1445.2	1.2(0.2)			$(19/2^-) \rightarrow 21/2^+$
		1794.7	1.4(0.2)			$(19/2^-) \rightarrow 17/2^+$
6→7	2387.1	(99.4)	0.5(0.05)			$23/2^- \rightarrow (21/2^-)$
6	2679.3	292.2	1.8(0.1)		E2*	$27/2^- \rightarrow 23/2^-$
6→7		162.4	1.9(0.1)	0.55(0.2)	M1/E2	$27/2^- \rightarrow 25/2^-$
6	3094.3	415.1	3.6(0.1)		E2	$31/2^- \rightarrow 27/2^-$
6→7		221.6	5.5(0.2)	0.52(0.02)	M1/E2	$31/2^- \rightarrow 29/2^-$
6	3615.0	520.7	6.2(0.2)	0.94(0.06)	E2	$35/2^- \rightarrow 31/2^-$
6→7		272.0	4.8(0.2)	0.58(0.02)	M1/E2	$35/2^- \rightarrow 33/2^-$
6	4219.7	605.2	5.7(0.4)	0.97(0.10)	E2	$39/2^- \rightarrow 35/2^-$
6→7		312.2	3.7(0.2)	0.57(0.02)	M1/E2	$39/2^- \rightarrow 37/2^-$
6	4886.2	667.0	3.4(0.2)	0.90(0.04)	E2	$43/2^- \rightarrow 39/2^-$
6→7		340.1	2.9(0.1)	0.62(0.03)	M1/E2	$43/2^- \rightarrow 41/2^-$
6	5593.4	706.8	3.6(0.3)	0.94(0.02)	E2	$47/2^- \rightarrow 43/2^-$
6→7		357.1	2.7(0.1)	0.44(0.06)	M1/E2	$47/2^- \rightarrow 45/2^-$
6	6325.6	732.9	2.6(0.2)	0.95(0.05)	E2	$51/2^- \rightarrow 47/2^-$
6→7		369.5	3.2(0.2)	0.59(0.03)	M1/E2	$51/2^- \rightarrow 49/2^-$
6	7088.6	764.9	2.4(0.1)	0.89(0.03)	E2	$55/2^- \rightarrow 51/2^-$
6→7		387.3	2.1(0.1)	0.64(0.02)	M1/E2	$55/2^- \rightarrow 53/2^-$
6	7903.3	814.7	1.8(0.1)	1.08(0.04)	E2	$59/2^- \rightarrow 55/2^-$
6→7		414.4	1.7(0.2)	0.64(0.02)	M1/E2	$59/2^- \rightarrow 57/2^-$
6	8778.9	875.6	1.8(0.2)	0.96(0.03)	E2	$63/2^- \rightarrow 59/2^-$
6→7		445.4	3.2(0.2)	0.65(0.03)	M1/E2	$63/2^- \rightarrow 61/2^-$
6	9722.3	943.5	1.6(0.2)	0.86(0.04)	E2	$67/2^- \rightarrow 63/2^-$
6→7		478.8	1.3(0.1)	0.47(0.03)	M1/E2	$67/2^- \rightarrow 65/2^-$
6	10732.0	1009.7	1.5(0.2)	0.92(0.04)	E2	$71/2^- \rightarrow 67/2^-$
6→7		511.2	1.6(0.2)	0.55(0.08)	M1/E2	$71/2^- \rightarrow 69/2^-$
6	11803.7	1071.8	1.1(0.2)	0.91(0.11)	E2	$75/2^- \rightarrow 71/2^-$
6→7		540.6	0.7(0.2)	0.47(0.03)	M1/E2	$75/2^- \rightarrow 73/2^-$

Table 5.10: Illustrates the measured properties (Relative intensity, Angular-intensity ratios and multipolarity assignment) of the γ-ray transitions in Band 6 of ^{159}Er, * the multipolarity of 1040.9 keV transition assigned acoording to [Del87].

Band	$E_{ex.}$ (keV)	E_γ (keV)	I_γ	R	Multipol.	Transition
6	12928.5	1124.8	1.0(0.2)	0.9(0.12)	E2	$79/2^- \rightarrow 75/2^-$
6	14124.2	1195.6	0.9(0.2)			$(83/2^-) \rightarrow 79/2^-$
6	15326.2	(1202.0)	0.8(0.2)			$(87/2^-) \rightarrow (83/2^-)$
6	16544.2	(1218.0)	0.7(0.16)			$(91/2^-) \rightarrow (87/2^-)$

Table 5.11: Illustrates the measured properties (Relative intensity, Angular-intensity ratios and multipolarity assignment) of the γ-ray transitions form the decay of states above $75/2^-$ in Band 6 of ^{159}Er.

transitions. It was predicted that these coupled bands decay to Bands 6 and 7, but the nature of connection was never established. The nature of the connection has been identifed for the first time in this work, through the 834-keV gamma-ray. The spectra presented in Figure 5.20 clearly show this gamma-ray in coincidence with the low-spin sequences of Bands 6 and 7 and the transitions in Bands 8 and 9, confirming that Band 6 is linked to Band 8 through the 834 keV transition. The coincidence spectrum in (b) was produced with a triple gate set on the 249-keV and 272-keV transitions, from the decay of Bands 6 and 7, and the 214-keV transition from band 9, and the spectrum (c) was produced with a double gate on 226-keV and 246-keV transitions from the decay of the $(41/2^+)$ and $(43/2^+)$ states in bands 8 and 9. The angular intensity-ratio measurement for this transition indicates that its value is consistent with that of a stretched dipole (M1 or E1) transition, which fits the decay path from the $(37/2^+)$ state to the $35/2^-$ state, from Band 8 to Band 6. Furthermore, a tentative transition of 755 keV connects Band 9 with Band 7, through the decay path from the $(39/2^+)$ state to the $37/2^-$ state.

In the present work extentions have been established to low-spin and high-spin structures, three new weakly populated gamma-ray transitions of energies 418-keV, 463-keV and 501-keV have been found at the bottom of Bands 8 and 9, and the new states at bottom of the bands are connected through the 241-keV, 260-keV and 203-keV new crossover transitions.

Band	$E_{ex.}$(keV)	E_γ(keV)	I_γ	R	Multipol.	Transition
7→6	2289.7	(59.7)	0.3(0.01)			$(21/2^-) \rightarrow 19/2^-$
7→2	2516.9	1040.9	1.5(0.2)		E2*	$25/2^- \rightarrow 21/2^-$
7→yrast		1269.5	2.1(0.03)	0.86(0.04)	E1	$25/2^- \rightarrow 25/2^+$
7→1		1072.1	1.25(0.2)		E1*	$25/2^- \rightarrow 23/2^+$
7→6		130.1	0.8(0.05)	0.48(0.03)	M1/E2	$25/2^- \rightarrow 23/2^-$
$\rightarrow 23/2^{(+)}$		806.3	1.1(0.2)	0.45(0.07)	E1 or M1	$25/2^- \rightarrow 23/2^{(+)}$
$^{(+)} \rightarrow$yr.	1711.0	928.8	1.0(0.2)	0.56(0.12)	E1 or M1	$23/2^{(+)} \rightarrow 21/2^+$
7	2872.8	355.9	1.7(0.1)		E2*	$29/2^- \rightarrow 25/2^-$
7→6		193.5	6.6(0.2)	0.65(0.04)	M1/E2	$29/2^- \rightarrow 27/2^-$
7	3343.0	471.3	4.4(0.2)	0.92(0.05)	E2	$33/2^- \rightarrow 29/2^-$
7→6		248.6	4.7(0.1)	0.58(0.02)	M1/E2	$33/2^- \rightarrow 31/2^-$
7	3907.6	564.6	4.2(0.4)	0.85(0.06)	E2	$37/2^- \rightarrow 33/2^-$
7→6		292.5	2.5(0.1)	0.6(0.02)	M1/E2	$37/2^- \rightarrow 35/2^-$
7	4546.0	638.5	3.8(0.3)	0.90(0.02)	E2	$41/2^- \rightarrow 37/2^-$
7→6		326.3	2.8(0.1)	0.61(0.02)	M1/E2	$41/2^- \rightarrow 39/2^-$
7	5236.3	690.1	3.5(0.2)	1.00(0.03)	E2	$45/2^- \rightarrow 41/2^-$
7→6		350.1	2.2(0.2)			$45/2^- \rightarrow 43/2^-$
7	5956.1	720.6	3.0(0.3)	0.95(0.02)	E2	$49/2^- \rightarrow 45/2^-$
7→6		362.7	3.1(0.2)	0.62(0.03)	M1/E2	$49/2^- \rightarrow 47/2^-$
7	6701.4	746.6	2.6(0.2)	0.93(0.03)	E2	$53/2^- \rightarrow 49/2^-$
7→6		375.8	3.3(0.3)	0.58(0.02)	M1/E2	$53/2^- \rightarrow 51/2^-$
7	7488.9	787.5	2.4(0.2)	0.84(0.03)	E2	$57/2^- \rightarrow 53/2^-$
7→6		400.3	1.0(0.04)	0.55(0.02)	M1/E2	$57/2^- \rightarrow 55/2^-$
7	8333.4	844.5	2.1(0.3)	0.88(0.02)	E2	$61/2^- \rightarrow 57/2^-$
7→6		430.1	1.3(0.1)	0.62(0.03)	M1/E2	$61/2^- \rightarrow 59/2^-$
7	9242.4	910.0	2.0(0.2)	0.95(0.03)	E2	$65/2^- \rightarrow 61/2^-$
7→6		464.6	1.15(0.1)			$65/2^- \rightarrow 63/2^-$
7	10220.6	977.2	1.7(0.2)	0.91(0.04)	E2	$69/2^- \rightarrow 65/2^-$
7→6		498.4	1.0(0.1)	0.64(0.05)	M1/E2	$69/2^- \rightarrow 67/2^-$

Table 5.12: Illustrates the measured properties (Relative intensity, Angular-intensity ratios and multipolarity assignment) of the γ-ray transitions in Band 7 of ^{159}Er, * the multipolarity of 1040.9 keV transition assigned acoording to [Del87]

Band	$E_{ex.}$ (keV)	E_γ (keV)	I_γ	R	Multipol.	Transition
7	11264.6	1043.8	1.4(0.2)	0.86(0.04)	E2	$73/2^- \rightarrow 69/2^-$
7→6		532.4	1.1(0.3)			$73/2^- \rightarrow 71/2^-$
7	12373.8	1109.4	1.2(0.2)	0.87(0.03)	E2	$77/2^- \rightarrow 73/2^-$
7	13517.5	1143.6	1.1(0.2)	0.91(0.2)	E2	$81/2^- \rightarrow 77/2^-$
7	13539.4	1165.6	0.8(0.2)			$(81/2^-) \rightarrow 77/2^-$
7	14726.2	1208.7	0.7(0.2)			$(85/2^-) \rightarrow 81/2^-$
7	14744.8	1205.4	0.7(0.2)			$(85/2^-) \rightarrow (81/2^-)$
7	16097.1	(1352.3)	0.6(0.2)			$(89/2^-) \rightarrow (85/2^-)$

Table 5.13: Illustrates the measured properties (Relative intensity, Angular-intensity ratios and multipolarity assignment) of the γ-ray transitions form the decay of states above $69/2^-$ in Band 7 of ^{159}Er.

Thus the excitation energy of band 8 (unfavoured signature) and Band 9 (favoured signature) have been extended down to the energy of 3745-keV and the 3986-keV, with tentative bandhead spins and parity of $(31/2^+)$ and $(33/2^+)$ respectively. In addition, new transitions have been observed at the top of the coupled bands, Band 8 extended up to spin $(73/2^+)$ with two new transitions of 1005-keV and 1015-keV, and the transitions in Band 9 have been established up to spin $(79/2^+)$ with three new transition of 992-keV, 1023-keV and 1069-keV. The spectrum in Figure 5.20 (a) presents transitions in Bands 8 and 9 and is produced with a sum of triple gates set on all crossover transitions from the decay of the $(33/2^+)$ state to $(67/2^+)$ state in coincidence with the 983-keV transition. The electromagnetic character of the majority of transitions in this strongly coupled band has been identified in this work for the first time, from angular intensity-ratio measurements, which is consistent with that of a mixed M1/E2 for Δ I = 1 transitions, and Δ I = 2 in-band transitions have been established as E2 transitions. The transition properties in this pair of strongly coupled bands are given in Tables 5.14 and 5.15.

Band	$E_{ex.}$ (keV)	E_γ (keV)	I_γ	R	Multipol.	Transition
8→9	3986.0	240.9	0.7(0.09)	0.64(0.03)	M1/E2	$(33/2^+) \rightarrow (31/2^+)$
8	4449.0	463.0	0.92(0.1)	0.83(0.01)	E2	$(37/2^+) \rightarrow (33/2^+)$
8→9		203.3	0.88(0.1)	0.57(0.04)	M1/E2	$(37/2^+) \rightarrow (35/2^+)$
8→6		833.9	1.2(0.2)	0.46(0.07)	E1 or M1	$37/2^{(}+) \rightarrow 35/2^-$
8	4889.5	440.6	2.9(0.6)	0.81(0.01)	E2	$(41/2^+) \rightarrow (37/2^+)$
8→9		226.4	2.5(0.1)	0.48(0.02)	M1/E2	$(41/2^+) \rightarrow (39/2^+)$
8	5400.7	511.1	2.1(0.3)			$(45/2^+) \rightarrow (41/2^+)$
8→9		265.1	3.0(0.3)	0.64(0.04)	M1/E2	$(45/2^+) \rightarrow (43/2^+)$
8	6012.3	611.4	1.8(0.3)	0.83(0.03)	E2	$(49/2^+) \rightarrow (45/2^+)$
8→9		317.9	1.6(0.2)	0.62(0.03)	M1/E2	$(49/2^+) \rightarrow (47/2^+)$
8	6721.3	709.6	1.5(0.3)	1.02(0.06)	E2	$(53/2^+) \rightarrow (49/2^+)$
8→9		366.6	1.55(0.2)	0.43(0.03)	M1/E2	$(53/2^+) \rightarrow (51/2^+)$
8	7526.2	804.9	1.4(0.2)	1.03(0.05)	E2	$(57/2^+) \rightarrow (53/2^+)$
8→9		414.0	1.45(0.2)	0.58(0.03)	M1/E2	$(57/2^+) \rightarrow (55/2^+)$
8	8417.5	891.3	1.3(0.3)	0.84(0.07)	E2	$(61/2^+) \rightarrow (57/2^+)$
8→9		455.5	1.2(0.1)			$(61/2^+) \rightarrow (59/2^-)$
8	9381.6	964.1	1.15(0.3)	0.98(0.09)	E2	$(65/2^+) \rightarrow (61/2^+)$
8→9		489.6	1.0(0.2)			$(65/2^+) \rightarrow (63/2^+)$
8	10386.5	1004.9	0.85(0.2)			$(69/2^+) \rightarrow (65/2^+)$
8	11404.2	1014.8	0.72(0.2)	0.96(0.06)	E2	$(73/2^+) \rightarrow (69/2^+)$

Table 5.14: Illustrates the measured properties (Relative intensity, Angular-intensity ratios and multipolarity assignment) of the γ-ray transitions in Band 8 of ^{159}Er.

Band	$E_{ex.}$ (keV)	E_γ (keV)	I_γ	R	Multipol.	Transition
9	4245.6	500.6	1.2(0.2)	0.88(0.02)	E2	$(35/2^+) \rightarrow (31/2^+)$
9→8		259.7	0.6(0.1)			$(35/2^+) \rightarrow (33/2^+)$
9	4663.1	417.5	1.5(0.08)			$(39/2^+) \rightarrow (35/2^+)$
9→8		214.2	1.15(0.1)	0.59(0.05)	M1/E2	$(39/2^+) \rightarrow (37/2^+)$
9→7		(755.4)	0.84(0.2)			$(39/2^+) \rightarrow 37/2^-$
9	5135.6	472.4	2.8(0.3)	0.86(0.02)	E2	$(43/2^+) \rightarrow (39/2^+)$
9→8		246.0	1.9(0.1)	0.45(0.03)	M1/E2	$(43/2^+) \rightarrow (41/2^+)$
9	5694.2	558.6	1.4(0.2)	0.85(0.02)	E2	$(47/2^+) \rightarrow (43/2^+)$
9→8		293.5	1.6(0.1)	0.57(0.02)	M1/E2	$(47/2^+) \rightarrow (45/2^+)$
9	6354.7	660.6	1.4(0.2)	0.90(0.02)	E2	$(51/2^+) \rightarrow (47/2^+)$
9→8		342.7	1.5(0.2)	0.65(0.02)	M1/E2	$(51/2^+) \rightarrow (49/2^+)$
9	7112.2	757.4	1.3(0.1)	0.87(0.05)	E2	$(55/2^+) \rightarrow (55/2^+)$
9→8		390.9	1.4(0.2)	0.48(0.05)	M1/E2	$(55/2^+) \rightarrow (53/2^+)$
9	7961.9	849.7	1.25(0.2)	0.85(0.03)	E2	$(59/2^+) \rightarrow (55/2^+)$
9→8		435.7	2.2(0.2)			$(59/2^+) \rightarrow (57/2^+)$
9	8892.0	930.1	1.2(0.2)	0.85(0.06)	E2	$(63/2^+) \rightarrow (59/2^+)$
9→8		474.5	2.1(0.2)			$(63/2^+ \rightarrow)(61/2^+)$
9	9874.9	982.9	1.1(0.3)	0.84(0.07)	E2	$(67/2^+) \rightarrow (63/2^+)$
9→8		493.3	1.2(0.1)			$(67/2^+) \rightarrow (65/2^+)$
9	19866.9	992.0	0.9(0.2)			$(71/2^+) \rightarrow (67/2^+)$
	11890.0	1023.1	0.76(0.1)			$(75/2^+) \rightarrow (71/2^+)$
	12959.3	1069.3	0.7(0.1)			$(79/2^+) \rightarrow (75/2^+)$

Table 5.15: Illustrates the measured properties (Relative intensity, Angular-intensity ratios and multipolarity assignment) of the γ-ray transitions in Band 9 of ^{159}Er.

Chapter 6

Interpretation of Structure of ^{159}Er

6.1 Introduction

Transitional rare-earth nuclei in mass region ($A \approx 150 - 160$) generate their angular momentum from collective rotation and the alignment of single particle nucleons, especially valence nucleons that are located outside the closed-shell of the doubly magic nucleus $^{146}_{64}\mathrm{Gd}_{82}$. The different bands of the nucleus at low spins are collective rotational structures, as the spin increases pairs of particles align with the rotation and at ultra-high spins the contribution of valence nucleons drives the band to a terminating state, thus the nucleus loses its collectively. To verify this fact, a detailed spectroscopic study has been undertaken of the band structure of the $^{159}_{68}\mathrm{Er}_{91}$ nucleus populated from the fusion evaporation reaction ^{116}Cd(^{48}Ca, 5n) using the Gammasphere array. In order to interpret the experimental results presented in chapter five, Cranked Shell Model calculations have been performed [Naz85, Cwi87], which calculate single particle energies as a function of the deformation parameter and rotational frequency, for both neutrons and protons. The theoretical results have been used to identify the quasiparticles involved in the structure of this nucleus and the interaction between the quasiparticle orbitals that were used to interpert the structure of the different bands. In addition, potential energy surface (PES) [Gne71] and Cranked-Nilsson Strutinsky calculations [Car06, Ben85, Afa99] have been performed to predict

the possible value of spin attained by bands at ultra high spins and to specify the underlying structure.

To understand the nuclear structure properties of $^{159}_{68}\mathrm{Er}_{91}$, the experimental variables will be interpreted in terms of alignment and the rotational properties of the bands in the level schemes shown in previous chapter, see Figures 5.1, 5.2 and 5.16. These can be compared with the theoretical calculation to assign quasi-particle configurations of the bands and specify the underlying structure of the ^{159}Er nucleus.

6.2 Alignment and Rotational Properties of the Bands

Experimentally, the nuclear structure properties of bands can be identified from the alignment $i_x = I_x(\omega) - I_{x,ref}(\omega)$ [Ben79] as a function of rotational frequency, and the excitation energy relative to a rotating liquid drop (rigid rotor reference) based on the Lublin Strasbourg model [Pom83, Car06], as a function of spin (known as rigid rotor plots without contribution of the core nucleons).

I_x is the aligned angular momentum $I_x = \sqrt{I(I+1) - K^2}$, at a given spin and the rotational frequency can be related to the gamma-ray transition energy $\omega \simeq \frac{E_\gamma}{\Delta I_x} \simeq \frac{E_\gamma}{2}$, whereas the rotational and the rigid rotor references are given by

$$I_{x,ref}(\omega) = (J_0 + J_1)\omega - i_0 \tag{6.1}$$

$$E_{RLD}(I) = \frac{\hbar^2}{2\mathcal{J}_{rig}} I(I+1) \tag{6.2}$$

Harris parameters [Har65] $\mathrm{J}_0 = 27.8 MeV^{-1}\hbar^2$ and $\mathrm{J}_1 = 45 MeV^{-3}\hbar^4$ have been used to define contribution of the core so as to reveal quasiparticle characters only. The values are chosen from the mean values for two even-even neighbour isotopes with an offset $i_0 = 0$ to ensure that the alignment for ground state bands of $^{158,\ 160}$Er at low rotational frequencies approximately zero, these values provide constant alignment

for the quasineutron configuration after first backbend. The moment of inertia of the rigid rotor reference is normalised to the ^{158}Er nucleus [Afa99].

$$\frac{\hbar^2}{2\mathcal{J}_{rig}} = 0.007(\frac{158}{A})^{\frac{5}{3}} MeV \tag{6.3}$$

6.3 Cranked Shell Model

To understand the motion of particles in the rotating frame, single particle (quasiparticle) schemes have been produced using Cranked Shell Model calculations. The code uses Universal Woods-Saxon potential, which requires the input of the deformation parameters and nucleon (neutron and proton) number. The prolate shape, $^{159}_{68}Er_{91}$ nucleus has deformations $\beta_2 = 0.235$ and $\beta_4 = 0.046$ [Mol95] with thirteen valence nucleons (9 neutrons and 4 protons) outside the doubly magic $^{146}_{64}$Gd$_{82}$ core. Its Fermi level can be identified from the single particle energy as a function of quadrupole deformation schemes [Ben90], for neutrons, this level is located close to the high-j and low-Ω intruder orbitals at the bottom of the $N_{osc} = 6(\nu\ i_{13/2})$ shell with the second and the third orbitals from the N$_{osc}$ = 5(νh$_{9/2}$, νf$_{7/2}$) subshell. The Fermi level for protons is relevant to high-j orbitals emerging from the middle of the N$_{osc}$ = 5(πh$_{11/2}$) subshell and from the states at the top of the N$_{osc}$ = 4(πd$_{5/2}$, πg$_{7/2}$ and πd$_{3/2}$) subshell with the lowest (πh$_{9/2}$) orbital [Pau09], as displayed in Figure 6.1 (a) and (b). The occupation of the high-j low-Ω i$_{13/2}$ neutron orbitals in this nucleus drives the prolate deformation, giving rise to a dominant collective rotational structure.

Experimentally the $^{159}_{68}$Er$_{91}$ nucleus has a diverse range of band structures collective rotational bands, strongly coupled bands, a gamma-vibration band and strongly deformed band. In order to identify the configuration and the characteristics of these observed bands, Cranked-Shell Model calculation have been performed to calculate quasiparticle energies in the rotating frame (Routhians) as a function of rotational frequency as displayed in Figure 6.2 (a) and (b). The calculation relies on the deformation parameters(β_2, β_4) and energy gap (Δ) of the quasiparticles independent of the rotational frequency. Values of $\Delta = 1.0$ and 1.13 MeV have been used respectively

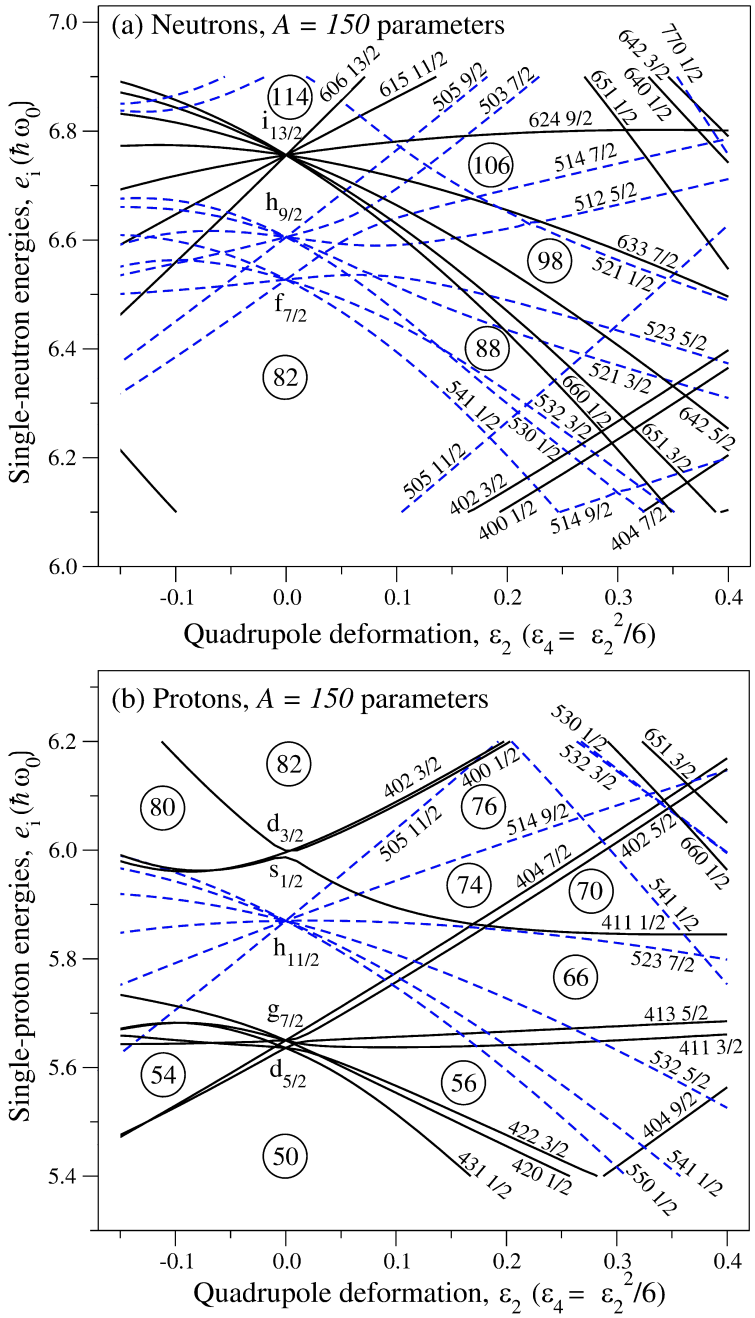

Figure 6.1: Single particle energy a function of quadrupole deformation ε_2 for (a) neutron and (b) protons, calculated with the A = 150 parameters [Ben90]. Positive-parity levels are denoted by solid (black) lines and negative-parity levels by dashed (blue) lines, respectively. The levels are labelled by asymptotic quantum numbers $[Nn_3\lambda]\Omega$. Figure is taken from [Pau09].

to reproduce the value of the neutron and proton crossing frequencies for the yrast band. The quasiparticle levels have been labelled for the orbitals originating from

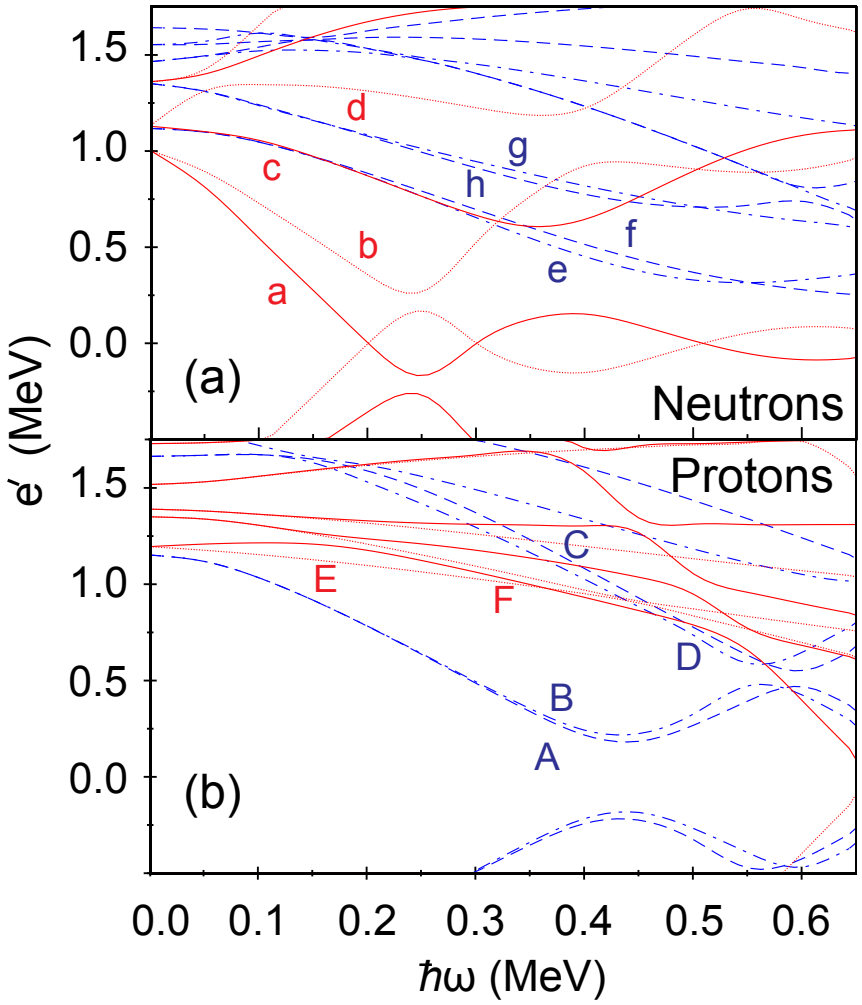

Figure 6.2: Cranked Shell Model calculations for (a) quasi-neutrons (b) quasi-protons in the rotating frame as a function of rotational frequency for ^{159}Er. The deformation parameters used were $\beta_2 = 0.235$, $\beta_4 = 0.046$ and $\gamma = 0°$, and with pair gaps $\Delta_n = 1.0$ MeV and $\Delta_p = 1.13$ MeV. The quasiparticle labeling is given in Table 6.1. The solid lines(red) show levels with parity and signature(π, α) = (+, +1/2); dotted lines (red) show (+, -1/2) levels; dot-dashed lines (blue) show (-, +1/2) and dashed lines (blue) show (-, -1/2) levels.

Nilsson states [N, n_z,Λ]Ω at $\omega = 0$, the levels are labelled in terms of the parity and signature (π, α) of the bands based on the quasiparticle configurations. Table 6.1 explains the quasiparticle labels of the lowest positive- parity and negative-parity orbitals occupied in ^{159}Er, the labelling based on the convention in reference [Rie80].

Quasiparticles	*Label*	$(\pi, \alpha)_n$	*Nilsson orbital*
Neutrons	a	$(+, +1/2)_1$	$i_{13/2}[651]3/2$
	b	$(+, -1/2)_1$	$i_{13/2}[651]3/2$
	c	$(+, +1/2)_2$	$i_{13/2}[660]1/2$
	d	$(+, -1/2)_2$	$i_{13/2}[660]1/2$
	e	$(-, +1/2)_1$	$h_{9/2}[521]3/2$
	f	$(-, -1/2)_1$	$h_{9/2}[521]3/2$
	g	$(-, +1/2)_2$	$f_{7/2}[523]5/2$
	h	$(-, -1/2)_2$	$f_{7/2}[523]5/2$
Protons	A	$(-, -1/2)_1$	$h_{11/2}[523]7/2$
	B	$(-, +1/2)_1$	$h_{11/2}[523]7/2$
	C	$(-, -1/2)_2$	$h_{9/2}[541]1/2$
	D	$(-, +1/2)_2$	$h_{9/2}[541]1/2$
	E	$(+, -1/2)_1$	$g_{7/2}[404]7/2$
	F	$(+, +1/2)_1$	$g_{7/2}[404]7/2$

Table 6.1: Quasiparticle labels for dominant Nilsson states origenated at $\hbar\omega = 0$ in ^{159}Er.

The most probable configurations involved in the structure of the bands in ^{159}Er have been identified from the interaction strength the between the levels which vary with rotational frequency at $\omega \neq 0$, and the alignment plots of the experimental data at the crossing frequencies for typical $i_{13/2}$ neutrons and $h_{11/2}$ protons in Erbium nuclei [Sim98]. Table 6.2 summarises the most probable configurations involved the structure of ^{159}Er.

6.4 Cranked Nilsson-Strutinsky Calculation (CNS)

The behaviour of band structures in nuclei at high-spin (or terminating) states can be interpreted within the framework of the configuration-dependent Cranked Nilsson Strutinsky (CNS) formalism without pairing, described in detail in references

Band	(π, α)	Quasiparticle Configurations
Yrast	$(+, +1/2)$	$a \rightarrow abc \rightarrow abc \otimes AB$
Band 1	$(+, -1/2)$	$b \rightarrow bad \rightarrow bad \otimes ABandEFand/orCD$
Band 2	$(+, -1/2)$	$e \rightarrow eab \rightarrow eab \otimes AB \otimes ubc$
Band 3	$(+, -1/2)$	$f \rightarrow fab \rightarrow fab \otimes AB \otimes ubc$
Band 4	$(+, -1/2)$	$gab \rightarrow gabef \otimes AB$
Band 5	$(+, -1/2)$	$ebc \rightarrow ebc \otimes AB$
γ-Band	$(+, +1/2)$	$\gamma \otimes a \rightarrow \gamma \otimes abc \otimes AB$
Bands 6 and 7	$(+, -1/2)$	$a \otimes AE(F) \rightarrow abc \otimes AE(F) \rightarrow abc \otimes AE(F) \otimes BCandAD$
Bands 8 and 9	$(+, -1/2)$	$eab \otimes AE(F) \rightarrow eab \otimes AE(F)BCandAD$
Band 10	$(+, -1/2)$	$(habef) \rightarrow habef \otimes AB)$

Table 6.2: A summary of the quasiparticle configurations proposed for the bands observed in ^{159}Er.

[Ben85, Afa99, Car06]. This model calculates the potential energy surfaces of nucleus (PES) [Gne71] as a function of angular momentum, for specific neutron and proton configurations outside the core nucleus, in a plane of the quadrupole deformation (ε_2) (defined by the Lund convention [And76]), and triaxial parameter (γ). Furthermore, the excitation energies relative to the rotating liquid drop energy as a function of spin (rigid rotor plots) can be traced for fixed configurations, from the Cranked Nilsson Strutinsky calculation.

For ^{159}Er, the configurations are labelled by the occupation of the valence particles relative to the $^{146}_{64}Gd_{82}$ core, with the shorthand notations$[P_1,P_2,n_1,n_2,n_3]^{\alpha_{tot}}$ for $d_{5/2}$ proton holes, $h_{11/2}$ protons and for the $i_{13/2}$, $h_{9/2}$, and $f_{7/2}$ neutrons respectively. Calculations of the potential energy surface have been carried out at spins $J^\pi = 85/2^+$, $89/2^+$, $97/2^+$, $101/2^+$, $105/2^+$ and $109/2^+$ for high-j $h_{11/2}$ protons and $i_{13/2}$ neutrons of the [4, 3] configurations, with $(\pi, \alpha) = (+, +1/2)$, the results are plotted in Figure 6.3.

The possible theoretical explanation for both signatures of the lowest positive and

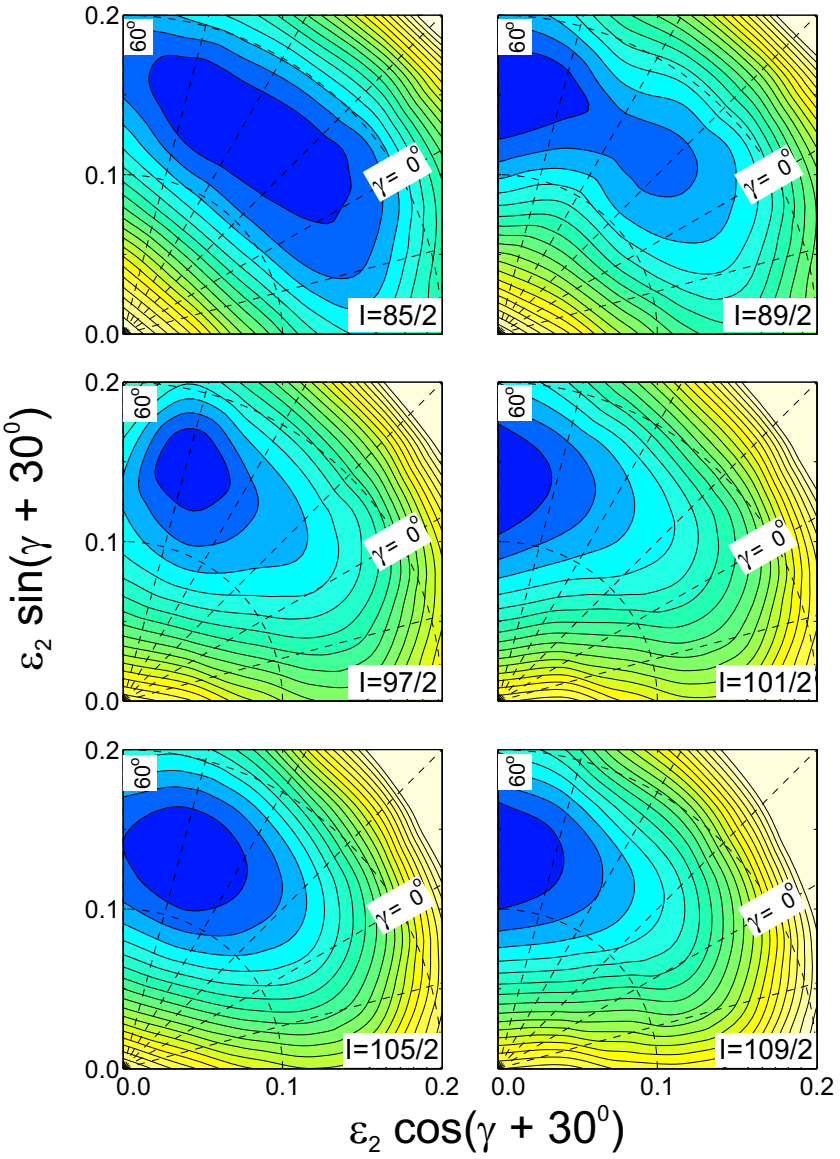

Figure 6.3: Calculated energy as a function of the shape of the nuclear potential. The potential is specified using the quadrupole deformation parameter ε_2 and the triaxiality parameter γ. The energy surfaces are drawn for the (+,+1/2) $\pi(h_{11/2})^4\nu(i_{13/2})^3$ configuration of ^{159}Er at spins 85/2, 89/2, 97/2, 101/2, 105/2 and 109/2. Contour lines are separated by 0.25 MeV and the γ plane is marked at 15° intervals. Dark (blue) regions represent low energy.

negative parity bands (with different configurations) can be obtained from the rigid rotor plots, which are shown in Figure 6.4 (b) and (e). At maximum spin value, the

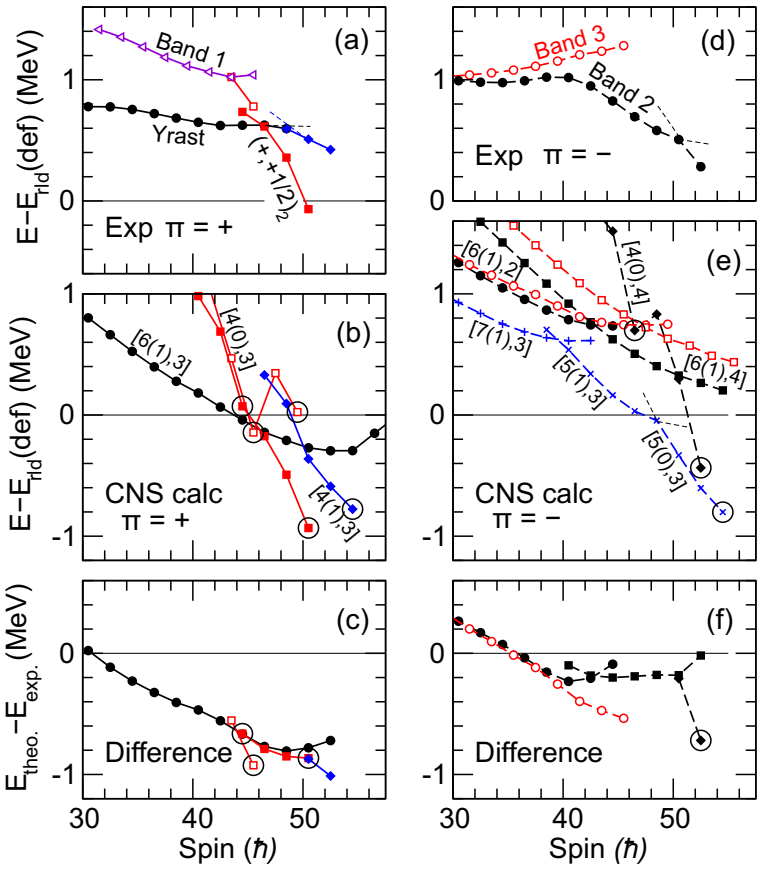

Figure 6.4: Experimental and calculated energies relative to a rotating liquid drop as a function of spin (rigid rotor plots) for the near yrast bands above 30$\hbar$. (a) and (b) positive parity states. (d) and (e) negative parity states. The energy difference between the experimental states and the associated calculated states assigned by theory is presented in (c) and (f) for the positive and negative-parity states respectively, the differences in panel (f) are obtained when the negative parity bands 2 and 3 are compared with configurations which are calculated a few hundred keV above yrast. The calculated configurations are labelled in the standard way by the number of $h_{11/2}$ protons and $i_{13/2}$ neutrons, but in addition by the number of $d_{3/2}s_{1/2}$ protons in parentheses. Positive-parity states are connected by solid lines and negative-parity states are connected by broken lines. Solid symbols correspond to (α = +1/2) and open symbols to (α = -1/2). The aligned states are marked with large open circles and suggested band crossings are indicated by thin dashed lines.

configuration assignments for the observed states of the oblate nuclear shape ($\gamma = 60°$) can be investigated from comparison between the experimental results and the theoretical predictions using Tilted-Fermi-Surface diagrams as depicted in Figure 6.5. The characteristics of the experimentally observed bands in ^{159}Er will be discussed in terms of the possible theoretical predictions and comparisons with the neighbouring nuclei (Erbium isotopes) in the following sections.

6.5 Positive Parity Bands:

This section will discuss the characteristic structure and the configuration assignments for the positive parity bands in ^{159}Er. The signature partner positive parity bands have been extended up to ultra-high spin and the assignment of the newly observed gamma-vibration band provide a complete discussion for a systematic comparison with neighbouring nuclei.

6.5.1 Yrast Band

The yrast band is the favoured signature of the positive parity band (+, + 1/2), based on the occupation of the $i_{13/2}$ odd nucleon in the $[651]3/2^+$ orbital. This was previously assigned in [Sim84], it is labelled (a) in Table 6.1 and Figure 6.2 a. Transitions in the yrast band previously extended up to spin $105/2^+$, there was, also a parallel sequence branching out from the $85/2^+$ yrast state and was labelled as $(+, +1/2)_2$, this extended up to spin $101/2^+$ [Kon99]. The observation of the gamma-ray transitions up to the highest spins $105/2^+$ and $101/2^+$, and the establishment of the multipolarity of linking transitions (1342-keV, 1264-keV and 1304-keV) between states of the yrast band and its high-spin parallel sequence (second $89/2^+$ to $(101/2^+)$), helped to provide a complete discussion for the structure of this band in detail up to the terminating state. Experimental alignment plots of the yrast band and its high-spin parallel sequence labelled $(+, +1/2)_2$ are presented in Figure 6.6, in which, the yrast band has an initial alignment of $\sim 5\hbar$.

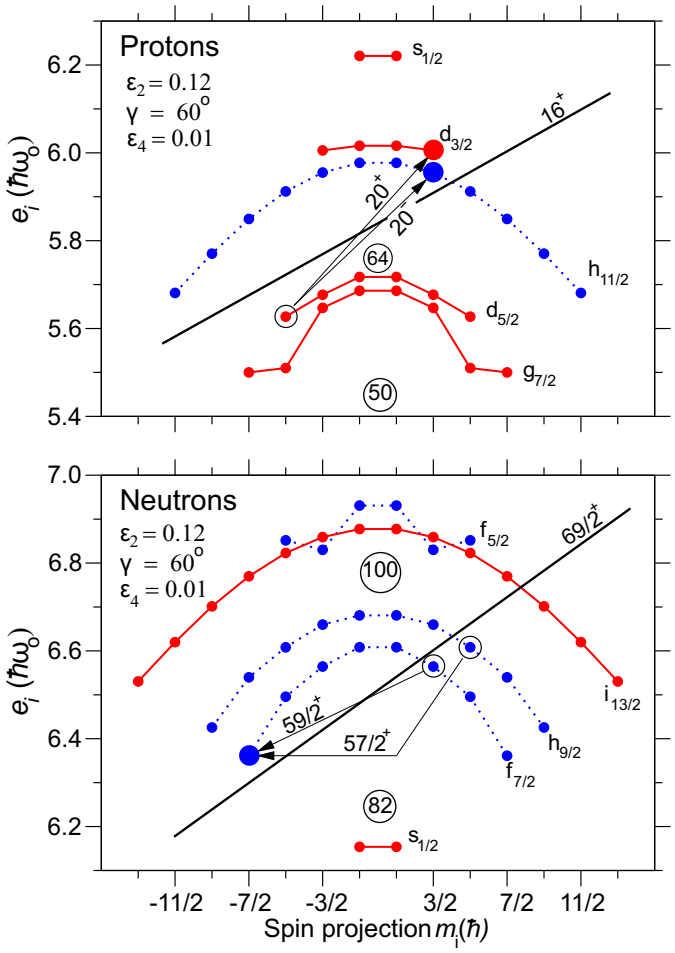

Figure 6.5: Single particle energy of the sloping Fermi surfaces as a function of the projection angular momentum, for protons and neutrons at the deformation specified in the figure, which is typical for the terminating configurations in ^{159}Er. The orbitals are labelled by subshells, but some of these sub-shells are strongly mixed so that, for example, the neutron $h_{9/2}f_{7/2}$ or the proton $g_{7/2}d_{5/2}$ orbitals are treated as one entity. In the fully aligned proton 16^+ state and neutron $69/2^+$ state, all orbitals below the sloping Fermi surfaces drawn by thick lines are occupied. It is then indicated by arrows how favoured lower spin aligned states can be formed if one neutron is de-excited to an anti-aligned orbital and how higher spin favoured states are formed when one proton is excited across the Z = 64 gap. With the present A = 150 parameters [Ben90], the $m = \pm 1/2$ and $m = \pm 3/2$ states of the proton $h_{11/2}$ subshell and those labelled $d_{3/2}$ are very close to degenerate. Therefore, the $d_{3/2}$ states are drawn at a somewhat higher energy to make the figure easier to read.

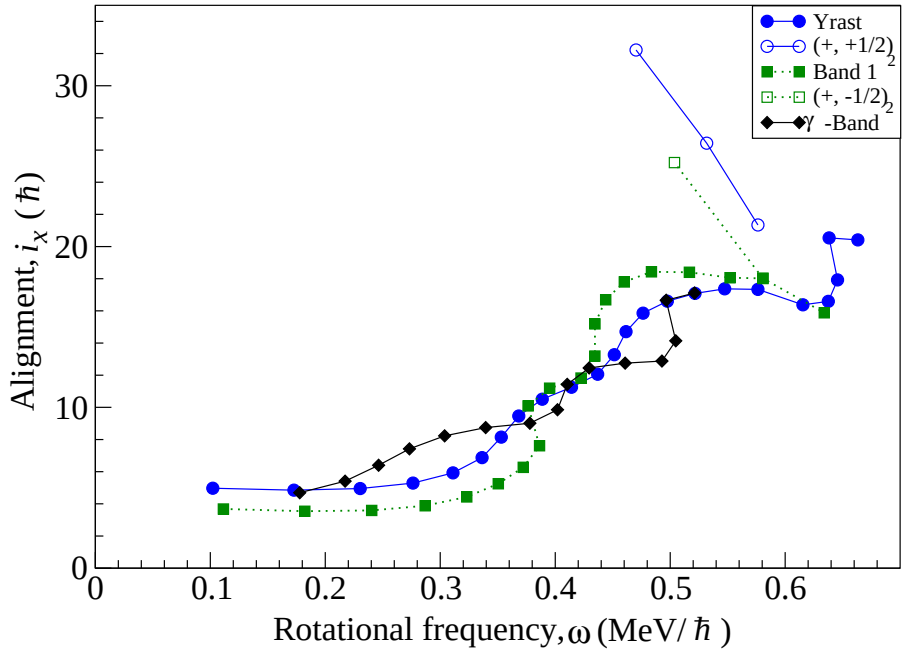

Figure 6.6: The experimental aligned angular momentum (alignment) as a function of rotational frequency for the positive parity bands in ^{159}Er: yrast band and its high-spin parallel sequence labelled $(+, +1/2)_2$, Band 1 and branching above $(87/2^+)$, labelled $(+, -1/2)_2$, and the γ-band. The Harris parameters of $J_0 = 27.8$ MeV^{-1} $\hbar^2$ and $J_1 = 45$ MeV^{-3} $\hbar^4$ have been used.

This reflects its one quasiparticle configuration a at low spin, with the odd neutron in the $[651]3/2^+$ orbital. The predicted alignment of the first pair of $(i_{13/2})^2$ neutrons, the ab crossing at rotational frequency ~ 0.24 MeV/$\hbar$, as shown in Figure 6.2 a, is Pauli blocked. Instead, this band undergoes the gradual alignment ($\sim 6.3\hbar$) of the second pair of $(i_{13/2})^2$ neutrons, labelled bc, at rotational frequency ~ 0.36 MeV/$\hbar$ followed by the alignment ($\sim 5.8\hbar$) of the first pair of $(h_{11/2})^2$ protons, the AB crossing, at rotational frequency ~ 0.46 MeV/$\hbar$. As a consequence of both neutron and proton crossings the band gains an alignment angular momentum of approximately ($\sim 12\hbar$) [Sim87], and its structure changes to a five quasiparticle configuration abc$\otimes$AB as in Table 6.2. Abrupt changes, at higher rotational frequencies, take place within the yrast band, around 0.6 MeV/$\hbar$, as a consequence of a change in the structure to a

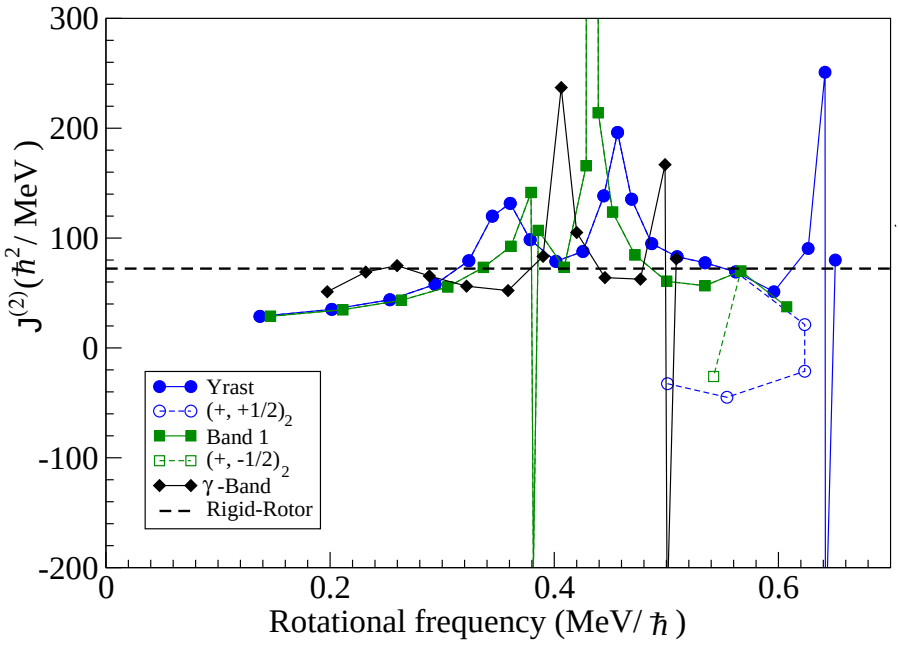

Figure 6.7: Dynamic moment of inertia $\mathcal{J}^{(2)}$ of the experimental data as a function of rotational frequency for the positive parity bands in ^{159}Er compared to the deformed rigid-body rotor $\sim 72\hbar^2$/MeV is shown.

non-collective oblate mode before the band reaches to terminating states. All the above mentioned changes in the structure of this band can be emphasized through the irregular variations of the dynamic moment of inertia relative to the rigid-rotor moment of inertia, as illustrated in Figure 6.7. However, the values of $\mathcal{J}^{(2)}$ in Figure 6.7 for the $(+, +1/2)_2$ decay sequence are lower than the rigid-rotor value, which reveals that the structure becomes yrast quickly when it extends up to the $101/2^+$ state. The experimental rigid-rotor plots in Figure 6.8 clearly show the states at the highest spin values are part of a down sloping sequence and favoured in energy close to or at the terminating states. This behaviour was suggested by Kondev et al. in [Kon99]. The interpretation is that it is similar to the structure of the favoured oblate state configurations in ^{158}Er at $40^+ \Rightarrow [\pi(h_{11/2})^4]_{16^+} \otimes \nu[(i_{13/2})^2(h_{9/2})^2(f_{7/2})^4]_{24^+}$ to $46^+ \Rightarrow [\pi(h_{11/2})^4]_{16^+} \otimes \nu[(i_{13/2})^2(h_{9/2})^3(f_{7/2})^3]_{30^+}$ with alignment of the extra odd neutron residing in the next available orbital $[\nu(i_{13/2})^1]_{9/2}$ in the case of ^{159}Er.

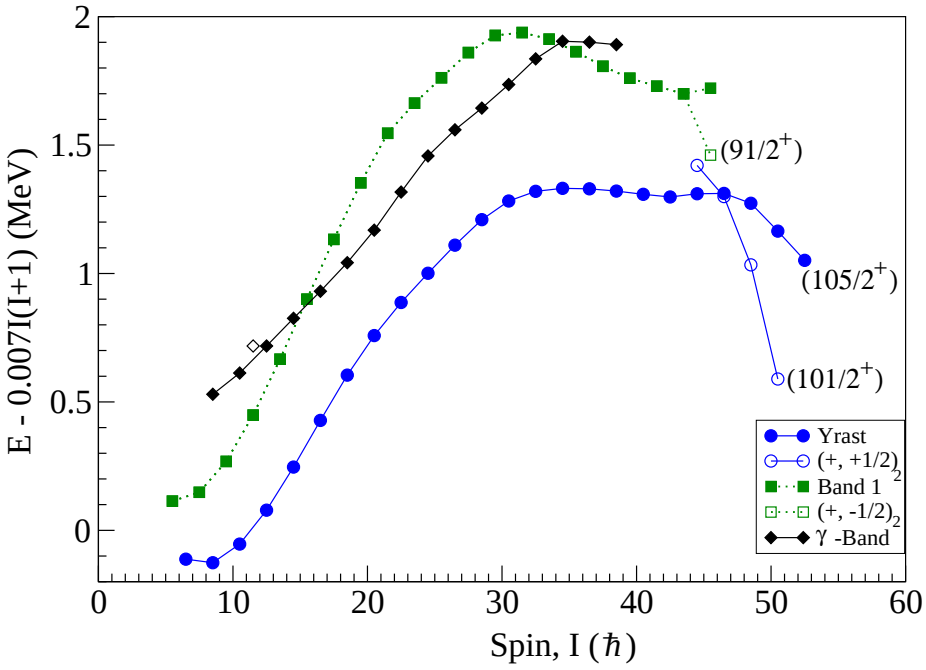

Figure 6.8: Energy relative to a rotating liquid drop (rigid-rotor plot) as a function of spin for the positive parity bands in ^{159}Er: yrast band and its high-spin parallel sequence labelled $(+, +1/2)_2$, Band 1 and branching above $(87/2^+)$, labelled $(+, -1/2)_2$, and the γ-Band. The Harris parameters of $J_0 = 27.8$ MeV^{-1} $\hbar^2$ and $J_1 = 45$ MeV^{-3} $\hbar^4$ have been used.

The behaviour of ^{159}Er, at the highest angular momenta observed in the yrast band, can be interpreted from the results of PES calculations for the chosen configurations $\pi(h_{11/2})^4$ $\nu(i_{13/2})^3$, which are presented in Figure 6.3. The configuration starts out at low spin near $\gamma \sim 0°$, and the minimum energy for spin $85/2^+$ is located at $\gamma \sim 35°$, the state $85/2^+$ appears collective with this configuration. The theoretical predictions for the structure of lower yrast states show that collective behaviour is expected. At higher spins, a well defined minimum with $\gamma = 60°$ (non-collective oblate) is predicted to occur at $89/2^+$, $101/2^+$ and $109/2^+$. The $\gamma = 60°$ minimum energy, at $89/2^+$ and $101/2^+$ corresponds to the structure of the second $89/2^+$ and $101/2^+$ states in the $(+, +1/2)_2$ decay sequence, the latter state was attributed to a fully aligned terminating state determined in reference [Kon99],

which is constructed from full alignment of the spin vectors in the valence configuration $[\pi(\mathrm{h}_{11/2})^4]_{16^+} \otimes \nu[(\mathrm{i}_{13/2})^3(\mathrm{h}_{9/2})^3(\mathrm{f}_{7/2})^3]_{69/2^+}$. Similarly, the former state is constructed with anti-alignment of one spin vector (a pair of $\mathrm{h}_{9/2}$ valence neutrons are anti-aligned), and its configuration will be $[\pi(\mathrm{h}_{11/2})^4]_{16^+} \otimes \nu[(\mathrm{i}_{13/2})^3(\mathrm{h}_{9/2}\mathrm{f}_{7/2})^6]_{57/2^+}$. Moreover, within the constraints of the $\pi(\mathrm{h}_{11/2})^4\ \nu(\mathrm{i}_{13/2})^3$ configuration, the minimum energy has been observed at $109/2^+$ with $\gamma = 60°$. The appearance of this state is a clear indication for states with higher-spins than the $101/2^+$, and existence of a new termination state in the yrast band ($109/2^+$), which has not yet observed experimentally. The formation of states at or near terminating states in ^{159}Er is illustrated in a sloping Fermi surface diagram for protons and neutrons in Figure 6.5. The fully aligned $101/2^+$ state is formed from full alignment of valence protons $[\pi(\mathrm{h}_{11/2})^4]_{16^+}$ and neutrons $\nu[(\mathrm{i}_{13/2})^3(\mathrm{h}_{9/2})^6(\mathrm{f}_{7/2})^6]_{69/2^+}$. Starting from this state, the state $89/2^+$ is formed when one valence neutron de-excites within the $\mathrm{h}_{9/2}\mathrm{f}_{7/2}$ orbital from an $m = 5/2$ state to an $m = -7/2$, illustrated by an arrow in lower panel to form the aligned neutron $57/2^+$ state. Also the new terminating state $109/2^+$ is formed by exciting a proton from below the Z = 64 gap from $m = -5/2$ state in $\mathrm{d}_{5/2}\mathrm{g}_{7/2}$ orbitals to the $m = 3/2$ state in the $\mathrm{d}_{3/2}$ orbital.

The rigid rotor plots of the experimental data, the CNS calculations at different configurations above spin $30\hbar$ for the yrast band and the difference between the calculated and experimental values are presented in the right panels of Figure 6.4 (a), (b) and (c) respectively. The CNS calculation with the $\pi(h_{11/2})^4\nu(i_{13/2})^3$ configuration is consistent with the PES prediction for the terminating states marked with solid square enclosed in open circles for both cases [4(0), 3] and [4(0), 3], and describes the (+, +1/2)$_2$ decay sequence well, with the aligned states at $89/2^+$ and ($101/2^+$) illustrated in Figure 6.3. The most probable configuration to build the (+, +1/2) yrast states for I $\geq 89/2^+$ is $\pi(h_{11/2})^6\ \nu(i_{13/2})^3$ with two additional $\mathrm{h}_{11/2}$ protons. The difference in the slopes between the calculated and experimental rigid rotor plots in Figure 6.4 (c), for spin values I = 30 - $40\hbar$ may be related to the pairing correlations

that are not included in the calculations.

6.5.2 Band 1

Band 1 was established as the unfavoured signature partner (+, -1/2) of the yrast band, based on the odd neutron occupying the next $i_{13/2}$ Nilsson [651]$3/2^+$ state. It lies at excitation energy of 136-keV above the yrast band [Sim84], and is labeled as the b orbital in Table 6.1 and Figure 6.2 a. The analysis in the present work has increased the observed transitions from $43/2^+$ up to $(91/2^+)$. The alignment and the dynamic moment of inertia plots in Figure 6.6 and 6.7 reveal the occurrence of changes in the structural behaviour of this band at rotational frequencies $\sim$ 0.38 MeV/$\hbar$ and $\sim$ 0.44 MeV/$\hbar$ respectively. The interpretation for the structure change at $\sim$ 0.38 MeV/$\hbar$ is attributed to the alignment of the third pair of $(i_{13/2})^2$ neutrons, the (ad) neutron crossing, with gain in alignment of $\sim 7.4\hbar$ relative to its initial alignment of $\sim 3.6\hbar$. This is lower than of the yrast band as expected. The occurrence of the ad neutron crossing was predicted from the Cranked Shell Model calculation at around the same rotational frequency [Sim84]. Figure 6.2 (a) explains the interaction between a and d quasineutron orbitals, which are plotted with dotted lines. A sharp up-bend at rotational frequency $\sim$ 0.44 MeV/$\hbar$ follows the ad neutron crossings. This is a consequence of the alignment the first pair of $(h_{11/2})^2$ protons (AB) with a gain in alignment of $\sim 7.1\hbar$. Thus the structure of the band changes to five quasiparticle configuration bad $\otimes$ AB as given in Table 6.2. At a rotational frequency near to $\sim$ 0.58 MeV/$\hbar$, the structure of band 1 suddenly changes, the $(87/2^+)$ state branches to the two highest observed states $(91/2^+)$, see level scheme in Figure 5.1 or Figures 6.4 (a), 6.6, 6.7 and 6.8. The lower energy observed state $(91/2^+)$ which decays via 1008-keV transition, marked with open square in Figures 6.4(a), 6.6, 6.8 and 6.7, has a behaviour that appears similar to the terminating states in the $(+, +1/2)_2$ decay sequence observed in the yrast band. The formation of the $91/2^+$ terminating state can be explained from the sloping Fermi surface diagrams, see Figure 6.5. Similar to the state $89/2^+$, the lowest-energy

aligned $91/2^+$ state can be constructed when a pair of $f_{7/2}$ valence neutrons are anti-aligned through the de-excitation of one valence neutron within the $h_{9/2}f_{7/2}$ neutron orbitals from an $m = 3/2$ state to an $m = -7/2$ (indicated by an arrow in the lower panel of the Figure 6.5), to form the aligned neutron state $59/2^+$, and suggesting the $[\pi(h_{11/2})^4]_{16^+} \otimes \nu[(i_{13/2})^3(h_{9/2}f_{7/2})^6]_{59/2^+}$ configuration for the $91/2^+$ aligned state. This interpretation is supported by the theoretical prediction of an aligned state 41^+ state, which is constructed from the $[\pi(h_{11/2})^4]_{16^+} \otimes \nu[(i_{13/2})^2(h_{9/2})^3(f_{7/2})^3]_{25^+}$ configuration, the aligned state should be observed in neighbouring nucleus ^{158}Er [Sim94]. However, this state has not yet been observed experimentally. Therefore the lowest-energy $(91/2^+)$ state in band 1 is possible candidate for an aligned oblate state in ^{159}Er, this suggestion is consistent with the results of CNS calculations with a $\pi(h_{11/2})^4$ $\nu(i_{13/2})^3$ configuration, [4(0), 3], as shown in Figure 6.4 (b), the aligned state $(91/2^+)$ is marked with open square enclosed in the large open circle. Furthermore the CNS calculation predict the observation of higher aligned states than the spin $(91/2^+)$ in Band 1.

6.5.3 Gamma-Band

It is possible that the new band observed at an excitation energy of 764-keV higher than that of the yrast band, and connected via a high-energy gamma-ray transition to the yrast band, labelled as Gamma-Band in Figure 5.1, has the same signature and parity as the yrast band (+, +1/2). Thus the possible interpretation for the configuration of this band may be that the band is based on a vibrational excitation coupled to the occupied $i_{13/2}$ neutron a in the $[651]3/2^+$ Nilsson orbital of the yrast band. This suggestion is supported by the angular intensity ratio measurement for most of the decay out transitions to the yrast band. The systematics of the excitation energy for the 2^+ and 4^+ yrast states (the energy and spins of the corresponding yrast 2^+ and 4^+ states for the odd-A erbium isotopes have been plotted relative to the $13/2^+$ yrast state), and the positive parity low lying states for K = 2 gamma-vibrational

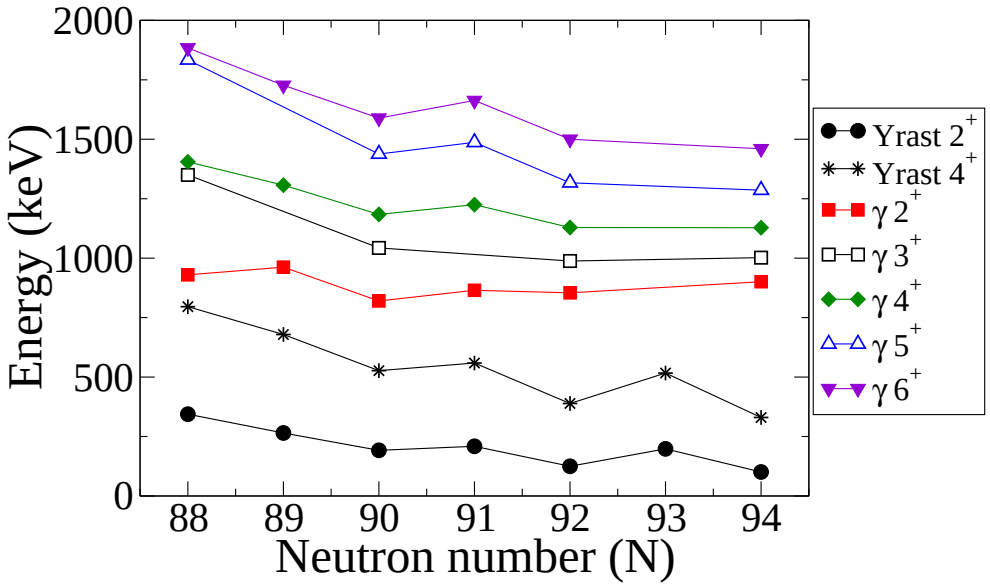

Figure 6.9: Systematics for the 2^+; 3^+; 4^+; 5^+ and 6^+ states of the bands based on γ-vibrational excitations for ^{156}Er [Ree11], ^{157}Er [Gal95], ^{158}Er [Sim84], ^{159}Er, ^{160}Er [Dus06], and ^{162}Er [Jan77]. Also included are the values for the yrast 2^+ and 4^+ states. The energies and spins of the bands observed in the odd-A isotopes are given relative to the lowest-lying state of the yrast band with $13/2^+$.

bands in neighbouring erbium isotopes with N = 88 through to N = 94 are presented in Figure 6.9. This reveals that the level energies for the gamma-band in ^{159}Er show good agreement with the systematics for the corresponding states identified in those neighbouring isotopes. This supports the assignment of this band as gamma-vibrational band. Figures 6.6 and 6.7 show the alignment and dynamic moment of inertia plots respectively, in both plots the nature of this band appear more complex than the other bands. Its structural behaviour in the rotational frequency domain $\sim$ 0.2- 0.35 MeV/$\hbar$ is unclear (upturn with gain in alignment of $\sim 4.2\hbar$), this upturn with increasing rotational frequency is followed by two gains in the aligned angular momentum of $\sim 3.8\hbar$ and $\sim 4.2\hbar$, at $\sim$ 0.41 MeV/$\hbar$ and $\sim$ 0.5 MeV/$\hbar$ crossing frequencies respectively. The crossings are interpreted as delayed (bc) neutron and

(AB) proton crossings, which occur slightly higher than the crossing frequencies in the yrast band because the deformation of the gamma-vibrational band is slightly different from deformation the yrast band.

The energy of the $23/2^{(+)}$ state in ^{159}Er has been plotted in Figure 6.9, with the energies of the $5^{+}{}_{\gamma}$ gamma-vibrational states observed in the even-even neighbouring isotopes, the energy of this state is quite similar to the odd-spin gamma-vibrational states. Therefore a possible candidate for the $5^{+}{}_{\gamma}$ gamma-vibrational state in ^{159}Er is the $23/2^{(+)}$ state. The rigid rotor plot in Figure 6.8 shows the energy of the $23/2^{(+)}$ state, marked with an open diamond, which is associated with the decay out transition of band 7 in the level scheme of Figure 5.16. The energy of this state is tracked on the gamma-vibrational band, see Figure 6.8.

6.6 Negative Parity Bands:

This section is devoted to interpreting the structure of the negative parity bands in ^{159}Er. The extensions of the previously known bands, Bands 2, 3 and 4, and the observation of the new bands, Bands 5 and 10, in the current work, shown in Figure 5.2, allow us to assign configurations to the bands, and also relate the crossing frequencies to the structure of the observed bands according to the predictions of the single-particle model for the unpaired system described in [Ril88] and the CSM calculations.

6.6.1 Band 2

Band 2 ($-$, $+1/2$), has previously been assigned to the occupying of the $h_{9/2}$ Nilsson $[521]3/2^{-}$ orbital by the odd neutron with the (e) configuration according to the CSM calculation [Sim84, Del87]. This band is of the favoured signature and considered as the ground state band in ^{159}Er. The alignment plots in Figure 6.10 show that at low spins this band exhibits collective rotational motion. The band crossing at rotational

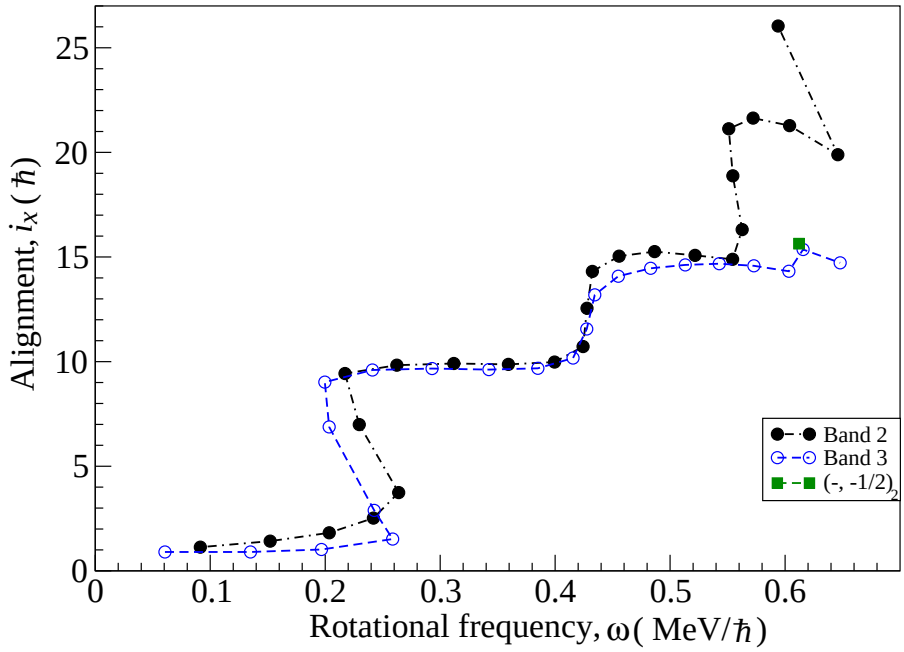

Figure 6.10: The aligned angular momentum (alignment) as a function of rotational frequency for Band 2, Band 3 and its high-spin parallel sequence labeled $(-, -1/2)_2$. The Harris parameters of $J_0 = 27.8$ MeV^{-1} $\hbar^2$ and $J_1 = 45$ MeV^{-3} $\hbar^4$ have been used.

frequency ~ 0.24 MeV/$\hbar$ is followed with a gain in alignment of $\sim 8.4\hbar$. This gain in alignment is consistent with the initial aligned angular momentum of the (a) and (b) quasi-neutrons in the signature partner positive parity bands discussed in section 5.4. Therefore the alignment was attributed to the first pair $(i_{13/2})^2$ neutrons (ab). This alignment resulted from the weak interaction strength between one and three quasiparticle ($e \rightarrow eab$) bands [Sim84, Del87], see Figure 6.2 a. At a rotational frequency of 0.43 MeV/$\hbar$, Band 2 experiences another crossing (up-bend), which causes a gain in alignment of $\sim 5.3\hbar$, as a result of alignment of the first pair of $h_{11/2}$ protons (AB). The AB crossing frequency and gain in the alignment in Band 2 and the yrast band are not of the same value (slightly lower in Band 2), because both bands are based on different deformation and configuration. Band 2 is of the eab $\otimes$ AB configuration, while the yrast band is of the abc $\otimes$ AB configuration. The crossing frequency of the (ab) quasi-neutrons and the (AB) quasi-protons are consistent with

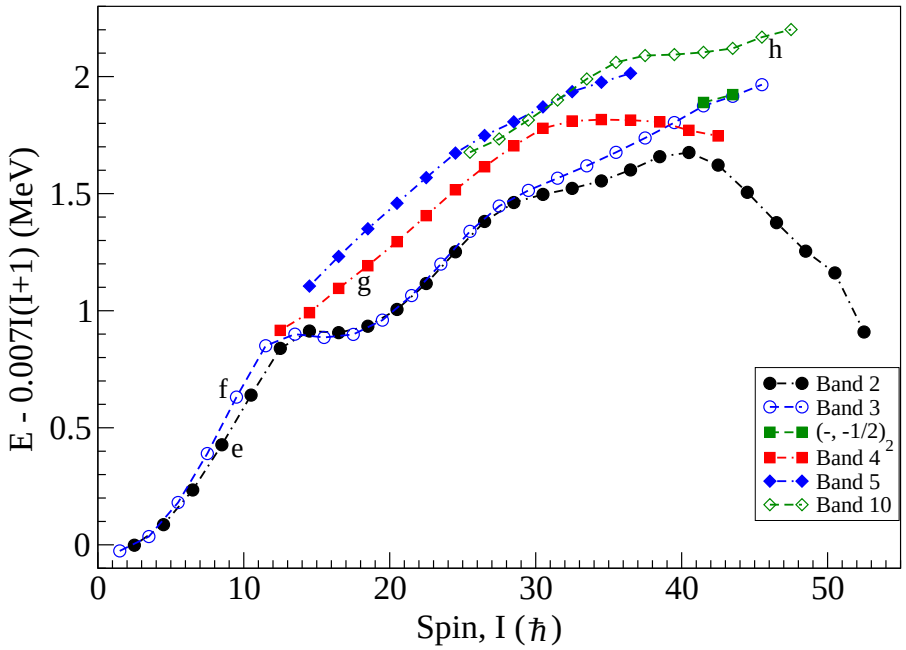

Figure 6.11: Energy relative to a rotating liquid drop (rigid-rotor plot) as a function of spin for the negative parity bands in ^{159}Er: Band 2, Band 3 with its high-spin parallel sequence labelled (-, -1/2)$_2$, Band 4, Band 5 and Band 10.

the predictions of the CSM calculations shown in Figure 6.2 (a) and (b). Furthermore, Band 2 experiences sharp back-bending at a rotational frequency of $\sim$ 0.55 MeV/$\hbar$, with a gain in alignment of $\sim 6.3\hbar$. This anomalous observation is known as an unpaired band crossing, ubc, see table 6.2. The interpretation of this crossing is outlined in a simple single-particle model in [Ril88], explained by Riley et al. For the first time, in an unpaired system the crossing occurs between bands based on specific single neutron configurations, that resulted from an exchange of occupation between a pair of neutrons in the (π, α) = (-, -1/2)$_1$ and (-, +1/2)$_2$ orbitals, and the (π,α) = (+, +1/2)$_1$ and (+, -1/2)$_1$ orbitals.

In Band 2, the highest-spin state observed experimentally is the (105/2$^-$) state, through the observation of a new transition of 1188 keV. The experimental alignment and rigid rotor plots in Figure 6.10 and 6.11, respectively, show that the state (105/2$^-$)

appears not to follow the smooth continuation of Band 2. CNS calculations have been performed to construct the high spin negative parity states in Band 2 (−, +1/2). Configurations with an odd number of $h_{11/2}$ protons and $i_{13/2}$ neutrons were favoured in these calculations, as shown in Figure 6.4 (e) for the configurations labelled with [7(1),3], [5(1),3] and [5(0),3]. The calculation gives a possible explanation for the band crossings observed in Band 2, and also suggests that the lowest energy state $109/2^-$ is a fully aligned terminating state. This lowest-energy aligned state $109/2^-$ can be constructed by exciting a proton below the Z = 64 gap from an $m = -5/2$ state in the $d_{5/2}$ orbital to the $m = 3/2$ state in the $h_{11/2}$ orbital, to form the fully aligned negative-parity state $[\pi(d_{5/2})^{-1}\pi(h_{11/2})^5]_{20^-}$ for the proton configuration, which couples to the $\nu[(i_{13/2})^3(h_{9/2})^3(f_{7/2})^3]_{69/2^+}$ neutron configuration, as illustrated in the top panel of Figure 6.5. In spite of the fact that odd number configurations are lowest in energy and favoured in calculation, as explained in Figure 6.4 (e), they are not assigned to the experimental observed negative parity band, Band 2, because this band is based on the occupation of the $h_{9/2}$ neutrons in the $[521]3/2^-$ negative parity orbital and interpreted at intermediate spin values in the paired regime as having negative parity, according to the discussion above of its alignment properties and comparison with the Cranked Shell Model calculations, see Figure 6.2 (a) and 6.10. Therefore, Band 2 is determined to have an even number of both $h_{11/2}$ protons and $i_{13/2}$ neutrons, and the CNS calculation with two and four $i_{13/2}$ neutrons for the configurations labelled [6(1), 2] and [6(1), 4] in Figure 6.4 (e), produces the observed band crossing at I ≈ 40 $\hbar$. The observation of such a crossing without the contribution of pairing supports the interpretation of the unpaired band crossing described in [Ril88]. Moreover, the calculation with an even $h_{11/2}$ proton configuration, labelled [4(0), 4] and [6(1), 4] in the Figure 6.4 (e), suggest that the discontinuity observed at the highest spin value ($105/2^-$) observed experimentally in this band, corresponds to the full spin alignment $[\pi(h_{11/2})^4]_{16^+} \otimes \nu[(i_{13/2})^4(h_{9/2}f_{7/2})^5]_{73/2^-}$ in the valance space configuration. In the calculations, the relative energies are wrong by approximately 500 keV but this is not unexpected for configurations which differ by a 2p-2h excitation.

6.6.2 Band 3

Band 3 has previously been interpreted as being based on the occupation by the odd neutron of the $h_{9/2}$, $[521]3/2^-$ Nilsson orbital with the (f) configuration [Sim84, Del87]. Assignment of new transitions has led to new states in this band between $15/2^-$ and $27/2^-$ in the present work, see Figure 5.2, that provide further evidence for the interpretation of this band as the negative (-, -1/2)$_1$ signature partner of Band 2. The alignment plots in Figure 6.10, and discontinuities in the dynamic moment inertia relative to of the rigid body moment of inertia for ^{159}Er nucleus, as shown in Figure 6.12, show that the structure of this band is similar to the Band 2. The band undergoes the (ab) $(i_{13/2})^2$ neutron crossing at rotational frequency $\sim$ 0.24 MeV/$\hbar$, with an alignment gain of $\sim 8.6\hbar$, which is followed by the alignment of the first pair $(h_{11/2})^2$ protons (AB) at a rotational frequency of the $\sim$ 0.43 MeV/$\hbar$, with a $\sim 5.0\hbar$ gain in the aligned angular momentum. Also the new high-spin transitions observed at the top of this band indicate a branching in the (-, -1/2)$_2$ sequence at the $79/2^-$ state at a rotational frequency of $\sim$ 0.6 MeV/$\hbar$. The new $(83/2^-)$ and $(87/2^-)$ states have very similar energies to the corresponding states in Band 3, as presented in Figure 5.2. The rotational properties of these states in Figures 6.10, 6.11 and 6.12 are labelled with green solid squares. The large discontinuity in dynamic moment of inertia of this (-, -1/2)$_2$ branch at $\sim$ 0.6 MeV/$\hbar$, as shown in Figure 6.12, may indicate the crossing that was predicted by Riley et al. [Ril88] for Band 3, which is interpreted as an exchange of a pair of neutrons from the (π, α) = (-, -1/2)$_2$ and (-, +1/2)$_1$ orbitals, with the (π, α) = (+, +1/2)$_1$ and (+, -1/2)$_1$ orbitals. The CNS calculation with two and four $i_{13/2}$ neutrons configurations, labelled [6(1), 2] and [6(1), 4] in Figure 6.4 (e) predict a delayed crossing between the configurations in this branch, but at a spin value which roughly coincides with the highest observed spin in Band 3. This suggests that Band 3 needs to be observed to higher spin values to test these predictions. This interpretation is supported with experimental observations for Band 3, which does not appear to terminate at the highest observed spin values, as shown in Figure 6.11.

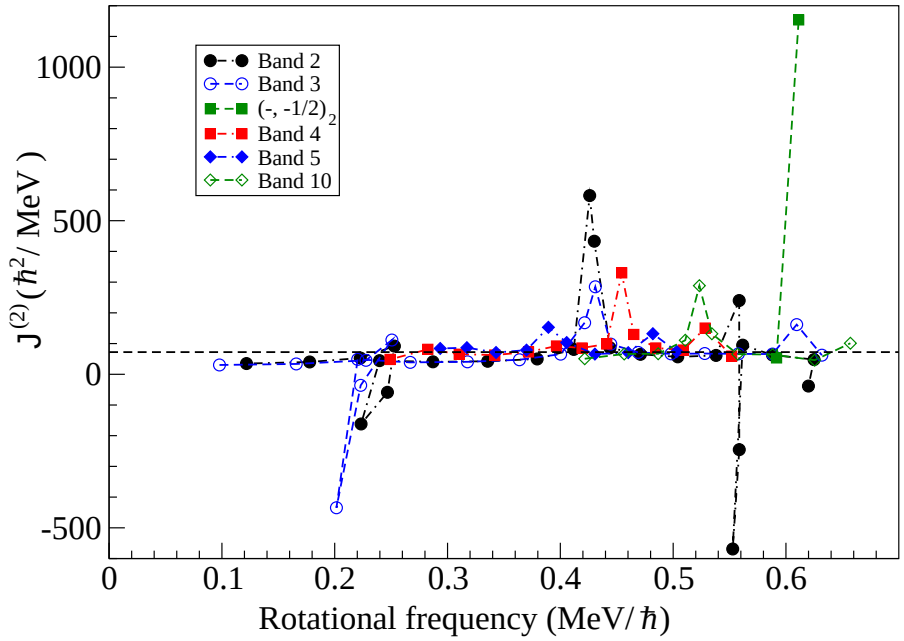

Figure 6.12: Dynamic moment of inertia $\mathcal{J}^{(2)}$ of the experimental data as a function of rotational frequency for the negative parity bands in ^{159}Er: Band 2, Band 3 with its high-spin parallel sequence labelled (-, -1/2)$_2$, Band 4, Band 5 and Band 10.

6.6.3 Band 4

Band 4 has the same signature and parity as Band 2, and depopulates strongly through the 640-keV and 540-keV to Band 1 and Band 2 at levels $23/2^+$ and $25/2^-$ respectively. This band has previously been assigned in terms of the next higher-lying negative-parity positive-signature quasineutron configuration (g) originating from the $h_{9/2}$ $[523]5/2^-$ Nilsson orbital [Del87]. The initial alignment of $\sim 6.9\hbar$ at rotational frequency ~ 0.24 MeV/$\hbar$ in Figure 6.13 suggests the configuration (gab) for Band 4. The gain in alignment of this band appears to be increasing gradually with increasing rotational frequency, and then experiences a band crossing at distinct rotational frequency ~ 0.46 MeV/$\hbar$, which is higher than of the second crossings in Bands 2 and 3 (based on the (e) and (f) configurations at low rotational frequencies, respectively). On the other hand, its alignment is $\sim 2\hbar$ higher than that of Band 2 and 3. A possible

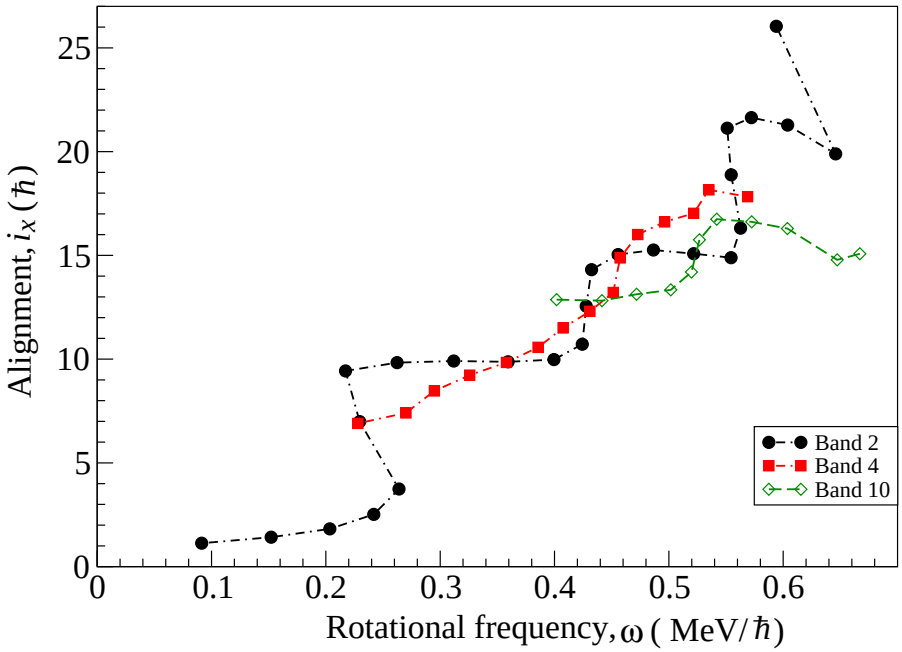

Figure 6.13: The aligned angular momentum (alignment) as a function of rotational frequency for Band 2, Band 4 and Band 10.

reason for this may lie with the $(f_{7/2}h_{9/2})^2$ (ef) crossing occurring at roughly the same rotational frequency as the (AB) crossing, and the structure of the band changes to seven quasiparticle configurations gab$\rightarrow$ gabef $\otimes$ AB as explained in table 6.2.

6.6.4 Band 5

The first four transitions in Band 5 have previously been observed [Del87], see Figure 5.2. In the present work, using the triple (double) gate coincidence techniques this new band has been tentatively extended up to state $(73/2^-)$ and its band head is now assigned to a $29/2^-$ state, and linked with the Band 2 through the new 654 keV E2 transition. The negative-parity positive-signature nature of this new band suggests that its structure is either based on the next higher-lying configuration (h), or, that it is a continuation of Band 2, based on the (e) configuration beyond the (ab) crossing. The later interpretation was speculatively suggested by Deleplaque et al. [Del87].

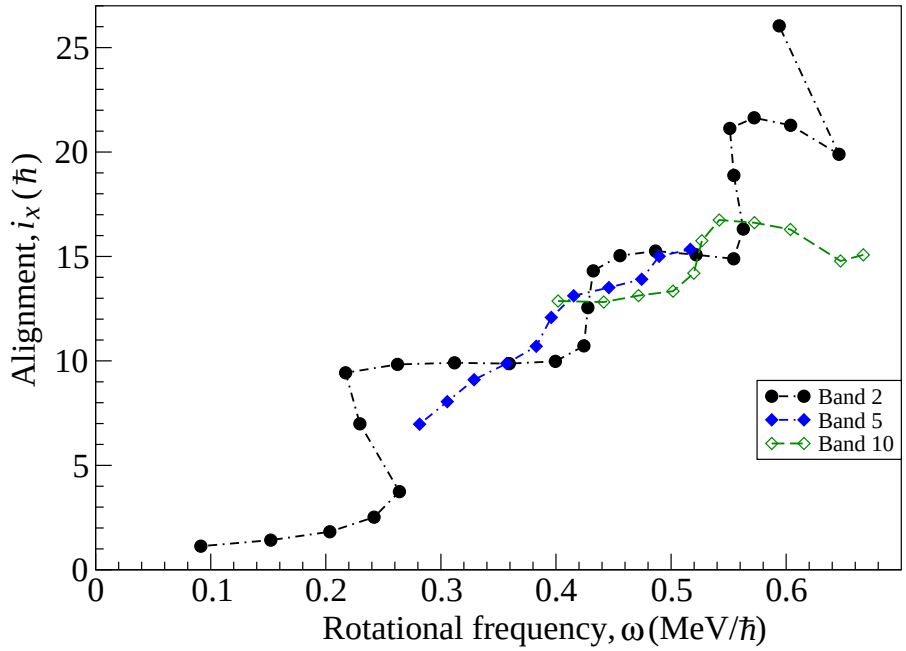

Figure 6.14: The aligned angular momentum (alignment) as a function of rotational frequency for Band 2, Band 5 and Band 10. The Harris parameters of $J_0 = 27.8$ MeV^{-1} $\hbar^2$ and $J_1 = 45$ MeV^{-3} $\hbar^4$ have been used.

The alignment characteristics of Band 5 lend weight to this assignment, with the initial alignment of $\sim 7.0\hbar$ suggesting a smooth continuation of the (e) configuration, which possibly undergoes a second $(i_{13/2})^2$ neutron alignment (bc) at rotational frequency ~ 0.27 MeV/$\hbar$, see Figure 6.14. The gain in alignment at rotational frequency ~ 0.4 MeV/$\hbar$ in Band 5 is $\sim 2\hbar$ lower than that of Band 2, and may be attributed to the AB $(h_{11/2})^2$ proton crossing, which will occur at a lower rotational frequency for this band because it lies higher in excitation energy than Band 2 and the other negative-parity bands.

6.6.5 Band 10

In the present work, a new band (Band 10) of low intensity gamma-ray transitions has been observed, which feeds into the moderate-spin ($49/2^+$, $53/2^+$) and ($51/2^-$, $55/2^-$) states of the yrast band and Band 3 respectively. Band 10, has been deduced to be of a negative-parity and negative-signature nature, through assignment of electromagnetic character of the 1143-keV linking transition to Band 3, as an E2 transition. This assignment would suggest that Band 10 is the signature partner of either Band 4 or Band 5. The alignment plots of Figure 6.13 and 6.14 do not give a clear indication as to which interpretation is most likely, however, Figure 6.11 show that Band 4 lies at a lower excitation energy than Band 5, and, therefore, Band 10 may be the unfavored signature partner of Band 4. Band 10 has an initial alignment of $\sim 13\hbar$, which is higher than the initial alignments of all the observed bands in ^{159}Er. This suggests that Band 10, is based on at least a three- or five-quasiparticle configuration. If structure of Band 10 is considered as the unfavored signature of Band 4, then its initial alignment may be attributed to the (habef) configuration. The Figures 6.12, 6.13 and 6.14 show that this aligned structure experiences a further quasiparticle alignment at a rotational frequency of ~ 0.53 MeV/$\hbar$ with a gain in alignment of $\sim 3.7\hbar$. This crossing may be attributed either to a delayed crossing of the ($h_{11/2}$) proton pair (AB) or to the unpaired band crossing involving exchange a pair of neutrons between positive-parity and negative-parity signature partner bands, as discussed in section 6.6.1 and 6.6.2. However, in the absence of the low-spin structure of this band, these interpretations are speculative.

6.7 Strongly Coupled Structure Bands:

The structure of the strongly coupled signature-partner Bands (6 & 7) and (8 & 9) observed in ^{159}Er, has previously been discussed in [Sim98]. The proposed configuration of the coupled structures was based on several experimental observations: absence of the occurrence of the AB $(h_{11/2})^2$ proton crossing in the coupled structures,

similarity in the intensity of different multiple character gamma-ray transitions at the bottom of the bands, the dipole nature of the assigned (806-keV, 1072-keV and 1270-keV) and non-assigned (1445-keV and 1795-keV) decay-out transitions from Bands 6 and 7 to the low-K yrast structures, and hindered decays from Bands 8 and 9 to the low-K yrast structures. These all indicate that the coupled bands are constructed at high-K values and are based on the excitation of multi-quasiparticles involving the $h_{11/2}[523]7/2$ and and $g_{9/2}[404]7/2$ proton configurations coupled to the odd neutron, see table 6.2. The quasiparticle assignments have been strengthened by the experimentally measured reduced transition probabilities $\frac{B(M1)}{B(E2)}$ in the strongly coupled bands, extracted from branching ratios of the ΔI = 1 and Δ I = 2 competing gamma-ray transitions measured by putting a double (triple) coincidence gate on the transition (transitions) above each level of interest and using the following equation:

$$\frac{B(M1;I\rightarrow I-1)}{B(E2;I\rightarrow I-2)} = 0.697\frac{(E_\gamma)^5(I\rightarrow I-2)}{(E_\gamma)^3(I\rightarrow I-1)} \times \frac{1}{\lambda_\gamma(1+\delta^2)}\ (\mu_N/eb)^2 \tag{6.4}$$

where E_γ is the energy of the gamma-ray transition measured in MeV, λ_γ is the branching ratio defined as the intensity ratio $\lambda_\gamma = \frac{I_\gamma(I\rightarrow I-2)}{I_\gamma(I\rightarrow I-1)}$ of the ΔI = 1 and ΔI = 2 competing gamma-ray transitions measured by putting a triple (double) coincidence gate on the transition above each level of interest, and the multipole mixing ratios δ(E2/M1) is assumed zero.

The experimental results for the reduced transition probability ratios were compared with the theoretical predictions of the semi-classical model of Dönau and Frauendorf [Don87] and [Fra81]. The parameters summarised in Table 6.3 were used in the calculation for quasiparticles which are associated with the configurations of the coupled bands. The experimental and the calculated results for B(M1)/B(E2) ratio are presented in Figure 6.15. As can be seen from Figure 6.15 the calculated values from proposed configurations are expected to be consistent to some extent with the experimental data, and support the assignment of the configurations. The structure of the strongly coupled bands in ^{159}Er was interpreted previously by Simpson et al. [Sim98].

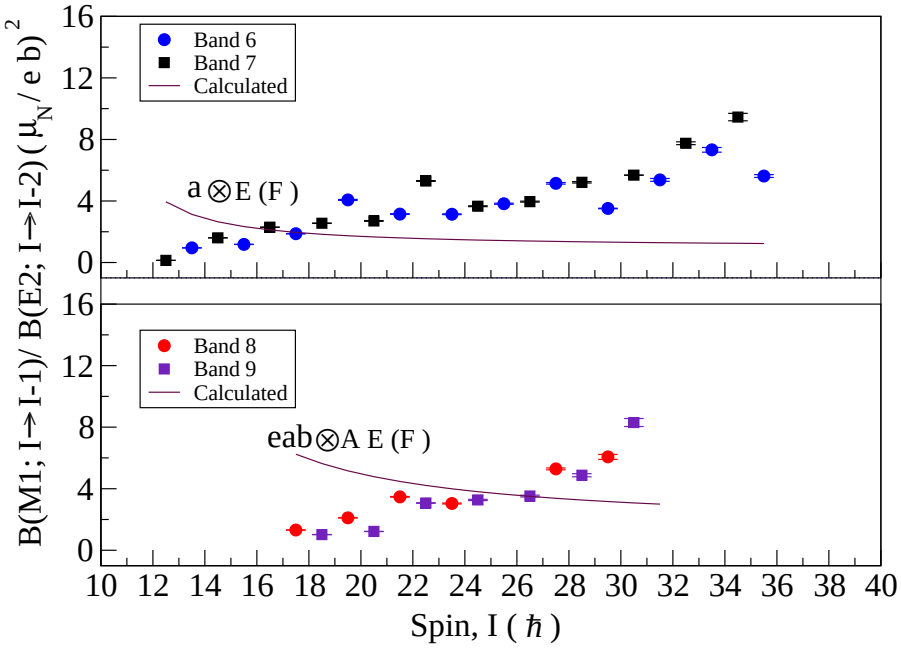

Figure 6.15: Measured reduced transition probability ratios B(M1)/B(E2) for the strongly coupled bands in ^{159}Er, with theoretical calculations using the parameters illustrated in Tables 6.3 for the given configurations.

Protons				Neutrons			
Nilsson State	g_Ω	i	Ω^π	Nilsson State	g_Ω	i	Ω^π
$g_{7/2}[404]7/2^+$	0.739	0.5	$7/2^+$	$i_{13/2}[651]3/2^+$	-0.177	5.015	$3/2^+$
$h_{11/2}[523]7/2^-$	1.214	2.3	$7/2^-$	$h_{9/2}[521]3/2^-$	0.209	1.446	$3/2^-$
				$(i_{13/2})^2[651]3/2^+$	-0.26	8.780	0

Table 6.3: The parameters were used in B(M1)/B(E2) calculation for the coupled bands in ^{159}Er.

In the next two subsections 6.7.1 and 6.7.2, the configurations and changes in the structure of the strongly coupled bands in the present experimental data will be interpreted in terms of the aligned angular momentum and dynamic moment of inertia relative to of the rigid body rotor with rotational frequency, as shown in Figures 6.16 and 6.17 respectively.

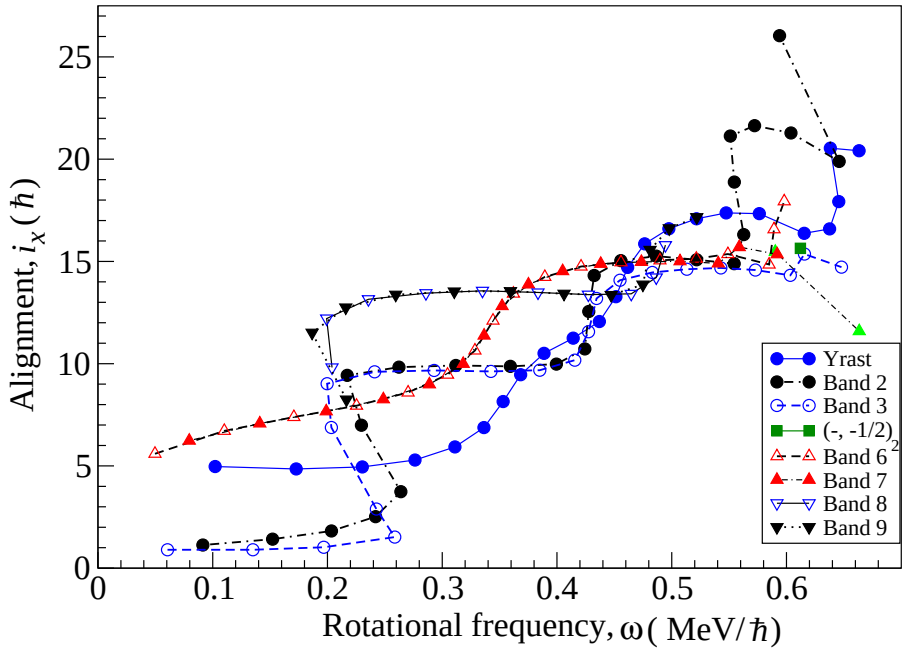

Figure 6.16: The aligned angular momentum (alignment) as a function of rotational frequency for the strongly coupled bands in ^{159}Er, with yrast band and Bands 2 and 3 with its high-spin parallel sequence labelled (-, -1/2)$_2$. The Harris parameters of J_0 = 27.8 MeV^{-1} $\hbar^2$ and J_1 = 45 MeV^{-3} $\hbar^4$ have been used.

6.7.1 Bands 6 and 7

The configuration of Bands 6 and 7 at low rotational frequency has previously been assigned to the $h_{11/2}[523]7/2$ and $g_{7/2}[404]7/2$ protons coupled to the $i_{13/2}[651]3/2$ neutron, a $\otimes$ AE(F) configurations. In this strongly coupled structure, the initial alignment in Band 6 is $\sim 5.7\hbar$ and in Band 7 is $\sim 6.2\hbar$. The gradual increase of alignment with rotational frequency and the $\sim 9.5\hbar$ and $\sim 8.7\hbar$ gain in alignment at rotational frequency $\sim$ 0.344 MeV/$\hbar$ and $\sim$ 0.352 MeV/$\hbar$ was attributed to the alignment of the $(i_{13/2})^2$ neutron pair (bc) crossing for both bands, see Figure 6.16, which illustrates the alignment of the strongly coupled bands and the bands based on the quasineutrons contributing to the configuration of the strongly coupled bands. In the present work, as a consequence of the observation of new transitions in this

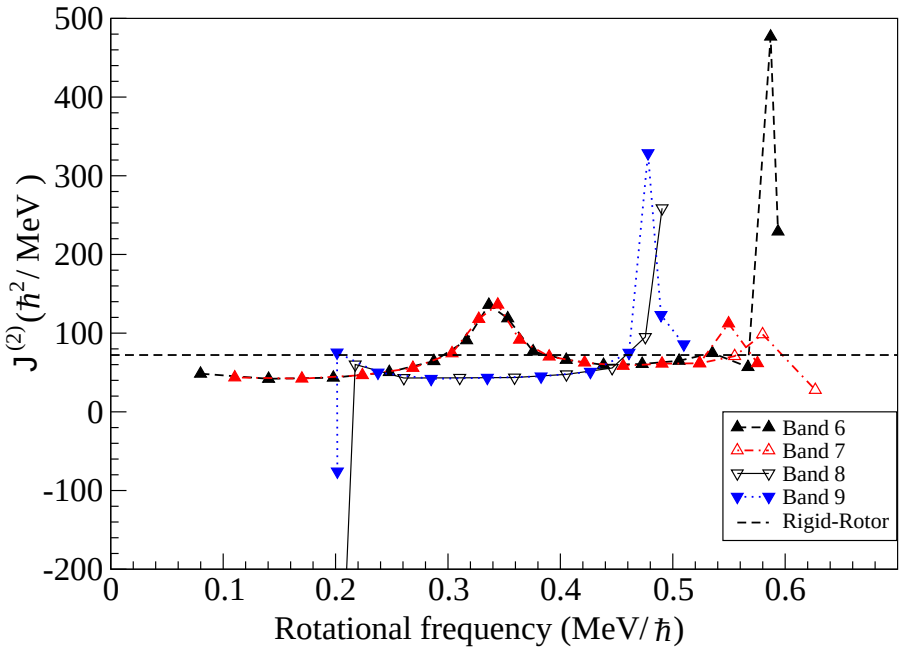

Figure 6.17: Dynamic moment of inertia $\mathcal{J}^{(2)}$ of the experimental data as a function of rotational frequency for the strongly coupled bands in ^{159}Er.

coupled bands, Bands 6 and 7 have been extended up to spins $(91/2^-)$ and $(85/2^-)$, and an additional parallel sequence branching off from the $77/2^-$ state in Band 7 has been observed up to spin $(89/2^-)$. At high rotational frequency ~ 0.59 MeV/$\hbar$ Band 6 experiences a sharp up-bend and gain in alignment, and at a slightly lower frequency the alignment in Band 7 becomes irregular and the parallel branch is observed at the same rotational frequency ($\sim$ 0.59 MeV/$\hbar$), see Figure 6.16. The change in band structure at this rotational frequency is attributed to the alignment of a second and third pair of protons, at the BC and AD proton crossings respectively. These crossings are predicted to occur around this rotational frequency in CSM calculations for quasiprotons, see Figure 6.2 b, and may be cause of these observations. Also, all the changes in the structure are illustrated in Figure 6.17, through the discontinuity of the dynamic moment of inertia of the strongly coupled bands relative to the rigid-body rotor.

6.7.2 Bands 8 and 9

The strongly coupled Bands 8 and 9 have previously been discussed in terms of the AE(F) proton configurations coupled to the odd neutron residing in the $h_{9/2}[521]3/2^-$ Nilsson state (e). Thus these coupled signature partner bands were assigned a positive parity [Sim98]. The spin assignments deduced for these bands suggested that an initial configuration of eab $\otimes$ AE(F) is appropriate for a high initial alignment of $\sim 10\hbar$, see Figure 5a in the previous work [Sim98]. From the present work, assignment of a dipole character to the new connecting transition between Bands 8 and 6 of gamma-ray energy 834-keV, confirm the previous spin assignments. Also through the newly observed transitions at low spins, the bandheads of Bands 8 and 9 are assigned $(33/2^+)$ and $(31/2^+)$, respectively, and a sharp gain in alignment observed at rotational frequency ~ 0.22 MeV/$\hbar$ in both bands suggests the presence of the (ab) crossing, which confirms the previous configuration assignments, see Figures 6.16 and 6.17. At high spins, an additional two and three new transitions have been observed in the Bands 8 and 9 respectively. With these extensions the bands show gain in alignment at crossing frequency of ~ 0.48 MeV/$\hbar$, see the same Figures. The first proton crossing (AB) is expected to be blocked in Bands 8 and 9 similar to the Bands 6 and 7, because of the presence of (A) quasiproton in the configuration of these bands. Therefore, these alignment gains could correspond to the BC and AD proton crossings. However, the crossings in Bands 8 and 9 occur at lower rotational frequency than the second and third proton crossings in Bands 6 and 7, and that predicted by the CSM calculations as in Figure 6.2 b, which may be an indication that these configurations have different deformations. It is interesting to note the unpaired band crossings occur at this frequency region in the negative parity signature partner Bands 2 and 3, see discussion in sections 6.6.1 and 6.6.2. Since the neutron configuration of Band 2 is contributes to the structure these strongly coupled bands, the unpaired crossing may well be expected Bands 8 and 9.

6.8 Triaxially Strongly Deformed Band:

Two weakly populated rotational bands with high dynamic moments of inertia have been previously observed in each of ^{157}Er and ^{158}Er. The bands bypass the terminating states [Pau07], the interpretation for the structure of these bands was based on Cranked Nilsson-Strutinsky Calculations, and the bands interpreted as triaxial strongly deformed structures (TSD) with $\varepsilon_2 = 0.37$ and $\gamma = 25^\circ$ [Ril09]. In the present experiment, three weeakly populated collective bands in ^{160}Er [Oll09, Oll11] and one band in ^{159}Er [Oll09] were observed, with the same characteristic of the TSD bands in ^{157,158}Er isotopes. The structure of the bands in ^{159}Er and ^{160}Er have been compared with CNS calculation and interpreted as triaxial strongly deformed (TSD) structures at $\varepsilon_2 = 0.37$ and $\gamma \sim \pm\, 20^\circ$ [Oll09], the detail of interpretation is discribed in reference [Oll09]. The observed triaxial band in ^{159}Er is labelld TSD1 in Figure 5.2. The excitation energy of this band, and tentative spin values are based on comparisions with CNS calculation [Oll09], also the in-band transitions were assumed as of stretched E2 character. The dynamic moment of inertia ($\mathcal{J}^{(2)}$) of the TSD bands in ^{157,158,160}Er was extracted under similar assumptions. The $\mathcal{J}^{(2)}$ for TSD1 in ^{159}Er is plotted with of all the TSD bands in ^{157,158}Er and ^{160}Er as a function of rotational frequency in Figures 6.18 (a) and (b) repectevily. The experimental data of dynamic moments of inertia ($\mathcal{J}^{(2)}$) in all TSD bands decrease with increasing rotational frequency, and TSD1 band in ^{159}Er similar to the TSD bands in ^{160}Er and TSD2 band in ^{158}Er exhibit a rise in $\mathcal{J}^{(2)}$ at a rotational frequency of ~ 0.55 MeV/$\hbar$. Theoretical calculations with a positive-γ configuration predict the occurence this bump in $\mathcal{J}^{(2)}$ as a consequence of alignment of $i_{13/2}$ neutrons at slightly lower rotational frequency than the experiment in ^{159}Er, on the other hand the calculation with negative-γ configuration attributes the observed bump in the dynamic moment of inertia of the experimental data, to proton crossing involving the $N_{osc} = 5$ $h_{11/2}$ and $h_{9/2}f_{7/2}$ proton orbitals, at $\sim$ 0.4- 0.5 MeV/$\hbar$ [Oll09]. Recent lifetime mearsurments of the TSD bands in ^{157,158}Er [Wan11] confirm that these bands are indeed strongly deformed.

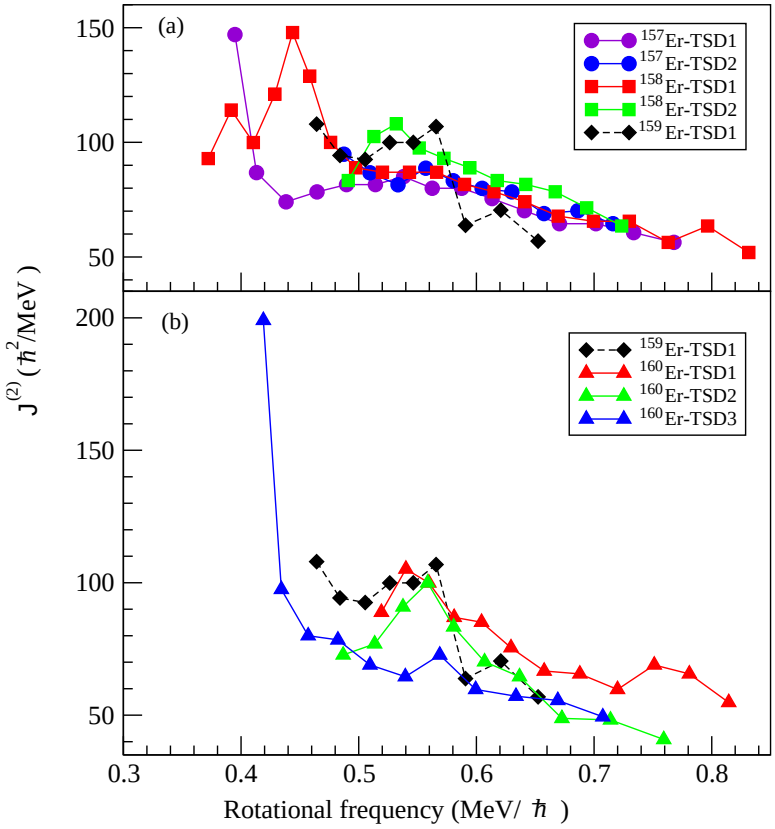

Figure 6.18: The dynamic moment of inertioa $\mathcal{J}^{(2)}$ as a function of rotational frequency for the triaxial band in ^{159}Er (a) with the proposed TSD bands in ^{157,158}Er and (b) with the proposed TSD bands in ^{160}Er isotopes.

However, the experimentally extracted transition quadrupole moment Q_t values are not consistent with the calculated favoured triaxial minimum of the positive-γ deformation by CNS calculations. In fact, a more deformed positive-γ or a negative-γ deformation gives better agreement. These recent experimental results highlight a challenge for the understanding of the triaxial degree of freedom and suggest that other theoretical approaches may need to be explored [Wan11]. Indeed, tilted cranking models suggest that the rotational axis can lie between the intermediate and

short principal axes. Thus, a rotational band may be associated with a mixing of the positive- and negative-gamma minima and recent calculations by Shi et al., [Shi12] discuss this issue and the structures responsible for the re-emergence of collectivity at such high spin values (I = 50-60$\hbar$).

6.9 Conclusion

A detailed spectroscopic study for the gamma-decays from excited states of ^{159}Er has been performed to understand the structural changes that occur with increasing angular momentum and excitation energy. The current work has revealed, three new rotational bands (γ-Band, Band 5 and Band 10), and extensions up to highest possible spins are made to the previously reported bands in ^{159}Er [Del87, Sim98]. Furthermore extensions at low spin are made to fill a gap of 6$\hbar$ in Band 3 with three new transitions and to extend down the band-head spin of the strongly coupled Bands 8 and 9 by 2$\hbar$. Assignments of band-head excitation energy and spin for the new bands, Band 4 and strongly coupled Bands 8 and 9 have been performed from angular intensity ratio measurements for newly observed linking transitions. The band structures are based on specific quasiparticle configurations discussed within the framework of the CSM. In addition, a new γ-Band may be based on the γ-vibrational structure coupled to the $i_{13/2}$ yrast band. At the highest possible observed spins, $\sim$ 50$\hbar$, there is a strong evidence for the structure of the positive parity bands, yrast band and Band 1, and the negative parity band, Band 2, to be in agreement with interpretation for favoured terminating sequences, which signify a change in structure from collective prolate to single-particle oblate shapes. Indeed, the favoured positive-parity states at $89/2^+$, $91/2^+$, and $(101/2^+)$ and the negative-parity $(105/2)$ state, are interpreted as the fully aligned terminating states from comparisons with CNS calculations. The unpaired band crossing at $\hbar\omega$ = 0.55 MeV/$\hbar$ in Band 2, identified previously, is confirmed in the CNS calculations. A band (TSD1) with a high moment of inertia was also observed, which indicates a strongly deformed triaxial collective structure

beyond spin $50\hbar$, which had been previously interpreted from comparison with CNS calculations [Oll09]. However, the exact nature of the gamma-Band between $\hbar\omega \sim 0.2$ and $\hbar\omega \sim 0.35$ MeV/$\hbar$ remains to be understood.

Bibliography

[Afa99] A. V. Afanasjev, *et al.*, *Physics Reports,* volume **322**, (1999) 1.

[Aki06] P. A. Pipidis. *Structural Behavior Of* ^{157,158,159}*Dy In the I = 30 - 50 Spin Regime and the High-Spin Domain of 158Er up to and Above Band Termination.* The Florida State University. PhD thesis,. (2006).

[And76] G. Andersson, *et al.*, *Nuclear Physics A,* volume **268**, (1976) 205.

[Bas80] R. Bass. *Nuclear Reaction With Heavy Ions*, Springer- Verlag, Berlin, (1980).

[Bax92] A. M. Baxter, *et al.*, *Nuclear Instruments and Methods A,* volume **317**, (1992) 101.

[Bea96] C. W. Beausang and J. Simpson. Nuclear Data Tables.*Journal of Physics G:* Nuclear and Particle Physics, volume **22**, (1996) 527.

[Ben79] R. Bengtsson and S. Frauendorf. *Nuclear Physics A,* volume **327**, (1979) 139-171.

[Ben83] T. Bengtsson & I. Ragnarsson. *Physica Scripta,* volume **T5**, (1983) 165.

[Ben85] T. Bengtsson and I. Ragnarsson. *Nuclear Physics A,* volume **436**, (1985) 14.

[Ben90] T. Bengtsson. *Nuclear Physics A,* volume **512**, (1990) 124.

[Boh36] N. Bohr. *Nature,* volume **137**, (1936) 344.

[Boh81] A. Bohr and B. Mottelson. *Physica Scripta,* volume **24**, (1981)71-76.

[Car94] M. P. Carpenter, *et al.*, *Nuclear Instruments and Methods in Physics Research A,* volume **353**, (1994) 234-238.

[Car06] B. G. Carlsson and I. Ragnarsson. *Physical Review C,* volume **74**, (2006) 011302.

[Che11] L. Chen *et al.*, *Physical Review C,* volume **83**, (2011) 034318.

[Cro95] B. Crowell *et al.*, *Background Subtraction for High -Fold Gamma-Ray Coincidence Data. Nuclear Instruments and Methods in Physics Research A,* volume **355**, (1995) 575-581.

[Cwi87] S. Cwiok, *et al.. Computer Physics Communications,* volume **46**, (1987) 379.

[Del87] M. A. Deleplanque. *et al.*, *Physics Letters B,* volume **193**, (1987) 422.

[Dia80] R.M. Diamond, F.S. Stephens. *Annual Reviews, Nuclear and Particle Science,* volume **30**, (1980) 85-115.

[Don87] F. Dönau. Electromagnetic Radiation of Rotating Nuclei.*Nuclear Physics A,* volume **471**, (1987) 469-488.

[Dus06] K. Dusling, *et al*, *Physical Review C,* volume **73**, (2006) 014317.

[Eva04] A. O. Evans. *Lifetime Measurements in 112,110 Te and Band Termination and Beyond in 157 Er.*, Oliver Lodge Laboratory, University of Liverpool, thesis. 2004.

[Fir96] R. B. Firestone. Table of Isotopes. John Wiley and Sons Inc. 1996.

[Fra81] S. Frauendorf. Magnetic Moments in the Backbending Region. *Physics Letters B,* volume **100**, (1981) 219-222.

[Gal95] S. J. Gale, *et al*, *Journal of Physics G,* volume **21**, (1995) 193.

[Gne71] G. Gneuss and W. Greiner. *Nuclear Physics A,* volume **171**, (1971) 449-479.

[Gro73] E. Grosse, *et al., Physical Review Letters,* volume **31**, (1973) 840.

[Har65] S. M. Harris. *Physical Review* volume **138**, (1965) B509.

[Hax49] O. Haxel, J.H.D. Jensen and H.E. Suess. *Physical Review,* volume **75**, (1949) 1766.

[Hod78] P.E. Hodgson. *Nuclear Heavy Ion Reactions*. Oxford Clarendon Press. (1978).

[Ing54] D. R. Inglis. *Particle Derivation of Nuclear Rotation Properties Associated with a Surface Wave. Physical Review,* volume **96**, (1954) 10591065.

[Ing56] D. R. Inglis. *Nuclear Moments of Inertia due to Nucleon Motion in a Rotating Well. Physical Review,* volume **103**, (1956) 17861795.

[Jan77] R. Janssens *et al*, *Nuclear Physics A,* volume **283**, (1977) 493.

[Joh71] A.Johnson, *et al.*, *Physics Letters B,* volume **34**, (1971) 605608.

[Kno10] G. F. Knoll. *Radiation Detection and Measurement*. John Wiley & Sons, Inc.,4th edition, (2010).

[Kon99] F. G. Kondev, *et al.*, *Journal of Physics G,* volume **25**, (1999) 897-899.

[Lag04] K. Lagergren. Private communication. Florida State University, (2004).

[Lee90] I. Y. Lee. *The Gamasphere. Nuclear Physics A,* volume **520**, (1990) 641c.

[May49] M.G. Mayer, *Physical Review*, volume **75**, (1949) 1969.

[Mol95] P. Moller, *et al.*, *Nuclear ground-state masses and deformations, Atomic Data and Nuclear Data Tables* volume **59**,(1995) 185.

[Mot60] B. Mottelson, and J. Valatin. *Physical Review Letters,* volume **5**, *No.* 11, (1960) 511-512.

[Mus11] M. Mustafa, *et al*, *Physical Review C,* volume **84**, (2011) 054320.

[Naz85] W. Nazarewicz *et al.*, *Nuclear Physics A,* volume **435**, (1985) 397.

[New70] J.O. Newton, *et al.*, *Nuclear Physics A,* volume **141**, (1970) 631.

[Nil55] S. G. Nilsson, *Dan Vidensk. Selsk. Mat. Fys. Medd.,* volume **29**, (1955) *No.* 16.

[Nil69] S. G Nilsson *et al*, *Nuclear Physics A,* volume **131**, (1969) 1-66.

[Nol85] P. J. Nolan, *et al.*, *Nuclear Instruments and Methods in Physics Research A,* volume **236**, (1985) 95-99.

[Nol94] P. J. Nolan, *et al.*, *Annual Reviews, Nuclear and Particle Science,* volume **44**, (1994) 561.

[Oll09] J. Ollier and J. Simpson, *et al., Physical Review C*, volume **80**, (2009) 064322.

[Oll11] J. Ollier, *et al.*, *Physical Review C,* volume **83**, (2011) 044309.

[Pau95] E. S. Paul. *Angular correlation analysis with Eurogam II*, (1995).

[Pau07] E. S. Paul, *et al.*, *Physical Review C,* volume **98**, (2007) 012501.

[Pau09] E. S. Paul, *et al.*, *Physical Review C,* volume **79** (2009), 044324.

[Pom83] K. Pomorski and J. Dudek. *Physical Review C,* volume **67** (2003), 044316.

[Rad95] D. C. Radford. *ESCL8R and LEVIT8R: Software for Interactive Graphical Analysis of HPGe Coincidence Data Sets.* http://radware.phy.ornl.gov/rw/esclev/esclev.html.

[Rad95] D. C. Radford. *ESCL8R and LEVIT8R software for interactive graphical analysis of HPGe coincidence data sets. Nuclear Instruments and Methods in Physics Research A,* volume **361**, (1995) 297.

[Rad00] D. C. Radford, ESCL8R and LEVITER: *Software for interactive Graphical Analysis of HPGe Coincidence Data Sets.* http://radware.phy.ornl.gov.

[Rag86] I. Ragnarsson, *et al.*, *Physica Scripta,* volume **34**, (1986) 651.

[Ray73] A. Raymond, Sorensen. *Reviews of Modern Physics,* volume **45**, *No.* 3, (1973) 353- 377.

[Ree11] J. M. Rees, E. S. Paul. *et al*, *Physical Review C,* volume **83**, (2011) 044314.

[Rie80] L. L. Riedinger, *et al.*, *Physical Review Letters,* volume **44** *No.*(9), (1980) 568-571.

[Ril88] M. A. Riley, J. D. Garrett, J. Simpson, and J. F. Sharpey-Schafer. *Physical Review Letters,* volume **60**, 092501 (1988).

[Ril09] M. A. Riley, *et al.*, *Acta Physica Polonica B,* volume **40**, (2009) 513.

[Rin80] P. Ring and P. Schuck. *The Nuclear Many-Body Problem.* Springer-Verlag Inc, (1980).

[Shi12] Y. Shi, J. Dobaczewski, S. Frauendorf, W. Nazarewicz, J. Pei, F. Xu, and N. Nikolov. *Physical Review Letters,* volume **108**, (2012) 092501.

[Sim84] J. Simpson, *et al*, *Journal of Physics G,* volume **10**, (1984) 383.

[Sim87] J. Simpson, *et al.*, *Journal of Physics G:Nuclear Physics,* volume **13**, (1987) 847-881.

[Sim94] J. Simpson, *et al.*, *Physics Letters B,* volume **327** (1994) 187-194.

[Sim98] J. Simpson, *et al.*, *European Physical Journal A,* volume **A 1** (1998) 267-274.

[Ste72] F. S. Stephens and R. S. Simon. *Nuclear Physics A,* volume **183**, (1972) 257-284.

[Ste73] R.M. Steffen, *et al.*, *Nuclear Data Tables.* Springer-Verlag Berlin, volume A **11**, (1973) 351.

[Ste75] F. S. Stephens. *Reviews of Modern Physics,* volume **47**, *No.* 1, (1975) 43- 65.

[Ste85] F. S. Stephens. *Physical Review Letters,* volume **54**, (1985) 2584.

[Str67] V. M. Strutinsky. *Nuclear Physics,* volume A **95**, (1967) 420.

[Str68] V. M. Strutinsky. *Nuclear Physics,* volume A **122**, (1968) 1.

[Str75] H. Strusny, *et al.*, *Nuclear Physics A,* volume **242** (1975) 30-44.

[Syz83] Z. Szymanski. *Fast Nuclear Rotation*, Claredon Press, Oxford, (1983).

[Tea09] C. Teal. *Structural Changes in* ^{161}*Tm and* ^{121}*Sn As A Function of Increasing Angulat Momentum.* The Florida State University. PhD thesis,. (2009).

[Tjø85] P. O. Tjøm, *et al.*,*Physical Review Letters,* volume **55**, (1985) 2405.

[Tor97] S. Törmanen, *et al.*, *Nuclear Physics A,* volume **613**, (1997) 282.

[Wan11] X. Wang, *et al.*, it{Physics Letters B. volume **702**, (2011) 127.

[Wei35] C.F. von Weizsacker. *Zeit. Phys,* volume **96**, (1935) 431.

[Won98] S. S. M. Womg. *Introductiry Nuclear Physics* Wiley-VCH,(1998).

[Woo54] R. D. Woods and D. S. Saxon. *Physical Review,* volume **95**, (1954) 577-578.

Here is where the original thesis contained the following article:

Diverse collective excitations in ^{159}Er up to high spin

M.Mustafa et al

Physical Review C 84 054320 (2011)

http://dx.doi.org/10.1103/PhysRevC.84.054320